High-Spatial-Resolution Laser Diagnostics for a Dual-Mode Scramjet

---

A

Dissertation

Presented to

the faculty of the School of Engineering and Applied Science

University of Virginia

---

in partial fulfillment

of the requirements for the degree

Doctor of Philosophy

by

Clayton Geipel

December 2020

APPROVAL SHEET

This

Dissertation

is submitted in partial fulfillment of the requirements
for the degree of

Doctor of Philosophy

Author: Clayton Geipel

This Dissertation has been read and approved by the examing committee:

Advisor: Harsha Chelliah

Advisor: Chloe Dedic

Committee Member: Christopher Goyne

Committee Member: Andrew Cutler

Committee Member: Charles Sackett

Committee Member:

Committee Member:

Committee Member:

Accepted for the School of Engineering and Applied Science:

Craig H. Benson, School of Engineering and Applied Science

December 2020

For Sarah

Acknowledgments

Where to begin? I owe so much to so many. Thank you to all who have helped me on this journey. To name only a few:

- Prof. Harsha Chelliah and Prof. Chloe Dedic, thank you for being excellent advisors. Your constant support has been invaluable, and I have learned so much from you both.

- Prof. Andrew Cutler, thank you for your guidance throughout the scramjet project.

- Prof. Christopher Goyne and Prof. Cass Sackett, thank you for serving on my advisory committee and providing feedback on the development of this dissertation.

- Dr. Paul Danehy and Dr. Ross Burns, thank you for your help in the characterization of the high-magnification camera system.

- Dr. Damien Lieber, Dr. Bob Rockwell, Vanessa Awate, Walker Smith, Christopher Spelker, Zeid Hashem, and Noah Bakr, thank you for your collaboration on scramjet experiments.

- Dr. Andreas Rauch, Dr. Tanner Nielsen, Dr. Ryan Johnson, Dr. Gabe Goodwin, thank you for providing your simulation results and helping me to understand them.

- Dr. Campbell Carter and Prof. Tonghun Lee, thank you for sharing with me your draft book chapter on LIF theory and practice; it was an invaluable resource in completing this work.

- Sean Alberts, Ryan Thompson, Dr. Khanh Dang, Naja Tyree, and Dominic Pinnisi, thank you for your collaboration in the Reacting Flow Laboratory.

- Prof. Kathryn Thornton and Prof. Gavin Garner, thank you for teaching me how to teach.

- Prof. Jim McDaniel, thank you for talking me into pursuing a doctoral degree.

- Dr. Yousef Shakhsheer, thank you for not talking me out of pursuing a doctoral degree and for keeping tabs on my progress.

- Karen Nowicki, Marivic Mitchell, Laura Akesson, Denise Williams, Henry Hurlburt, Michael Fetsko, and Todd Phillips, thank you for encouraging me down the path to becoming an engineer.

- Mike and Lennie Geipel, Doug and Tidge Roller, and Sarah Kelley, thank you for being there with me every step of the way.

Contents

List of Tables

List of Figures

List of symbols and abbreviations

Symbols

quantity	unit	description
A_c	[cm^2]	light sheet cross-sectional area
A_{ij}	[s^{-1}]	spontaneous emission rate coefficient
B_{ij}	[m^2/(J·s)]	Einstein B-coefficient
c	[-]	diffusion coefficient, anisotropic diffusion filter
c	[m/s]	speed of light
$\bar{c}$	[-]	mean progress variable
E	[V/m]	electric field strength
f_B	[-]	Boltzmann fraction
F	[-]	modulation transfer function
F_{ij}	[cm^{-1}]	rotational term energies
G_v	[cm^{-1}]	vibrational term energies
g	[-]	energy state degeneracy
$\hat{g}$	[cm^{-1}]	laser overlap intergral
H	[mm]	cavity height
h	[m^2·kg/s]	Planck constant
I	[-]	pixel intensity
I	[W/cm^2]	irradiance

I_0	[-]	flame stretch factor
i, j	[-]	pixel indices
$\mathcal{I}$	[-]	intermittency
J	[-]	rotational quantum number
Ka_η	[-]	Karlovitz number based on Kolmogorov length scale
k	[J/K]	Boltzmann constant
$\mathcal{K}$	[-]	constant, anisotropic diffusion filter
L	[mm]	cavity length
l_i	[μm]	line group length
l_r	[μm]	resolution length scale
P	[-]	probability
P	[W]	power
p	[atm]	pressure
m	[-]	image modulation
m_u	[kg]	atomic mass unit constant
M	[-]	magnification
M	[-]	molecular weight
N	[-]	number of iterations, anisotropic diffusion filter
N	[cm^{-3}]	number density
n_i	[-]	collisional broadening empirical power law coefficients
Q_e	[s^{-1}]	electronic quenching rate
Q^P	[-]	partition function
Re_Λ	[-]	Reynolds number based on integral length scale
r	[mm]	radial coordinate
R	[μm]	beam wavefront radius of curvature
s	[mm]	flame front pathwise coordinate
s_L	[m/s]	laminar burning velocity

s_T	[m/s]	turbulent burning velocity
T	[K]	temperature
U	[J]	pulse energy
u	[m/s]	x-direction duct velocity
v	[-]	vibrational quantum number
W	[mm]	cavity width
W	[kg/mol]	molecular weight
W_{ij}	[s^{-1}]	stimulated rate coefficients
w	[μm]	beam radius
x, y, z	[mm]	spatial coordinates
X	[-]	mole fraction
Y	[-]	mass fraction
α	[°]	beam crossing half-angle
$\gamma_{i,0}$	[cm^{-1}/atm]	collisional broadening coefficients
δ_L	[mm]	flame length scale
Δt	[-]	timestep, anisotropic diffusion filter
$\Delta \nu_C$	[cm^{-1}]	collisional broadening linewidth
$\Delta \nu_D$	[cm^{-1}]	Doppler broadening linewidth
$\Delta \nu_L$	[cm^{-1}]	laser linewidth
η	[μm]	Kolmogorov length scale
η	[F/m]	permittivity
κ	[mm^{-1}]	curvature
Λ	[mm]	integral length scale
ν	[m^2/s]	dynamic viscosity
σ	[-]	standard deviation
Σ	[mm^{-1}]	flame surface density ψ

| [-] | Gouy phase shift |

Abbreviations

abbreviation	description
CARS	coherent anti-Stokes Raman scattering
CCD	charge-coupled device
CFD	computational fluid dynamics
DG	discontinuous-Galerkin simulation
DNS	direct numerical simulation
FLEET	femtosecond laser electronic excitation and tagging
FSD	flame surface density
FWHM	full-width at half-maximum
ICCD	intensified charge-coupled device
IFSD	integrated flame surface density
LES/RANS	large eddy simulation/Reynolds-averaged Navier-Stokes simulation
PLIF	planar laser-induced fluorescence
PIV	particle image velocimetry

Abstract

Dual-mode scramjets present new possibilities for the aerospace industry: high-speed commercial flights, high-speed defense applications, and more cost-effective access to space. Cavity flameholders are typically employed in scramjet combustors to create a recirculation region that increases the local residence time and production of key radical species, such as hydroxyl (OH). These radicals mix with the main flow through a highly-dynamic shear layer separating the main flow and the cavity flow. Most current experimental and computational techniques for cavity-stabilized flames do not resolve all spatial scales. Direct Numerical Simulation (DNS) models provide full resolution from Kolmogorov scales to integral scales, but are extremely computationally expensive and require validation through experimental measurements. The University of Virginia Supersonic Combustion Facility (UVaSCF) is an optically-accessible ground test facility capable of simulating the conditions of a scramjet in Mach 5 flight and generating experimental data critical for establishing simulation boundary conditions. Previous studies have characterized a wall-mounted cavity flame holder of height 9 mm. A scaled-down strut-mounted cavity of height 3 mm was recently designed to provide a domain with a volume small enough to simulate completely using DNS.

This dissertation presents OH planar laser-induced fluorescence (PLIF) measurements obtained for both cavity configurations, with maximum resolution $40 \times 40 \times 25$ μm, significantly exceeding the resolution of previous measurements of comparable flows. OH-PLIF images are processed to obtain the intermittency of the flame and the distribution of local values for flame surface density and flame front curvature. These metrics describe the location

and shape of the flame brush and the distribution of flame front length scales. Simulated OH-PLIF images are produced from DNS results for direct comparison with experiments through flame structure metrics. Simulated OH-PLIF images show flame structure sizes comparable to those found experimental images and the flame is shown to spread into the main duct flow at approximately the same angle as in experiments. This agreement with experiments validates turbulence-chemistry interactions resolved by DNS.

In addition, this dissertation describes the construction of a new hybrid fs/ps rotational/vibrational coherent anti-Stokes Raman scattering (CARS) system. Broadband pulse generation will enable this system to simultaneously measure temperature and major combustion species, e.g. O_2, N_2, CO_2, and C_2H_4. The spatial resolution of this system is quantified using a microscale jet of nonresonant gas. The effects of crossing angle and beam astigmatism on the spatial resolution are investigated in order to minimize the size of the CARS interrogation volume. This will minimize the effects of spatial averaging over the small length scales present in turbulent flames. A minimum interrogation volume length of 200 μm was achieved. This system will be used to gather temperature and species information in future scramjet flow configurations.

Chapter 1

Introduction

This dissertation has two primary objectives. First, it is intended to demonstrate methods for improving the spatial resolution of laser-based measurement systems for measuring temperature and species in combustion environments with small spatial scales. Second, it seeks to improve understanding of premixed, turbulent combustion in a dual-mode scramjet ground test facility through the application of these diagnostic methods.

1.1 Literature review

1.1.1 Scramjet propulsion

Ramjets and scramjets have the potential to change all sectors of the aerospace industry. A ramjet is a jet engine that uses a convergent duct for compression instead of turbomachinery. If the flow through the ramjet is supersonic, it is known as a **s**upersonic-**c**ombustion **ramjet** - a scramjet. If the flow is partially-supersonic and partially-subsonic, it is known as a dual-mode scramjet. In dual-mode flow conditions, a scramjet can provide flight Mach numbers between 3 and 5 while avoiding some flame stability issues affecting fully-supersonic combustion. Chapters 2 - 4 refer to experimental and computational studies on a ground-test

facility replicating conditions inside a dual-mode scramjet engine; all discussion of scramjets will refer to the dual-mode configuration.

High-speed commercial and defense aircraft could be built with scramjets, enabling manned flight at speeds much faster than currently available. Scramjet propulsion could be used for long-range unmanned flight (providing a faster alternative to cruise missiles). In addition, a scramjet could serve as one stage in a space launch vehicle. Without the need for an onboard oxidizer, a scramjet is much more fuel-efficient than a rocket engine. More cost-effective access to space could be achieved by using scramjets and rockets together (as scramjets alone cannot achieve escape velocity).
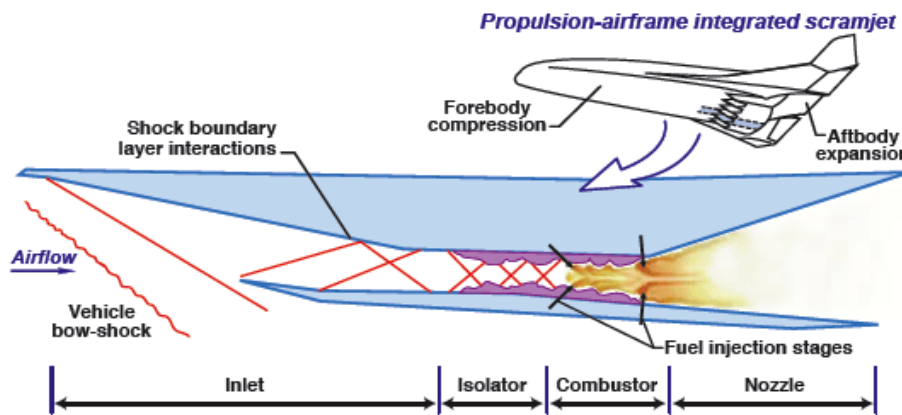
Figure 1.1: Scramjet schematic fron NASA LaRC [1].

Figure 1.1 illustrates the general architecture of a scramjet engine. Air enters a converging inlet at supersonic speeds. A train of oblique shocks causes the pressure and temperature of the air to rise as it travels downstream. A constant-area isolator section is used to distance the combustor from the inlet, reducing the effects of combustion back-pressure on flow through the inlet. Fuel can be added in the isolator section; movement through the shock train causes effective mixing between fuel and air, resulting in a well-premixed flow in the combustor section. In a non-premixed case, fuel injection occurs in the combustor section.

1.1.2   Cavity-stabilized flames

High duct velocities in relation to chemical reaction rates require scramjet flames to be stabilized by a region of recirculation that provides a continuous ignition source. While many flow recirculation geometries have been explored, recent works have focused on cavity flameholders because of low pressure losses in the combustor [2, 3, 4].

Fuel-air mixing, ignition, and stable combustion in scramjet engines have been the focus of numerous investigations (see [5, 6] for detailed reviews). The exact flame structure in these flows depends on the fuel injection location, overall residence time, turbulent mixing time scales, and chemical time scales, with non-premixed and premixed reacting flow configurations as limiting flame structure modes. In non-premixed flames with large Damköhler numbers, as are found in high-enthalpy flows with fuel injected in the cavity or just upstream of the cavity [7], the flame structure is largely dictated by the turbulent mixing rate between fuel and air and not by finite-rate kinetics. At this large Damköhler number limit, ignition typically starts at the fuel rich boundary of the dynamic mixing layer and subsequently adjusts to the stoichiometric mixture fraction location within the mixing layer (corresponding to a local equivalence ratio of unity). For lower Damköhler numbers (for example, in flows with lower enthalpy associated with lower flight Mach numbers) and when fuel is injected further upstream of the cavity, the flame structure transitions to a partially-premixed flame anchored above the recirculation region in the cavity. These effects were clearly demonstrated by Micka and Driscoll [8] who performed a series of experiments in which fuel was injected into a supersonic combustor duct from wall-normal injectors placed at several locations upstream of a cavity. At higher temperatures with large Damköhler numbers, the flame would anchor behind the recirculation regions formed by individual fuel jets. At lower static temperatures, the flame was anchored in the stratified mixing layer over the cavity with the degree of stratification dictated by the fuel injection location and turbulent mixing time scales.

Pure diffusion flames and fully-premixed flames represent ideal limits between which practical flows exist, and both limits provide conceptual and practical simplifications that

help in understanding the scramjet combustion processes. Premixing without pre-ignition can be accomplished by moving fuel injectors further upstream of the cavity at moderate Mach numbers [9, 10]. In the premixed limit, chemical kinetic effects and turbulence-flame interactions are isolated from fuel-air mixing. The flame downstream of the cavity can be treated approximately as a one-dimensional flame propagating in a static field of reactants, connecting scramjets to the large body of research into turbulent premixed flames [11, 12]. Turbulent mixing between the fully-premixed reactant stream and the product species emanating from the cavity across the dynamic shear layer dominates the combustion process at these high speeds. In other words, the rate-controlling mixing process between fuel and air in non-premixed flames has been replaced by a mixing process between reactants and product species in this premixed mode. Thus, recirculation regions produced by cavity flame holders are critical for flame stabilization in these high-speed premixed flames as well.

This work is part of a coordinated experimental and computational investigation of premixed cavity-stabilized combustion in which fuel is injected far upstream of the combustor to achieve a near-uniform mixture in the vicinity of the cavity flameholder. The flame produced in this mode can be used to investigate the physics of high-speed combustion and test assumptions made by chemical-kinetic models. Fundamental premixed flame structure information gathered at highly turbulent and compressible flow conditions is scarce, and relevant both for understanding scramjet flows and for the general validation of models that describe turbulence-chemistry interactions occurring at unresolved scales [13].

Relevant normalized length and time scales can be defined for premixed combustion: the turbulent velocity fluctuation normalized with respect to laminar burning velocity, u'/s_L, and the integral turbulent length scale normalized with respect to the laminar flame thickness, Λ/δ_L. These parameters are used to define the Reynolds number based on integral length scale Re_Λ and the Karlovitz number based on Kolmogorov length scale Ka_η as shown in Eqs. (1.1) and (1.2). These dimensionless numbers control the structure of premixed flames and can be used to categorize a given flame into distinct commbustion regimes, known as laminar
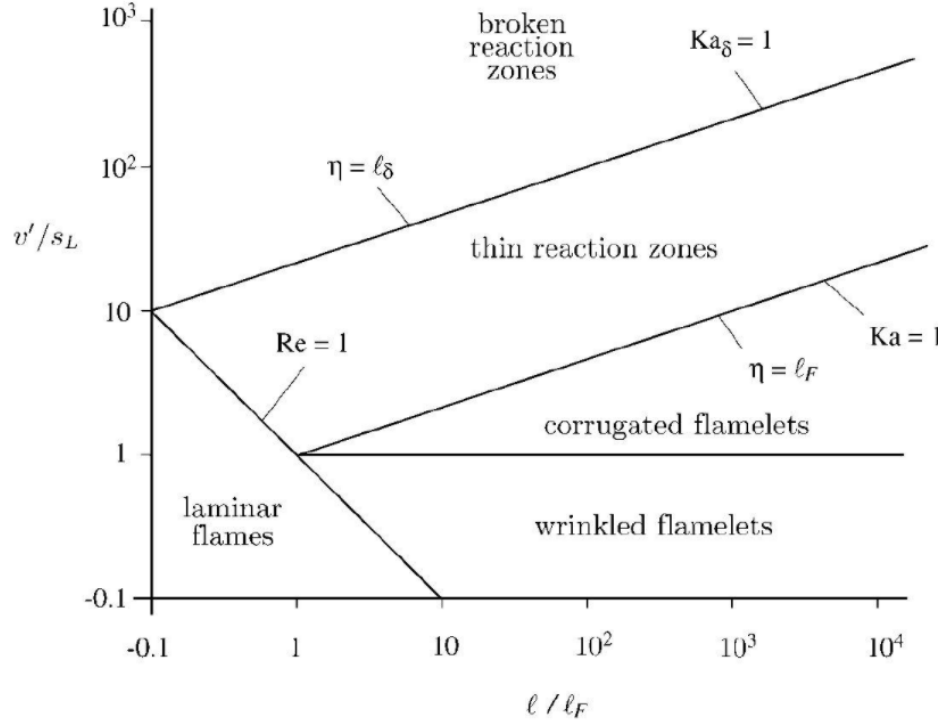
Figure 1.2: Premixed turbulent combustion regimes, from Peters [14].

flames, wrinkled flamelets, corrugated flamelets, thin reaction zones, and broken reaction
zones [14], as shown in Fig. 1.2. Experimental analysis of the flame structure therefore
provides insight into how inflow turbulence interacts with the chemical kinetics of the flame.
Turbulent flame speed correlations [14, 15] can be used to relate the Reynolds number of the
flow to the flame speed and predict the flame angle, defined as the angle at which the flame
spreads away from the flame holder.

$$\mathrm{Re}_\Lambda = \frac{u'}{s_L} \frac{\Lambda}{\delta_L} \tag{1.1}$$

$$\mathrm{Ka}_\eta = \left(\frac{u'}{s_L}\right)^{3/2} \left(\frac{\Lambda}{\delta_L}\right)^2 \tag{1.2}$$

In the premixed mode, turbulent mixing between the premixed fuel-air stream and product
species across the flame structure dominates the combustion process. This is particularly
relevant for hydrocarbon-fueled systems where slower reaction times produce longer ignition

delay times and longer overall reaction times for complete combustion [16]. Thus, recirculation regions produced by cavity flameholders are critical for flame stabilization in these high-speed flow fields. These recirculation regions generate product species including highly-reactive radical species such as hydroxyl (OH). The mixing of radical species from the cavity with the inflow occurs through a highly-dynamic shear layer. The inflow in this work, as in many other ground test investigations, is a gaseous ethylene-air mixture. Ethylene (C_2H_4) is the major product of the thermal decomposition of liquid hydrocarbon fuels. Previous premixed C_2H_4-air experiments [17, 18, 19] produced stable partially-premixed flames anchored above the cavity, with varying fuel-air equivalence ratio across the inflow plane, i.e. in a stratified fuel-air mixture.
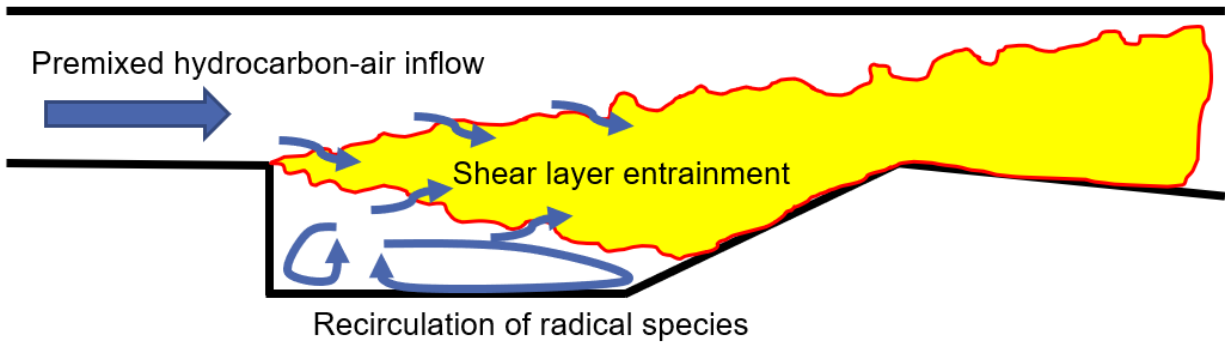
Figure 1.3: Cavity flameholder schematic.

1.1.3 Planar laser-induced fluorescence

Laser-induced fluorecence (LIF) [20, 21] is an optical diagnostic technique in which laser light electronically excites a target species, resulting in radiative decay (i.e. fluorescence). This fluorescence is captured by a sensitive camera or photomultiplier tube. LIF is widely-used for visualizing fluid flows, as laser light can be shaped to provide planar (PLIF) and volumetric (VLIF) measurements of individual species concentration [22].

PLIF is often used as a non-intrusive diagnostic technique for measuring species concentrations in combustion experiments [23, 24]. PLIF images are two-dimensional maps

describing the presence or absence of the target species. PLIF signal is typically a qualitative measurement; areas of higher PLIF signal indicate greater local concentration of the target species. Quantitative target species concentration values can only be obtained after careful correction for factors such as fluorescence quenching and reabsorption, laser sheet irradiance variation (both between laser pulses and between different positions within the laser sheet), and temperature and pressure dependencies [25].

Common target species for PLIF combustion experiments include CH_2O (identifying the preheat zone of the flame) [26, 27], CH (identifying the location of peak heat release) [28], and tracers such as NO [29] and toluene [30]. OH is the most common choice of target species among combustion products [31, 32, 33, 34]. OH is a long-lived combustion radical produced near the zone of peak heat release; it is often used as a flag for the presence or absence of combustion products in general. Several different transitions produce OH PLIF signal at very high signal-to-noise ratios; one is the $Q_1(8)$ transition of the $A^2\Sigma^+ \rightarrow X^2\Pi(1,0)$ band, excited at 283.55 nm [35, 36]. PLIF signal acquired using this band is relatively-insensitive to temperature; the Boltzmann fraction of the lower state varies by less than 10% as temperature varies from 1200 to 2300 K [37].

OH-PLIF has been used extensively for imaging flames anchored on cavity flameholders [38, 39, 40, 41]. However, previous studies typically are not finely-resolved enough to distinguish flame wrinkles at all length scales and do not quantify the in-plane resolution of the images. Images presented by these studies often do not resolve structures smaller than about 300 µm. However, as will be shown in Chapter 2, structures smaller than 100 µm can be expected to exist in these high-speed flames. OH-PLIF resolution improvements must be made in order to resolve the finest structures. High-spatial-resolution experimental capabilities are necessary in order to produce data comparable with the output of new and upcoming direct numerical simulations (DNS) [42, 43] which resolve flame structure to Kolmogorov length and time scales.

1.1.4 Coherent anti-Stokes Raman scattering

Coherent anti-Stokes Raman spectroscopy (CARS) is a nonlinear optical technique in which three laser pulses referred to as pump, Stokes, and probe are overlapped and focused, producing a coherent signal which contains temperature and species information for the sampled molecules present in the measurement volume [44, 45]. CARS is often used in harsh combustion environments, providing noninvasive thermometry and species concentration data that cannot be collected by other methods [46, 47, 48]. The pump beam excites target molecules from the current state to a higher virtual state. Simultaneously, the Stokes beam causes a transition from the virtual state to a lower state. The frequency difference between the pump and Stokes beams is selected to match a Raman-active transition of the target molecule. The probe beam excites the molecules to a new virtual state, and CARS signal is emitted at the anti-Stokes frequency as they return to the original state. The resultant CARS signal depends on the population difference between energy levels participating in the transition. Population distribution is dependent on temperature, as shown by the Boltzmann equation [49], printed in Eq. (1.3), where N is the total number density, N_j is the number density of a given energy state ϵ_j, g_j is the degeneracy of the state, k_B is Boltzmann's constant, and T is temperature.

$$N_j = N \frac{g_j e^{-\epsilon_j/(k_B T)}}{\sum_j g_j e^{-\epsilon_j/(k_B T)}} \tag{1.3}$$

CARS can be used to target vibrational ($\Delta v = \pm 1$, $\Delta J = 0$) or rotational ($\Delta v = 0$, $\Delta J = \pm 2$) transitions. With broadband pulses, many species can be excited and measured simultaneously [50]. In vibrational CARS, the frequency difference between the pump and Stokes beams is chosen to equal the Raman-active vibrational frequency of the molecules, causing transitions between vibrational states. (This process will be termed "vibrational CARS" in this dissertation; it is sometimes called "ro-vibrational" CARS in other works.) Pure rotational transitions can be excited by pump and Stokes pulses with the same central

wavelength, as the bandwidth of the fs pulses (150 cm^{-1}) is on the same order as the frequency difference of the rotational transitions (~ 10 cm^{-1} and higher). A dual-pump fs/ps CARS system performs both processes simultaneously, with a single Stokes beam, a single probe beam, and two pump beams, one to excite vibrational transitions and one to excite rotational transitions [51]. Figure 1.4 is an energy diagram of the excitation scheme of dual-pump CARS.
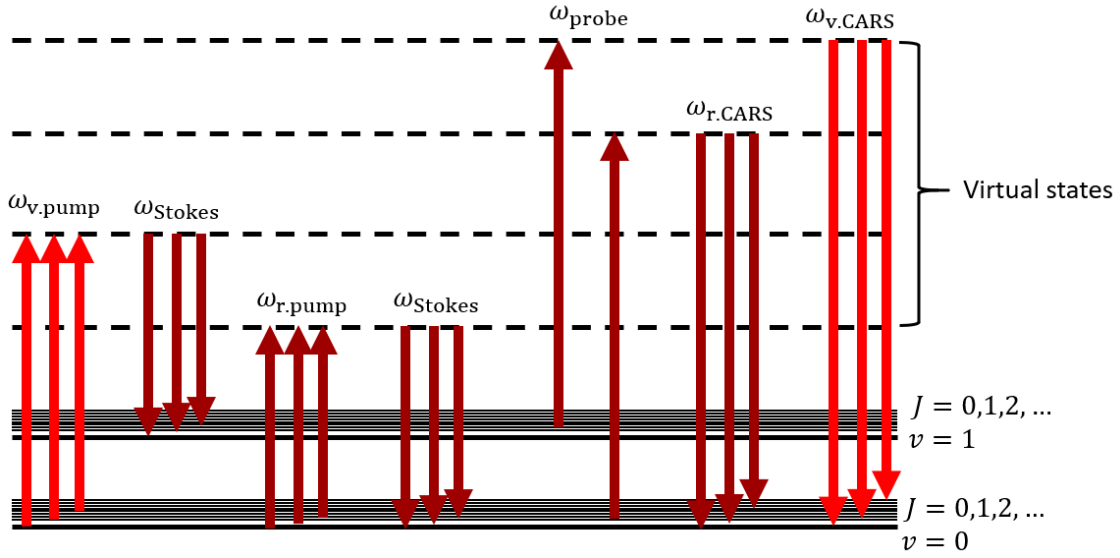
Figure 1.4: Energy diagram for dual-pump CARS. The broadband nature of fs pulses are represented by groups of three arrows.

Hybrid femtosecond/picosecond (fs/ps) CARS is an approach that uses pump and Stokes pulses shorter than 100 fs and a probe pulse several picoseconds in duration [52]. This method has several benefits over traditional ns excitation schemes. With fs excitation, the probe pulse can be delayed in time to suppress nonresonant signal [53, 54, 55], and the resultant CARS signal is insensitive to collisions [30] when short probe delays are employed—making it an ideal candidate for measurements at elevated pressures. In addition, high beam quality from a regeneratively-amplified Ti:sapphire femtosecond laser reduces the focused beam waist of the CARS beams relative to previous ns CARS measurements resulting in improved spatial resolution. Femtosecond laser pulses are inherently broadband; this property can be used to generate CARS signal in multiple target species simultaneously without using
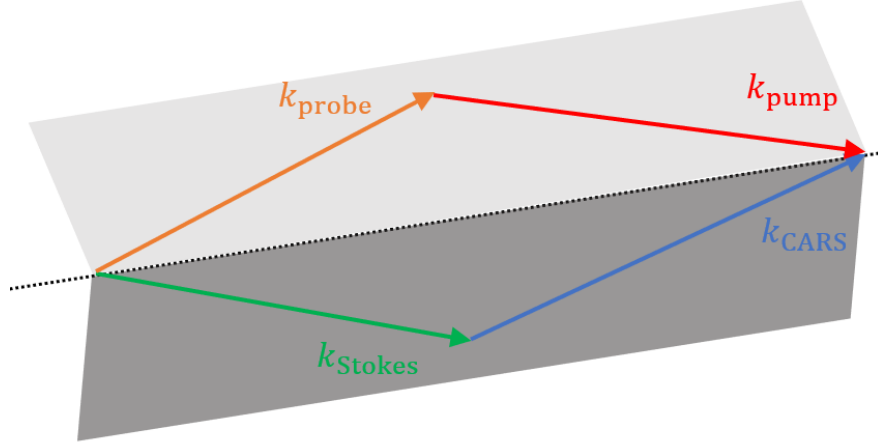
Figure 1.5: Folded BOXCARS phase-matching configuration.

a broadband dye laser. Finally, femtosecond pulses have significantly smaller total pulse energies than nanosecond pulses but are able to generate more CARS signal. As a result, CARS with femtosecond pulses can be used to acquire spatially-resolved measurements along a line [56, 57, 58, 59].

The CARS process must conserve both energy, as shown in Eq. (1.4), and momentum, as shown in Eq. (1.5). The latter requirement is referred to as phase matching.

$$\omega_{\text{pump}} + \omega_{\text{probe}} - \omega_{\text{Stokes}} - \omega_{\text{CARS}} = 0 \tag{1.4}$$

$$\mathbf{k}_{\text{pump}} + \mathbf{k}_{\text{probe}} - \mathbf{k}_{\text{Stokes}} - \mathbf{k}_{\text{CARS}} = 0 \tag{1.5}$$

A common phase-matching configuration, known as folded BOXCARS [60, 61] is depicted in Fig. 1.5. In this configuration, $\mathbf{k}_{\text{CARS}}$ propagates in a direction separate from the other three waves, making it unnecessary to filter the CARS signal from the other beams. A single focusing lens is often used to converge the input beams to a single point, a second lens recollimates the CARS signal, as shown in Fig. 1.6.

In the region where the pump, probe, and Stokes beams intersect, CARS signal is produced with local irradiance proportional to the product of the local irradiances of the three input
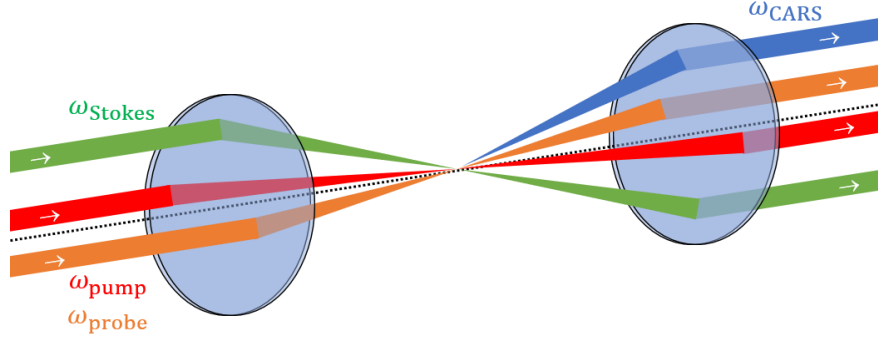
Figure 1.6: CARS generation using a single focusing lens, adapted from [62].

beams: $I_{CARS} \propto I_{pump} I_{probe} I_{Stokes}$ [25]. This region of interaction between the beams will be called the interrogation volume. For BOXCARS phase matching, this volume is an elongated ellipsoid, with a semi-major axis (the "length" of the volume) largely controlled by the beam crossing angle, and two semi-minor axes (the "width" of the volume) largely controlled by the diameter of each incoming beam at the crossing location. The extent of the interrogation volume is an important parameter for the design of a CARS experimental investigation. By minimizing the interrogation volume size, the spatial resolution of the experiment is increased. However, this also decreases the intensity of the collected CARS signal. Folded-BOXCARS experiments with small crossing angles commonly have interrogation volumes on the order of 1 mm in length [51, 63]; this can produce undesirable spatial averaging effects in environments such as scramjet flames in which temperature gradients occur on scales of order 100 µm or less [64].

Several methods have been used to evaluate the size of CARS interrogation volumes. The most common method involves the translation of a thin glass coverslip along the length of the volume. The intensity of the nonresonant CARS signal generated in the glass is recorded at each coverslip position [65, 63, 66, 58, 67]. This method is prone to inaccuracy because, in order to avoid damaging the coverslip, beam energies must be drastically attenuated, which may change the extent of CARS signal generation. This method also cannot be used to measure the width of the interrogation volume; the width is sometimes measured by translating a knife edge across the volume [68] or measuring burn patterns at beam foci

[69, 70].

Several studies [57, 71, 72] have measured focus beam diameters d and crossing angles α to estimate the interrogation volume width as $w = d/\sin\alpha$. This method assumes that the centers of the input beams intersect perfectly and that the crossing occurs at the beams' foci.

Tedder et al. [73] used a beam splitter to direct a weak reflection of the input beams through neutral density filters and onto a CCD camera. The camera was translated to acquire beam profiles at several planes, enabling the construction of a three-dimensional model of the interrogation volume. In this approach, care must be taken to ensure that the beam position in the profile images is not altered by the splitter or filters, that the camera responds linearly to increases in beam energy, and that the camera has equal sensitivity to beams of different frequency content.

Finally, CARS probe volume length can be determined by translating the CARS beams relative to a small gas-phase structure, and acquiring CARS spectra at different positions. One series of studies [74, 75, 76] used the tip of a conical flame of diameter 3 mm for this purpose, measuring the change in temperature as the beams were translated. Snow et al. [70] performed one-dimensional rotational CARS with nanosecond pulses and measured the interrogation volume size using a 1 mm-diameter jet of Freon-12 in an O_2 co-flow, measuring the extent of the absence of O_2 CARS signal. Dedic [51] used a jet created by a tube of inner diameter 100 µm to evaluate the spatial resolution of an ultrafast CARS system, however, the exact width of the jet downstream of the needle exit was not quantified.

1.2   Research goals

In order to improve PLIF and CARS diagnostic techniques, and in order to improve understanding of the behavior of turbulent flames, this dissertation aims to achieve the following goals.

1. Design an in situ diagnostic system to capture OH-PLIF with spatial resolution sufficient to capture all length scales.

2. Using high-spatial-resolution OH-PLIF, characterize the flame structure of multiple cavity-stabilized premixed flames, and infer the effect of cavity scaling on flame structure.

3. Use experimental data to evaluate the accuracy of simulations of cavity-stabilized flames.

4. Design a high-spatial-resolution hybrid fs/ps CARS system and investigate the effects of beam crossing angle and focusing conditions on interrogation volume size.

1.3   Dissertation overview

The following is an outline of the remaining chapters of this dissertation.

Chapter 2 describes the high-spatial-resolution OH-PLIF experiment. The construction of the OH-PLIF system is described, and a characterization of the system resolution is provided. OH-PLIF intensity statistics are provided for flames stabilized on cavity flameholders of heights 9 mm and 3 mm. A comparison of the gross behavior of both flames on the basis of intensity statistics follows.

Chapter 3 concerns the extraction of morphological information from OH-PLIF images. An image binarizaiton process is described, followed by calculations of metrics including flame intermittency, flame angle, and flame front curvature. The results are compared to those published for other premixed flames, providing information on the turbulent combustion regime of the cavity-stabilized flames.

Chapter 4 presents a comparison between the OH-PLIF experimental results and computational simulations of the 3 mm cavity flowpath from other published sources. Hybrid LES/RANS and discontinuous Galerkin simulations are discussed in brief. DNS results are explored in more depth. A model of the LIF process employed in the experiment is used to

investigate temperature and pressure effects on OH-PLIF images. OH mass fraction values are used to generate simulated PLIF images based on a finite laser sheet width; the effects of the width of the laser sheet are also explored. These synthetic images are processed to generate statistics and morphological metrics that are be directly compared to experimental results. The fidelity of each simulation to the experiment is discussed with recommendations for improvement.

Chapter 5 describes the construction of a high-spatial-resolution dual-pump hybrid fs/ps CARS system. The size of vibrational and rotational CARS interrogation volumes were measured for multiple different focusing lens and beam crossing configurations; this was performed by translating a micro-scale jet of nonresonant gas through the interrogation volume and observing the drop in resonant CARS signal. This quantifies the spatial resolution of the CARS system; this provides important context for ultrafast CARS measurements of combustion environments with small spatial scales.

A conclusions section provides a summary of the work presented here, as well as recommendations for further study. Appendices provide information about an upcoming application for the CARS system as well as supplemental tables and figures.

Chapter 2

High-spatial-resolution PLIF measurements for cavity-stabilized flames

2.1 Motivation and objectives

OH-PLIF measurements in scramjet flows typically resolve flame structures at integral length scales and at some intermediate length scales, but cannot resolve flame structures near Kolmogorov length scales. Results from direct numerical simulations (DNS) of scramjet flows resolve all turbulent length scales; in order to fully validate the results of these simulations, experimental resolution of PLIF images must be increased. This presents two principal challenges. First, the magnification of the camera must be maximized while maintaining image quality. Then, the thickness of the laser sheet must be minimized without excessive loss of laser energy. Both the camera resolution and the laser sheet thickness must be carefully measured to facilitate comparison with computational results and the results of other experiments.

Previously-studied cavity flame holders typically have experimental domains that are

too large and too computationally-expensive to simulate using DNS. A new reduced-size cavity flame holder has recently been designed [77] to provide a feasible domain for DNS computations [42, 43]. An OH-PLIF investigation of this flame holder is necessary to characterize the structure of the new flame, understand the interaction between the premixed combustion process and turbulence effects, and validate the chemical-kinetic model employed by the DNS investigation.

The first part of this chapter presents the design for an OH-PLIF system with spatial resolution sufficient to capture all flame structure length scales for the scramjet flow. The system has a maximum spatial resolution of 40 × 40 × 25 μm. The second part of this chapter presents the results of scramjet experiments. Turbulent, compressible flames anchored on cavities of two different sizes were measured. These high-resolution measurements are used in Chapter 3 to extract metrics characterizing the structure of the scramjet flames and placing them into context with other premixed flames. In Chapter 4, these measurements provide a basis for comparison with computational investigations.

2.2   U.Va. Supersonic Combustion Facility

2.2.1   Tunnel

The University of Virginia Supersonic Combustion Facility [78, 10] (UVaSCF) is an optically-accessible scramjet ground testing facility in which compressed air is electrically heated to produce a non-vitiated continuous flow. In the current configuration, the high-enthalpy flow passes through a nozzle that generates a Mach 2 free stream. The enthalpy of the flow corresponds to a vehicle travelling at a flight Mach number of about 5. C_2H_4 is injected perpendicular to the flow in an isolator section, far upstream of the cavity flameholder. A train of oblique shocks in the isolator section decelerates the flow below Mach 1 and facilitates mixing of air and fuel streams. The nearly-homogeneous fuel-air stream then enters an optically-accessible combustor section and passes through an extender with an

air throttle before exiting. A schematic of the flow path in the facility is shown in Fig. 2.1. A small amount of H_2 was initially injected into the cavity to ignite the C_2H_4-air mixture. Measurements were collected at total temperature 1200 K, and total pressure 300 kPa. The local Mach number in the combustor was 0.66 (as calculated by a one-dimensional model of the facility isolator [79]). Fused silica windows on two sides of the combustor section allow optical access. The duct in the combustor section has width 38 mm and height 29 mm. A narrow third window placed on the top wall allows a laser sheet to enter the combustor region with an orientation parallel to the two side windows.

Modular combustor sections can be inserted into the tunnel, enabling the investigation of various flameholder geometries. Two are investigated in this work: the "large-cavity combustor" is a copper insert with a cavity of height 9 mm, and the "small-cavity combustor" is an Inconel 718 insert with a cavity of height 3 mm. Both inserts are actively cooled and incorporate access ports for pressure sensing and temperature measurements. In small cavity tests, the air throttle provided the minimum possible back pressure that maintained a thermally-choked condition, and the global fuel-air equivalence ratio was 0.46. In large cavity tests, the thermal throat was established by a constant area section between the combustor and extender; the air throttle was not used. The global fuel-air equivalence ratio for large cavity tests was 0.41.
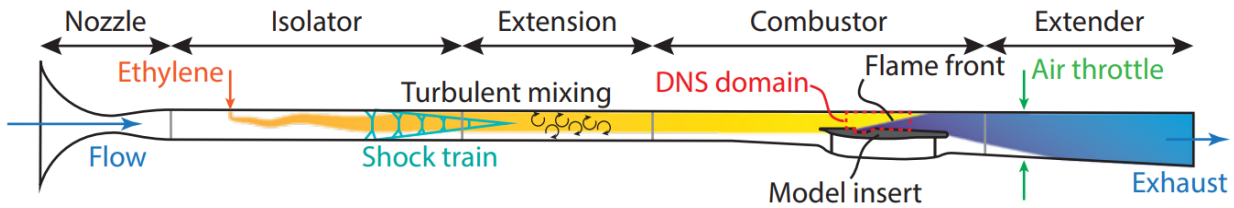
Figure 2.1: Flow path at UVaSCF for small-cavity tests.

2.2.2   Large-cavity combustor

In the large-cavity configuration, the bottom wall of the combustor is a machined copper insert with a cavity flame holder of height $H = 9$ mm and length $L = 54$ mm spanning the

full width of the duct. The distance from the lip of the cavity to the opposite wall is 43.5 mm. A diagram of the large-cavity configuration is shown in Fig. 2.2, and a natural-light image of the cavity-stabilized flame is shown in Fig. 2.3. The coordinate system used in this dissertation for both cavities originates at the intersection of the spanwise centerplane, the plane of the backward facing step, and the leading edge of the cavity. The flow moves in the positive x-direction. The positive y-direction points into the cavity. Positions will be specified relative to this origin, normalized by H.
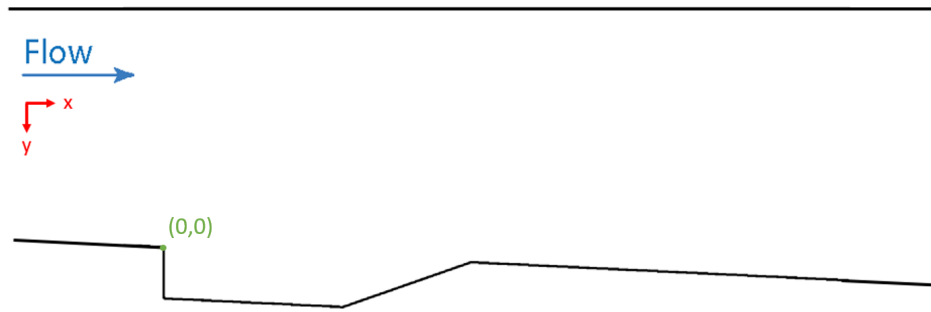
Figure 2.2: Large-cavity combustor, $H = 9$ mm.
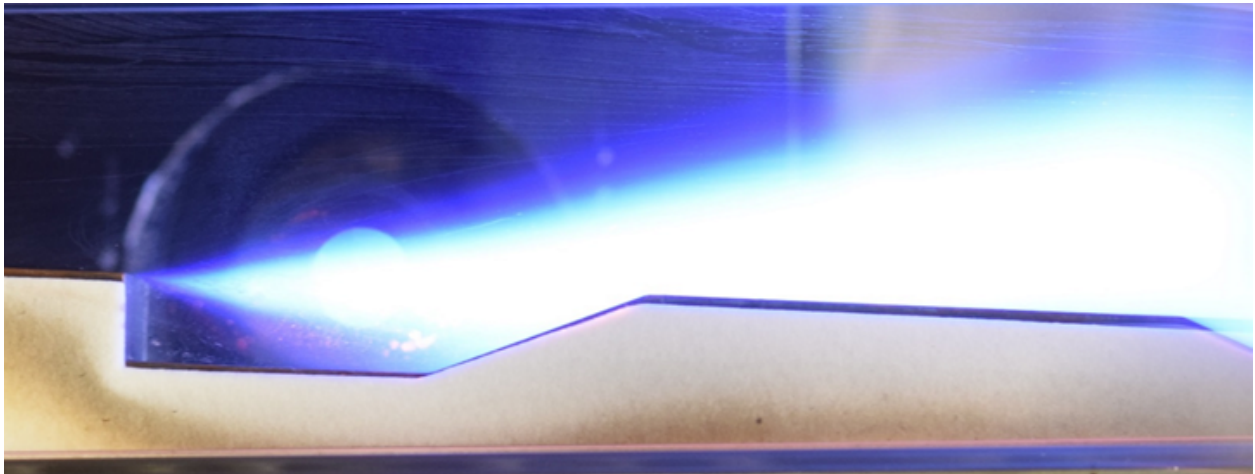
Figure 2.3: Large-cavity flame, natural light image.

Cantu et al. [80] previously studied a premixed C_2H_4-air flame in this flowpath using OH-PLIF. Images were taken in the $x - y$ and $y - z$ planes with a spatial resolution of approximately 300 µm. The flame anchored on the backward-facing step, and spread into the free stream at an approximately-constant angle. Flame intermittency and flame angle

measurements were performed at multiple test conditions, including a base case with high heat release and two cases near flameout conditions; the flame angle varied between 10.4° and 11.3°. Kirik et al. [81] performed PIV on this flowpath using graphite tracer particles and determined that inflow turbulence and shock train position govern flame propagation, and that heat release has only a weak effect. Cutler et al. [64] performed rotational/vibrational nanosecond CARS on this flowpath to measure temperature and major species. Ramesh et al. [82] simulated this configuration using LES/RANS, producing results in reasonable agreement with experiments.

2.2.3   Small-cavity combustor

In the small-cavity configuration, the bottom wall of the combustor is an Inconel 718 insert with a cavity flame holder with length and height scaled by a factor of 1/3 with respect to the large cavity. The insert was produced using direct laser metal sintering; additive manufacturing was necessary due to the complex geometry of the insert, including internal passages for cooling and pressure measurements. The design of the insert is the subject of a paper by Lieber et al. [77]. The cavity has height $H = 3$ mm and length $L = 18$ mm, spanning the full width of the duct. In the $x - y$ plane, the measurement volume is scaled down by a factor of three relative to the large-cavity configuration in order to make DNS computations feasible. The cavity is placed on a strut that divides the combustor flow into two streamtubes; this was necessary to produce a scaled-down measurement domain without severely blocking the flow. A diagram of the small-cavity configuration is shown in Fig. 2.4. Natural light images depicting the ignition sequence of the small-cavity configuration are shown in Fig. 2.5.

This dissertation documents the first OH-PLIF measurements of this cavity configuration. PIV and simultaneous PIV/OH-PLIF measurements were performed concurrently [83], and this flowpath has now been simulated using LES/RANS [9] and DNS [43].
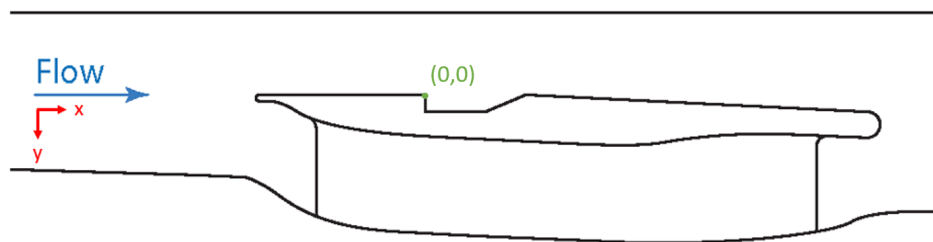
Figure 2.4: Small-cavity combustor, $H = 3$ mm.
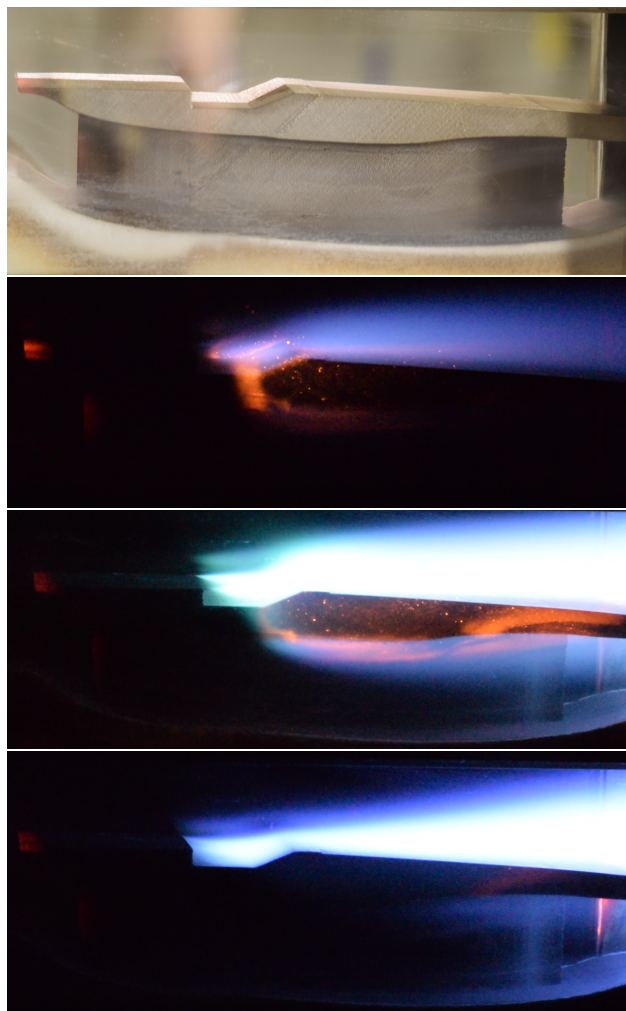
Figure 2.5: Small cavity ignition sequence: (a) No reaction; note glowing leading edge. (b) H_2 flame. (c) Transition from H_2 to C_2H_4. (d) C_2H_4 flame.

2.3 PLIF system

2.3.1 Resolution requirement

The OH-PLIF system described in this section was designed to resolve wrinkles in the flame front at all spatial scales. The smallest flame wrinkles are expected to occur at a scale ten times larger than the Kolmogorov length η [84], which can be estimated [85]:

$$\eta = \left(\frac{\nu}{u}\right)^{3/4} \Lambda^{1/4} \tag{2.1}$$

LES and PIV investigations of the large-cavity experiment have produced estimates for the integral length scale $\Lambda \approx 5$ mm, the root-mean-square velocity $u \approx 50$ m/s, and the kinematic viscosity $\nu \approx 4.5$ m^2/s. As a result, the size of the smallest flame wrinkles is approximately $10\eta \approx 70$ μm. This estimate served as a target resolution for the OH-PLIF system described here.

2.3.2 Laser system

Figures 2.6 and 2.7 depict the optical setup for the experiment. A 20 Hz Q-switched Nd:YAG (QuantaRay, SpectraPhysics) laser beam was frequency-doubled to wavelength 532 nm and used to pump a dye laser (Cobra Stretch, Sirah) circulating Rhodamine 6G dye. The dye laser was set to output light of wavelength 567.10 nm, which was frequency-doubled to 283.55 nm. This wavelength excites the $Q_1(8)$ transition of the $A^2\Sigma^+ \rightarrow X^2\Pi(1,0)$ band of OH. This band provides a high signal-to-noise ratio and is commonly-used for imaging high-speed flows [35, 36]. The $Q_1(8)$ transition was chosen for its relative insensitivity to temperature [39]. At the dye laser exit, the beam had 15 mJ/pulse and was approximately 1 cm in diameter.

A spatial filter was implemented in order to produce a very thin laser sheet waist. This spatial filter was a repurposed entrance slit for a spectrometer. It consists of two steel blades
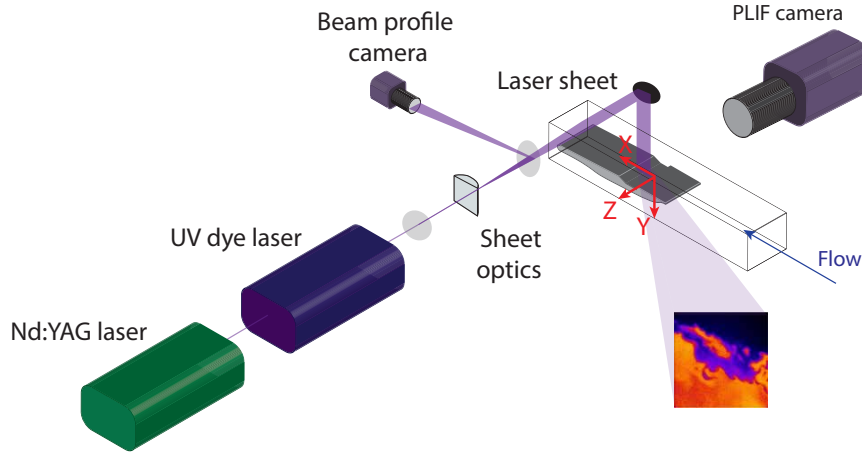
Figure 2.6:   PLIF overview.
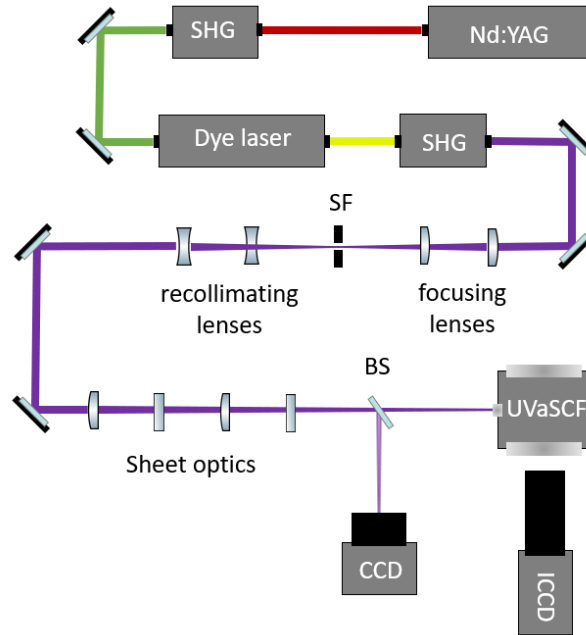
Figure 2.7:   Optical setup for OH-PLIF. UVaSCF flow direction is out of the page.

separated by a gap. The width of the gap is controlled by turning an adjustable knob. The beam passed through a cylindrical lens that focused the beam at the plane of the spatial filter. On the other side of the filter, another cylindrical lens recollimated the beam. By narrowing the gap around the beam focus, the sheet waist could be significantly reduced.

The sheet optics were mounted on a remotely-operated three-axis translation system.

This system was used to move the laser sheet in three dimensions in order to interrogate different regions of the combustor. After the beam passed through sheet optics, a periscope directed the sheet onto the spanwise centerline of the combustor. Before the periscope, a beam splitter directed a weak reflection of the sheet into a CMOS camera (Blackfly, Point Grey) in order to measure the sheet profile. Neutral density filters were used to attenuate the sheet reflection.

For the sheet optics used in the large-cavity experiment, beam profiles were acquired at various settings of the spatial filter knob, as shown in Fig. 2.8. As the aperture width was reduced, non-Gaussian features from the edges of the sheet were removed, resulting in a significantly thinner sheet. The filter was set at 125 µm for OH-PLIF experiments. For the large-cavity experiment, this setting produced a laser sheet waist of approximately 25 µm (as measured by full-width at half-maximum.) Different sheet optics were used in the small-cavity experiment because this optical train was shared by a PIV experiment [83] resulting in a laser sheet waist for the small-cavity experiment of approximately 95 µm.
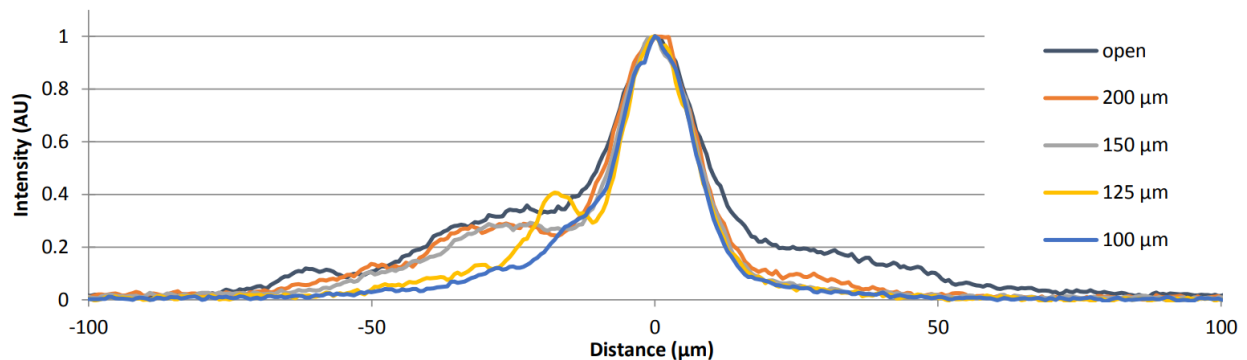
Figure 2.8: Laser sheet intensity profiles at various spatial filter settings for large cavity experiment.

An important quantity for contextualizing fluorescence results is the maximum incident irradiance $I_{\max}$. This can be calculated assuming Gaussian profiles in two spatial dimensions (sheet height and thickness) and in time. This serves only as an approximation; a non-Gaussian variation in intensity along the sheet height is observed for the small-cavity experiment, and will be discussed in Section 2.5. The calculation requires knowledge (or estimation) of the

energy per pulse at the flowfield and the full width at half maximum (FWHM) values of the sheet height, sheet thickness, and time. The standard deviation of each Gaussian profile is related to the respective FWHM [86]:

$$\text{FWHM} = 2\sqrt{2\ln2}\sigma \tag{2.2}$$

The laser pulse power $P(t)$ is a Gaussian function in time with standard deviation σ_t and peak power P_{max}:

$$P(t) = P_{\text{max}} \exp\left(\frac{-t^2}{2\sigma_t^2}\right) \tag{2.3}$$

The time-integral of the pulse power is the energy per pulse, and involves the Gaussian error function (erf):

$$E = \int_{-\infty}^{\infty} P(t)dt = \sqrt{\frac{\pi}{2}}P_{\text{max}}\sigma_t \ \text{erf}\left(\frac{t}{\sqrt{2}\sigma_t}\right)\Bigg|_{-\infty}^{\infty} = \sqrt{2\pi}P_{\text{max}}\sigma_t \tag{2.4}$$

Peak power can be obtained as a function of energy per pulse and pulse standard deviation in time:

$$P_{\text{max}} = \frac{E}{\sqrt{2\pi}\sigma_t} \tag{2.5}$$

The laser irradiance $I(y,z)$ (with units of power per area) is a two-dimensional Gaussian function with peak irradiance I_{max} and spatial standard deviations σ_x and σ_y:

$$I(y,z) = I_{\text{max}} \exp\left[-\left(\frac{y^2}{2\sigma_y^2} + \frac{z^2}{2\sigma_z^2}\right)\right] \tag{2.6}$$

As in the cavity coordinate system, y is the dimension of the sheet height, and z is the dimension of the sheet thickness. The origin for these coordinates is the center of the sheet, where irradiance is greatest. When $t = 0$ and the pulse power is at its peak value, the integral over all area of the irradiance is equal to the peak power:

$$P_{\text{max}} = \int_{-\infty}^{\infty} \int_{-\infty}^{\infty} I(y,z) dy dz = \frac{\pi}{2} I_{\text{max}} \sigma_y \sigma_z \, \text{erf} \left(\frac{y}{\sqrt{2}\sigma_y} \right) \Big|_{-\infty}^{\infty} \text{erf} \left(\frac{z}{\sqrt{2}\sigma_z} \right) \Big|_{-\infty}^{\infty} = 2\pi I_{\text{max}} \sigma_y \sigma_z \tag{2.7}$$

Finally, peak irradiance can be determined as a function of peak power and spatial standard deviations.

$$I_{\text{max}} = \frac{P_{\text{max}}}{2\pi \sigma_y \sigma_z} \tag{2.8}$$

The irradiance is related to the excitation rate W of the species targeted for LIF [87]:

$$W_{lu}(t, \nu_L) = I(t) \frac{B_{lu}}{c} \hat{g}(\nu_L, T, p) \tag{2.9}$$

Here, l and u refer to the lower and upper energy states of the LIF process, c is the speed of light, and B is the Einstein B-coefficient. The laser overlap integral $\hat{g}$ can be calculated using a method from Carter and Lee [88], with the assumption of a Gaussian laser lineshape:

$$\hat{g}(\nu_L, T, p) = \frac{1}{\sqrt{1 + \alpha(T)^2}} \frac{2\sqrt{\ln(2)}}{\sqrt{\pi}\Delta\nu_D(T)} V \left[\frac{2\sqrt{\ln(2)}\nu_L/\Delta\nu_D(T)}{\sqrt{1 + \alpha(T)^2}}, \frac{a(T,p)}{\sqrt{1 + \alpha(T)^2}} \right] \tag{2.10}$$

Here, V is the Voigt function:

$$V(u, v) = \frac{v}{\pi} \int_{-\infty}^{\infty} \frac{e^{-w^2}}{v^2 + (u-w)^2} dw \tag{2.11}$$

The parameters $a(T, P)$ and $\alpha(T)$ are given by:

$$a \approx \sqrt{\ln(2)} \Delta\nu_C / \Delta\nu_D \tag{2.12}$$

and

Table 2.1: Mole fractions of major collisional partners of OH, from DNS simulation of the scramjet flame [42].

Species	X_i
H_2O	0.05
CO_2	0.05
N_2	0.76
O_2	0.12

$$\alpha(T) = \Delta\nu_L/\Delta\nu_D(T) \tag{2.13}$$

Here, $\Delta\nu_L$ is the FWHM of the laser line. $\Delta\nu_C$ is the linewidth associated with elastic dephasing collisions, dependent on the dephasing collision rate coefficient Q_C:

$$\Delta\nu_C = \sum_i 2\gamma_{i,0} \cdot p \cdot X_i \cdot \left(\frac{T_{\text{ref}}}{T}\right)^{n_i} \tag{2.14}$$

Here, $\gamma_{i,0}$ are broadening coefficients (in $\text{cm}^{-1}/\text{atm}$) for species i at a reference temperature T_{ref}. p is the local pressure, X_i are mole fractions, and n_i are empirical power-law variables for temperature variation [89, 90]. Mole fractions for major collisional broadening partners (H_2O, CO_2, N_2, and O_2) in the current flame (according to DNS results [42]) are provided in Table 2.1. Relevant broadening parameters are shown in Tables 2.2 and 2.3. The values reported in these tables correspond to the transitions studied in the literature that are the closest available (in branch and ΔJ) to the transition used in this work for OH-PLIF; however, all published studies refer to the $(0,0)$ band and not the $(1,0)$ band. No studies have been performed to produce similar parameters for other broadening partners, so broadening due to other species is assumed to be negligible. The broadening parameters are significantly uncertain, therefore the computed value of $\Delta\nu_C$ can only be treated as a rough estimate.

$\Delta\nu_D$ is the Doppler linewidth, which can be calculated using the central frequency of the transition ν_0, the Boltzmann constant k_B, the atomic mass unit constant m_u, and the molecular weight of the target species M.

Table 2.2: Collisional broadening coefficients for OH $A^2\Sigma^+ \rightarrow X^2\Pi(0,0)$ $Q_1(6.5)$ at $T = 1220$ K [91].

Species	$2\gamma_{i,0}$ [cm^{-1}/atm]
H_2O	0.237 ± 0.008
CO_2	0.064 ± 0.004
N_2	0.060 ± 0.004
O_2	0.042 ± 0.004

Table 2.3: Collisional broadening temperature dependencies for OH $A^2\Sigma^+ \rightarrow X^2\Pi(0,0)$.

Species	n_i	Transition	Reference
H_2O	0.035 ± 0.3	$R_1(8.5)$	[89]
CO_2	1.7 ± 0.5	$R_1(8.5)$	[89]
N_2	0.6 ± 0.3	$Q_1(5.5)$	[91]
O_2	unknown, assumed 0	N/A	N/A

Table 2.4: Laser sheet characteristics

Variable	Value	Units	Notes
FWHM$_t$	8.5 ± 2	[ns]	Based on Quanta-Ray specifications
FWHM$_y$	10	[mm]	Estimated
FWHM$_z$	0.095	[mm]	Measured

$$\Delta\nu_D(T) = \nu_0\sqrt{\frac{8k_BT\ln(2)}{m_uMc^2}} \qquad (2.15)$$

Equations (2.2) - (2.15) enable the calculation of the maximum excitation rate that occurs during the LIF process. Measured and estimated characteristics of the laser sheet are provided in Table 2.4. Tables 2.5 and 2.6 show necessary input values and constants. Table 2.7 provides the calculated excitation rate and several intermediate quantities. The resulting value of $W_{lu,\max} = 2.05 \cdot 10^{11}$ s^{-1} far exceeds the rate of electronic quenching $Q_e \approx 5 \cdot 10^8$ s^{-1} [88]. As a result, these experimental measurements fall in a strongly-saturated LIF regime. This verification of LIF transition saturation is necessary to produce appropriate simulated PLIF images from simulation results for comparison to the experiment, as discussed in Chapter 4.

Table 2.5: Excitation rate calculation input values

Variable	Value	Units	Notes
E	8	[mJ]	
σ_t	3.6 ± 0.8	[ns]	
σ_y	4.2	[mm]	
σ_z	0.040	[mm]	
B_{lu}	$9.86 \cdot 10^8$	$[\mathrm{m}^2/(\mathrm{Js})]$	[88]
$\Delta\nu_L$	0.1	$[\mathrm{cm}^{-1}]$	
M_{OH}	17	$[-]$	
T	1500	[K]	From DNS measurements, see Chapter 4
ν_0	35270	$[\mathrm{cm}^{-1}]$	Corresponds to 283.55 nm

Table 2.6: Excitation rate calculation constants

Variable	Value	Units
k_B	$1.38 \cdot 10^{-23}$	[J/K]
m_u	$1.66 \cdot 10^{-27}$	[kg]
c	$3.00 \cdot 10^8$	[m/s]

Table 2.7: Excitation rate calculation output values

Variable	Value	Units	Equation
$\Delta\nu_C$	0.1	$[\mathrm{cm}^{-1}]$	2.14
$\Delta\nu_D$	0.24	$[\mathrm{cm}^{-1}]$	2.15
α	0.42	$[-]$	2.13
a	0.35	$[-]$	2.12
$\hat{g}$	2.62	[cm]	2.10
$P_{\max}$	$8.87 \cdot 10^5$	[W]	2.5
$I_{\max}$	$2.10 \cdot 10^8$	$[\mathrm{W/cm}^2]$	2.8
$W_{lu,\max}$	$1.81 \cdot 10^{11}$	$[\mathrm{s}^{-1}]$	2.9

2.3.3   Camera system

OH-PLIF images were taken using an intensified CCD camera (PI-MAX 4, Princeton Instruments). The camera was mounted on the same three-axis translation system as the laser sheet optics such that the focus of the laser sheet remained centered in the field of view as the sheet moved. A fourth translation stage allowed the camera to remotely translate closer to and further away from the laser sheet. This stage was used to make focusing movements of $o(1 \text{ mm})$ remotely, during facility operation.

A 100 mm focal length $f/2.8$ ultraviolet camera objective (2178, CERCO) was mounted

on the camera with extension tubes. The lens contained a bandpass filter (FF02-320/40, Semrock) to admit light from 310 to 340 nm. This filter admitted OH-PLIF signal while blocking laser reflections and other interferences. The resolution and performance of the camera system were evaluated using a glass resolution target (USAF-1951) backlit by an ultraviolet LED light source (LM2X-DMHP, ISSI). This resolution target presents line groups in a range of sizes; the lines are alternately transparent and opaque. Images were taken of this target using three total lengths of extension tubes: 76.2 mm, 152.4 mm, and 203.2 mm. An image of the target taken in the first configuration is shown in Fig. 2.9.
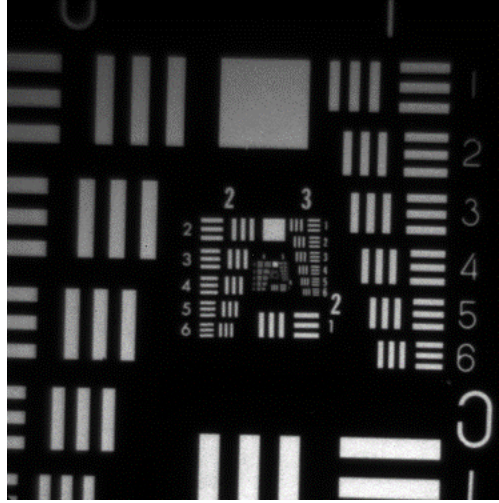
Figure 2.9: USAF-1951 resolution target.

The resolution of a camera system can be determined by determining line group contrast as a function of line size, known as a modulation transfer function [92]. Minimum and maximum pixel intensities were determined for each line group i with line size l_i and used to determine modulation values m_i according to Eq. (2.16). A baseline modulation value m_0 was determined from the bright square visible in Fig. 2.9 and the surrounding dark background. The modulation transfer function was determined according to Eq. (2.17). A "resolution limit" was defined conservatively for the system as a length scale l_r such that $F(l_r) = 0.5$. This process of obtaining modulation transfer functions and resolution limits was repeated for all three extension tube configurations.

$$m_i = \frac{I_{\text{max}} - I_{\text{min}}}{I_{\text{max}} + I_{\text{min}}} \tag{2.16}$$

$$F\left(l_i\right) = \frac{m_i}{m_0} \tag{2.17}$$

Image magnification M was recorded for all three configurations; as expected from ray optics, M grew linearly with extension tube length. Pixel intensity I decreased with M, in reasonable agreement with the theory [93] given in Eq. (2.18).

$$I \propto (M+1)^{-2} \tag{2.18}$$

The product of the resolution limit and magnification was observed to be approximately constant, as shown in Eq. (2.19). For the present lens and camera, this relationship allows the in-plane resolution of the system to be estimated based on the magnification produced at a given extension tube length and focus setting.

$$l_r \cdot M = 77 \ \mu\text{m} \tag{2.19}$$

The magnification of the final PLIF setup was determined by imaging a millimeter-grid dotcard that was illuminated at a very shallow angle by the laser sheet. Camera exposures were binned 2×2 due to camera bandwidth limits, producing 512×512-pixel images. Each pixel recorded a grayscale intensity value as a 16-bit integer. Nd:YAG flashlamps, Q-switch, and PI-Max exposure were all timed using an LC-880 experiment controller. While the laser pulsed at 20 Hz, images were captured at 10 Hz due to camera bandwidth limits.

2.4   Large-cavity PLIF results

Images taken for the large-cavity configuration had magnification 1.91, producing a field of view 6.86 mm $\times$ 6.86 mm. Images were taken while the translation system's x-axis motor

was in motion. The camera travelled along the x-axis at 0.25 mm/s, producing 40 images for ever millimeter travelled. Six x-direction sweeps were acquired from $x/H = 0$ to 14.10 and from y/H = -2.41 to 1. Most (x, y) point locations were measured 275 times. Approximately 14,000 images were acquired. Additional "background" images were acquired with the laser blocked. Selected background-corrected PLIF images are shown in Fig. 2.10; a compilation of images across the experimental domain are shown in Fig. 2.11. Figure 2.12 shows the number of PLIF acquisitions taken at each point in the domain. Mean and standard deviation OH-PLIF signal levels are shown in Figs. 2.13 and 2.14, respectively.
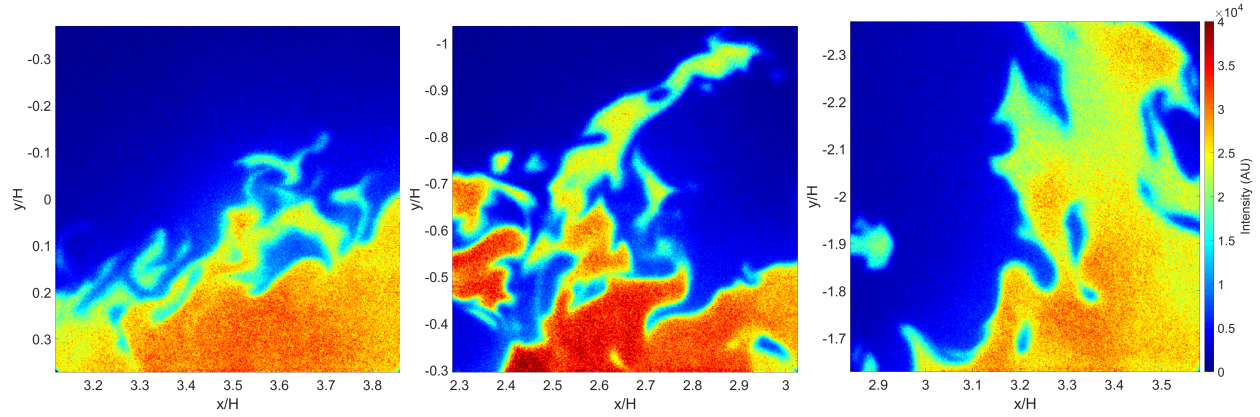
Figure 2.10: Single OH-PLIF images of the small-scale cavity flameholder (arbitrary units).
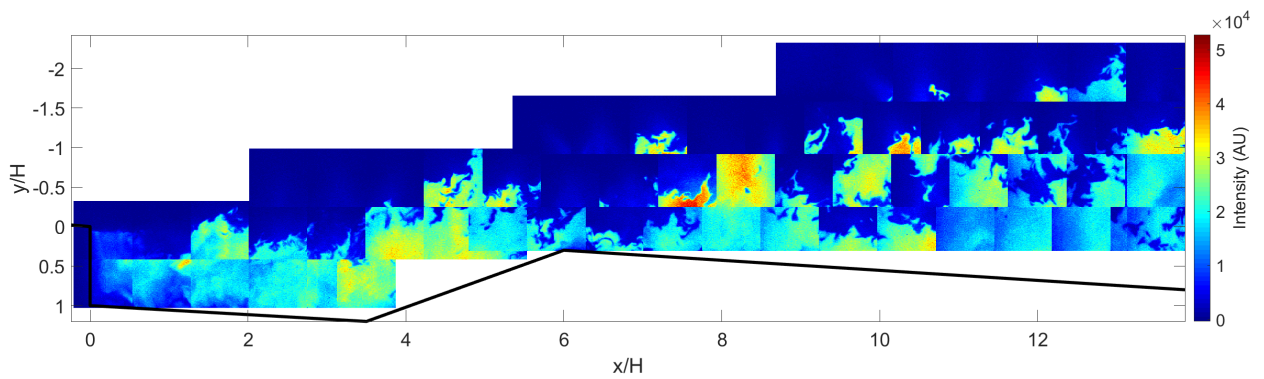
Figure 2.11: Compilation of single-shot OH-PLIF images (arbitrary units).
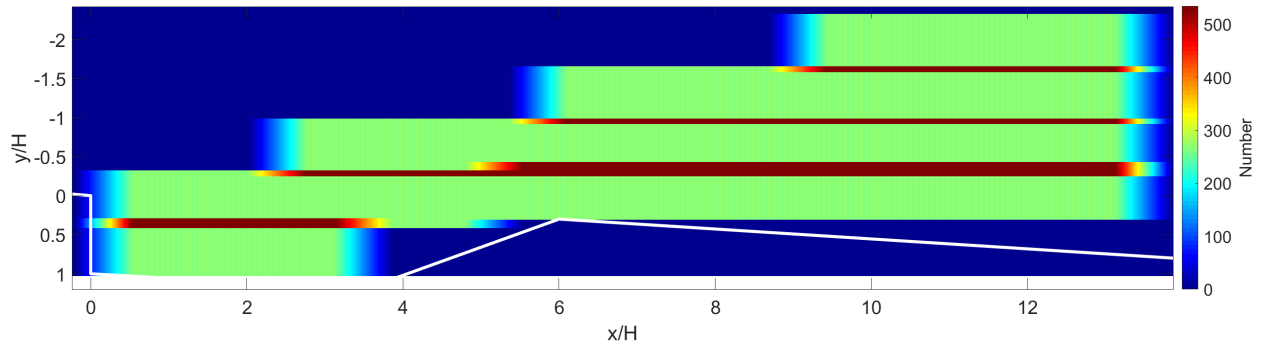
Figure 2.12: Number of OH-PLIF acquisitions performed at each pixel location.
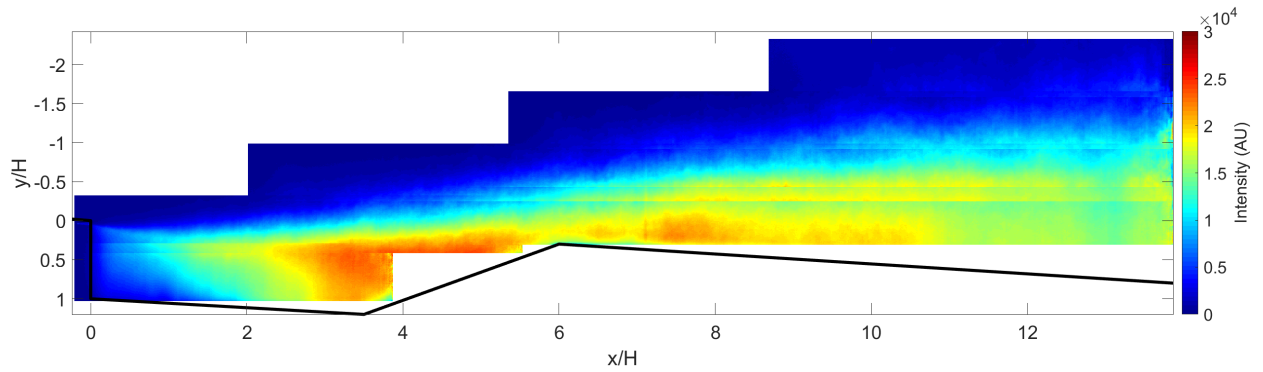
Figure 2.13: Mean OH-PLIF signal (arbitrary units).
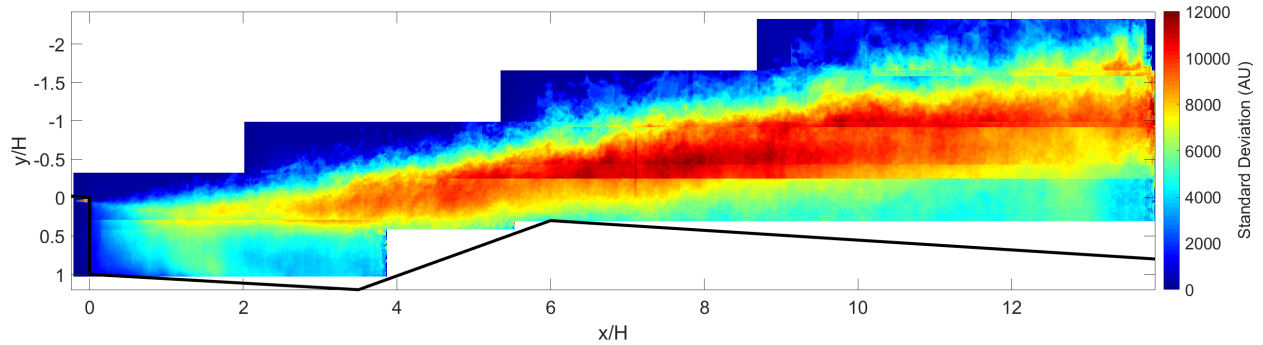
Figure 2.14: Standard deviation of OH-PLIF signal (arbitrary units).

2.5   Small-cavity PLIF results

Images taken for the small-cavity configuration had magnification 2.34, producing a field of view 5.6 mm × 5.6 mm. Camera exposures were 200 ns long at 52% of maximum intensifier gain. After the flame was established in the facility, one thousand images were captured

at each of nineteen different fields of view, spanning $x/H = 0$ to 15 and y/H = -4 to 1, as shown in Fig. 2.15. Acquiring images with stationary fields of view was possible for the small-cavity configuration because of the smaller domain; it would have been infeasible for the large-cavity configuration. Occasionally, adjustments on the order of one millimeter were made to the camera focus stage to obtain the sharpest possible image. Additional "lightfield" images were taken at each field of view with the flame off.
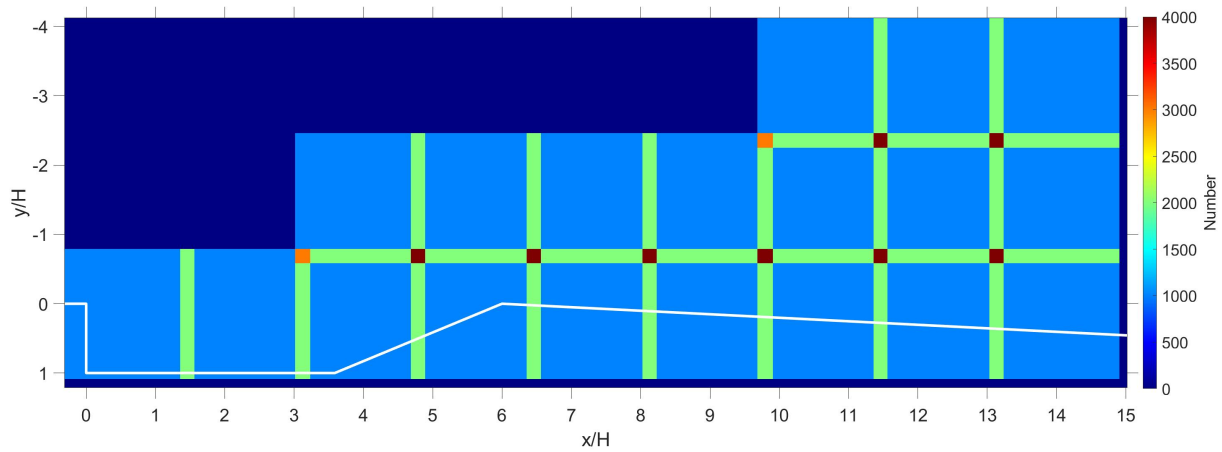
Figure 2.15: Number of OH-PLIF acquisitions performed at each pixel location.

Two corrections were applied to the acquired images. First, a mean lightfield image was computed for each field of view and subtracted from the corresponding PLIF images. Next, because the laser sheet intensity was observed to vary along its height, beam profile images were used to compute laser sheet intensity as a function of x-position within the field of view. All PLIF images were normalized using this function to correct for variations in sheet intensity. Post-correction qualitative OH-PLIF images are shown in Figs. 2.16 and 2.17.

Data from OH-PLIF images were mapped onto a 4187 $\times$ 1457-pixel matrix that spanned the entire measurement domain from $x/H = 0$ to 15 and y/H = -4 to 1. OH-PLIF signal
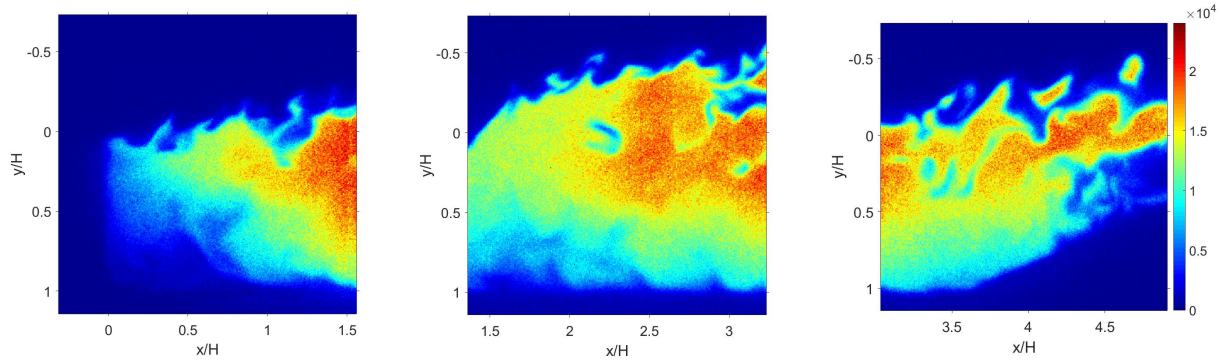
Figure 2.16:   Single OH-PLIF images of the cavity flameholder (arbitrary units).
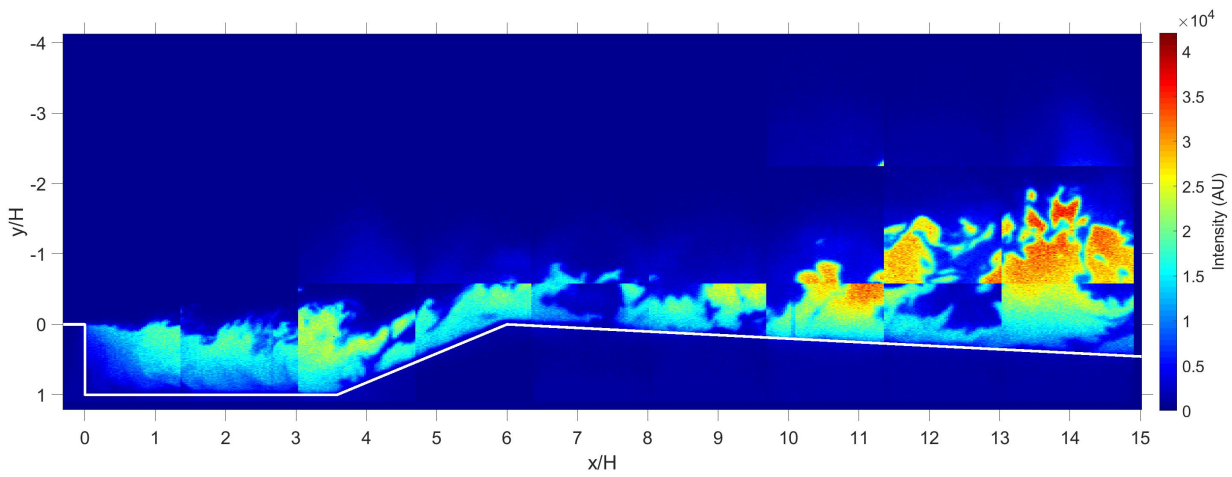
Figure 2.17: Compilation of single-shot OH-PLIF images (arbitrary units).

intensity mean and standard deviation are shown in Figs.   2.18 and   2.19, respectively.

The flame spreads into the main flow at an approximately-constant angle, consistent with

OH-PLIF from large cavity measurements. However, unlike the large cavity measurements,

there is a significant region of decreased OH-PLIF signal intensity from $x/H = 5$ to 8, near

the trailing edge of the cavity. Here, the flow accelerates over the aft ramp of the cavity

and then decelerates over the diverging wall downstream of the cavity. It is hypothesized

that the high shear strain rates in this area cause local reduction in OH concentration. At

high strain, chemical reaction rates become small in comparison to thermal diffusion and

mass diffusion rates, decreasing the concentration of product species. Cutler et al. [64]

performed one-dimensional calculations for a laminar premixed opposed jet C_2H_4-air flame

and demonstrated a decrease in CO concentration with increasing strain rate; similar decreases are expected for other intermediate combustion products such as OH. Significant changes in temperature or pressure could also cause OH-PLIF signal to decrease [25]; however, hybrid LES/RANS results [9] do not predict large local variations in temperature or pressure within the burned gas in this region. The flame recovers and OH-PLIF signal increases again for $x/H > 8$.
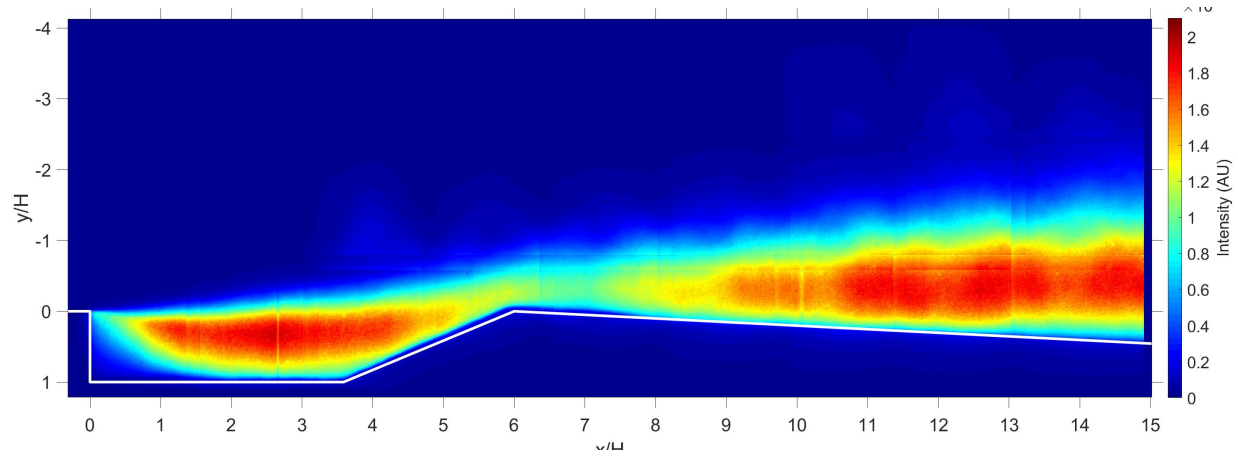
Figure 2.18: Mean OH-PLIF signal (arbitrary units).
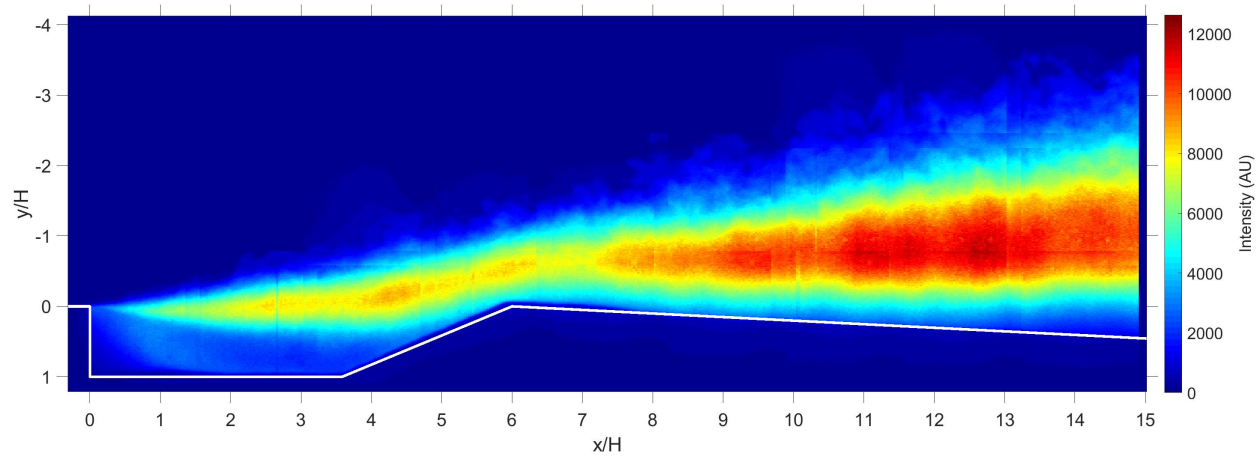
Figure 2.19: Standard deviation of OH-PLIF signal (arbitrary units).

2.6 Summary

The structures of turbulent compressible premixed C_2H_4-air flames were imaged using a high-spatial-resolution OH-PLIF system. Both a wall-mounted cavity of height $H = 9$ mm and a scaled-down strut-mounted cavity of height $H = 3$ mm were studied. For the small cavity, two-dimensional single-shot images were captured along the centerplane of the duct, from $x/H = 0$ to 15 and $y/H = $ -4 to 1, using nineteen different fields of view of size 5.6 mm $\times$ 5.6 mm. OH-PLIF intensity measurements were compiled for this domain using a light sheet with FWHM 95 μm. For the large cavity, images were captured from $x/H = 0$ to 13 and $y/H = $ -2.3 to 1, using fields of view 6.9 mm $\times$ 6.9 mm and a light sheet with FWHM 25 μm. For both configurations, the expected in-plane resolution of the images was 40 μm $\times$ 40 μm.

The resulting ensemble of OH-PLIF images resolved flame structures expected under current flow conditions. The results demonstrate a flame anchored on a recirculation region generated by the cavity flameholder; the turbulent mixing of premixed reactants and product species controls the combustion process and the spread of the flame. The images exceed the spatial resolution of any published results under similar conditions.

Chapter 3

Flame front characterization for cavity-stabilized flames

3.1 Motivation and objectives

The qualitative nature of the OH-PLIF images presented in the previous chapter presents an obstacle for the interpretation of the experimental results. Quantitative metrics are required to place these results in context with computational efforts describing cavity-stabilized flames, as well as the broader literature describing premixed flames. In particular, metrics are needed to facilitate direct comparison between experimental OH-PLIF images and computational DNS outputs.

With this goal in mind, a set of tools has been developed to describe the morphology of the flame front in OH-PLIF images. First, an automated method identifies the position of the flame front based on regions of high OH gradient. Then, the flame fronts are processed to obtain flame intermittency, flame front curvature, and other metrics. These metrics are used to compare the small-cavity flame with premixed flames from the literature and examine similarities and differences between the large- and small-cavity flames.

The image processing algorithm and results are presented first for the small-cavity

Table 3.1: Image processing variables.

Filter	Coefficient	Value
Anisotropic diffusion filter	N	15
	Δt	1/7
	$\mathcal{K}$	20
Gradient image threshold	t_1	95%
PLIF intensity threshold	t_2	10%

configuration in Sections 3.2–3.5. Large-cavity results (and algorithm modifications necessary for large-cavity data processing) are then presented in Section 3.6.

3.2 Image binarization

An automated MATLAB script was developed to binarize OH-PLIF images into "burned" and "unburned" regions. Burned regions have high OH-PLIF signal and are expected to consist largely of combustion products. Unburned regions have low OH-PLIF signal and are expected to consist mostly of reactants. This is based in part on the method described in [94]; several modifications were necessary to accommodate high-spatial-resolution images. The process used several variables that were varied by trial-and-error until the script-defined flame front matched the boundary between regions of high and low OH-PLIF signal visible to the eye. These variables are listed in Table 3.1.

3.2.1 Filtering

First, the image was converted to double precision. The image was passed through a median filter using a 3×3 pixel window to smooth noise. An anisotropic diffusion filter [95, 96] was then applied. This filter diffuses a matrix of image intensity values $I(x, y, t)$ over a timestep Δt using a diffusion coefficient $c(x, y, t)$. The diffusion coefficient is chosen to be a function of the magnitude of the intensity gradient and a constant $\mathcal{K}$; this has the effect of smoothing noise while preserving edges. This process is described in Eqs. (3.1) and (3.2), in which "div"

represents the divergence operator, Δ represents the gradient operator, and ∇ represents the Laplacian operator.

$$\frac{\partial I}{\partial t} = \mathrm{div}\,(c\nabla I) = c\Delta I + \nabla c \cdot \nabla I \tag{3.1}$$

$$c\,(x, y, t) = e^{-(\|\nabla I\|/K)^2} \tag{3.2}$$

The resulting image will be referred to as the "intensity image"; an example is shown in Fig. 3.1.
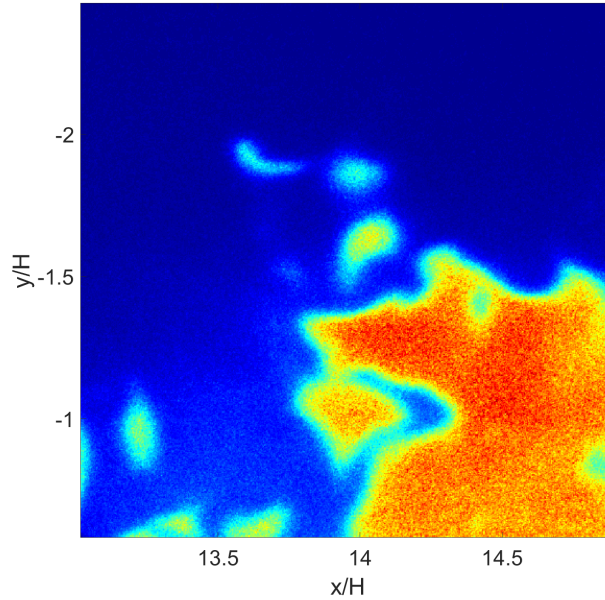
Figure 3.1: Intensity image.

3.2.2   Threshold selection

The two-dimensional gradient of PLIF intensity is a useful tool for discerning the flame front. At the flame front, the pixel intensity changes rapidly in space, resulting in high gradient values. The gradient of the PLIF image was approximated using the Sobel method [97] through the following steps. Matrices of approximate gradient values in the x- and

y-directions, G_x and G_y, are computed by convolving the PLIF image with two 3×3 kernels, as shown in Eqs. (3.3) and (3.4).

$$G_x = \begin{bmatrix} 1 & 0 & -1 \\ 2 & 0 & -2 \\ 1 & 0 & -1 \end{bmatrix} * I \tag{3.3}$$

$$G_y = \begin{bmatrix} 1 & 2 & 1 \\ 0 & 0 & 0 \\ -1 & -2 & -1 \end{bmatrix} * I \tag{3.4}$$

The magnitude G of the gradient can be found through vector addition, as shown in Eq. (3.5).

$$G = \sqrt{G_x^2 + G_y^2} \tag{3.5}$$

This result will be referred to as the "gradient image"; an example is shown in Fig. 3.2.
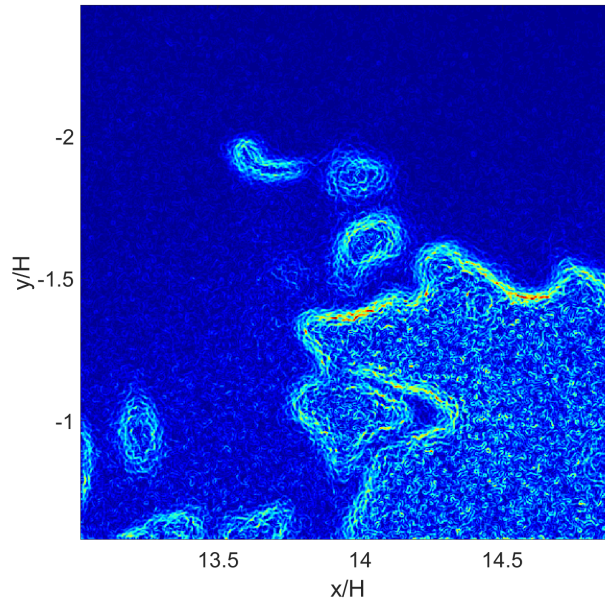
Figure 3.2: Gradient image.

The highest gradient values were isolated using a 95th percentile threshold; a list of all gradient image pixels with values higher than the threshold was compiled. This was used to create a list of intensity image values for the same pixel locations. The tenth percentile of this list was used as a threshold for intensity image binarization. Pixels with values greater than the threshold were set to 1; this was defined as the "burned" area. Other, "unburned" pixels were set to 0. The shape of the burned region was smoothed using morphological closing [98]. This result is the "binary image"; an example is shown in Fig. 3.3.
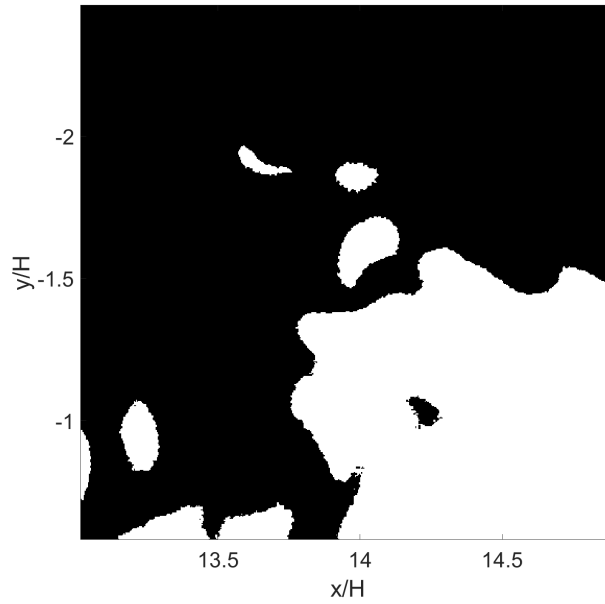
Figure 3.3: Burned area image.

3.3 Flame intermittency

3.3.1 Calculation

The intermittency of the cavity-stabilized flame was calculated; the process is described next. Intermittency $\mathcal{I}$ is defined [80] as the probability that OH is present at a given point; this probability varies over the spatial domain. For each (i, j) pixel location, intermittency is the

proportion of images in which significant OH-PLIF signal (as specified by the binary images) exists at that pixel, as shown in Eq.(3.6).

$$\mathcal{I}(i,j) = P(\text{burned})\big|_{i,j} \tag{3.6}$$

Other works [99] refer to a quantity called mean progress variable $\bar{c}$ which describes the time-averaged reactedness at a given position from 0 (pure reactants) to 1 (pure products). This terminology is avoided here because OH is an intermediate product, and simulations performed on the facility reveal regions of significant heat release inside regions of OH [9, 43]; therefore the presence of OH does not indicate that the reaction is complete.

Intermittency values across the small-cavity domain are shown in Fig. 3.4. This is a graph of the probability of the presence of OH, and by analogy, combustion products; it provides a visual representation of the spatial envelope in which the flame exists. Within the cavity, immediately downstream of the step, from about $x/H = 0.5$ to 4.5, there is a region where intermittency is equal to one, meaning combustion products are always present. Downstream of the cavity, intermittency values are always less than one. In particular, at the end of the cavity ramp, where the flow accelerates with high shear, the probability of significant OH presence is reduced relative to values upstream and downstream.
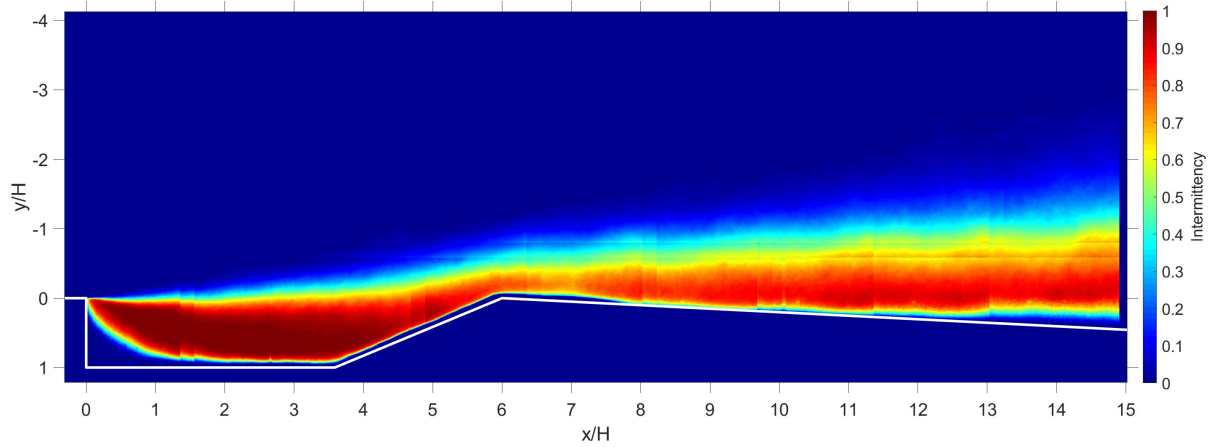
Figure 3.4: OH-PLIF signal intermittency.

Lieber [83] presented simultaneous PIV/OH-PLIF measurements on the same flowpath and also observed low intermittency at the cavity aft ramp. The study also demonstrated that the majority of mass flux out of the cavity occurs at the aft ramp. Based on these observations and instantaneous PIV/OH-PLIF acquisitions, Lieber proposed the existence of an unsteady combustion cycle in which mass is intermittently ejected at the aft ramp; reactants are entrained into the region between ejection events. Lieber suggested, without direct evidence, that this ejection cycle was connected to thermoacoustic oscillations between the shock train and the thermal throat, which have been measured in other scramjet facilities [100, 101]. The reduction in intermittency seen in Fig. 3.4 could be associated with such a thermoacoustic cycle; temporally-resolved measurement techniques would be necessary to investigate the phenomenon further.

3.3.2   Flame brush

Figure 3.5 shows how different flame regions, including the flame brush, can be defined based on intermittency values. Region A comprises all areas with $\mathcal{I} < 5\%$. In the main duct, these are areas where combustion products are rarely or never present. There is also a low-intermittency region in the cavity; this is likely a region of combustion products in which all OH has been consumed. Region B has $\mathcal{I} > 95\%$, where combustion products (and OH radicals) are nearly-always present. The remaining regions have $5\% < \mathcal{I} < 95\%$. Region C, near $x/H = 0$, is the area where the flame anchors to the backward-facing step. Region D, near the cavity wall, is characterized by diffuse OH signal without a sharp boundary. Here, OH generated at the flame front is reaching the end of its lifetime and being consumed. Finally, Region E is the flame brush, located at the shear layer emanating from the backward-facing step.

A coordinate system based on the flame brush is useful for describing flame front metrics. The flame brush region is bisected by a contour of $\mathcal{I} = 50\%$, which approximates a straight line emanating from the cavity leading edge and propagating into the main flow at an angle

of 3.87° to x. A rotated coordinate system is defined based on this contour: x' and y' are equal to x and y rotated 3.87° counterclockwise about z, such that x' bisects the flame brush. x' is then the direction of the flame brush and y' is the direction normal to the flame brush. The y'-direction thickness of the flame brush is shown as a function of x'/H in Fig. 3.6. With increasing x', the brush thickness increases steadily, with a slight decrease at trailing edge of the cavity.
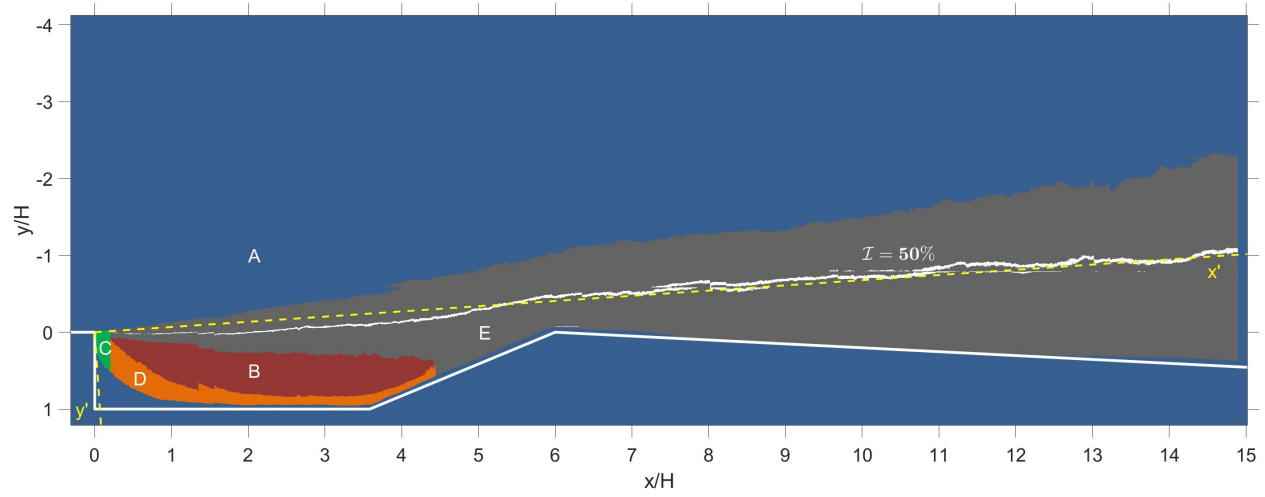
Figure 3.5: Flame intermittency regions. A: low-intermittency region. B: high-intermittency region. C: flame anchoring region. D: OH consumption region. E: flame brush.
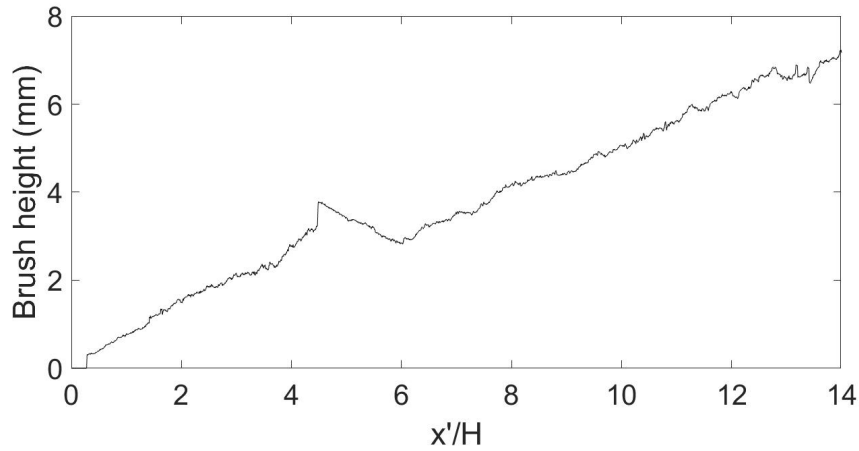
Figure 3.6: Variation of flame brush thickness with downstream distance.

Intermittency data also permits an evaluation of the flame angle, or the angle at which the flame tends to propagate away from the backward-facing step, relative to the free stream direction. The outer bound of the flame brush (corresponding to the $\mathcal{I} = 5\%$ contour) was used to calculate flame angle; the line of best fit through this contour is angled at 8.75°.

3.4 Flame surface density

3.4.1 Calculation

The burned area images were processed to isolate the flame front. The interior of the burned region was removed, leaving a one-pixel-wide outline circumscribing the burned area. The result was an image in which pixels with a value of 1 formed one or more loops circumscribing the burned region. These pixels all lay on the flame front, the cavity wall, or the image border. Pixels at the image border and near the cavity wall were removed. After removing any other spurious pixels, only pixels on the flame front remained. This result is the "flame front image." A subsection of an OH-PLIF image is displayed with the detected flame front overlaid in Fig. 3.7.

Flame surface density is the ratio of the surface area of the flame to the volume that the flame occupies. OH-PLIF images provide a two-dimensional "slice" of the flame; the flame surface density in OH PLIF images can be approximated as the ratio of flame front length to image area [102]. For any two-dimensional window within an image, the local flame surface density can be approximated as the ratio of the length l of the flame front within the window and the area A of the window. The local mean value of flame surface density Σ at any pixel location (i, j) is average of this ratio evaluated for all possible windows b that contain (i, j), for all images k:

$$\Sigma\left(i, j\right) = \frac{1}{BK} \sum_{b=1}^{B} \sum_{k=1}^{K} \frac{l}{A} \tag{3.7}$$
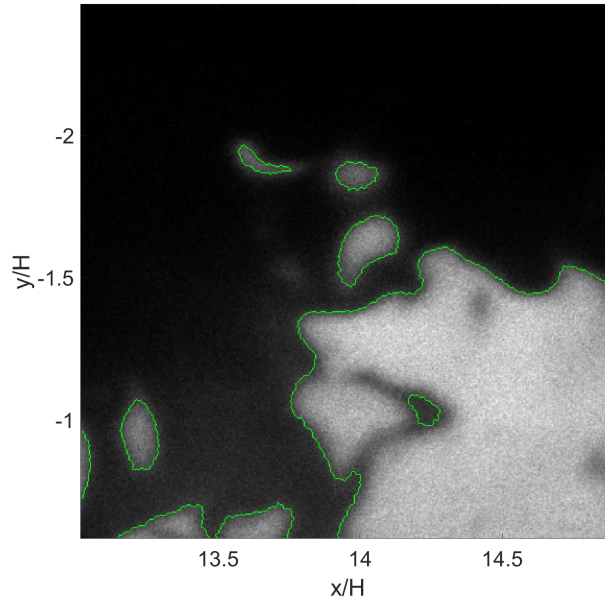
Figure 3.7: Flame front (green) overlaid on intensity image (grayscale).

For a perfectly laminar flame, the flame front would trace a straight line through the image, and the ratio of flame front length to image area would be small. A more turbulent flame front would include wrinkled and distributed flame regions, and therefore higher flame surface density. Increasing flame surface density is associated with an increase in u'/S_L, the ratio of mean streamwise velocity fluctuations to the laminar burning velocity [102, 99].

Flame surface density was calculated using 2×2-pixel windows. The method used to determine flame front length inside a window is shown in Fig. 3.8. If the window contained no flame front pixels, the flame front length was zero. A window with one, three, or four flame front pixel had a flame front length of one, three, or four pixels, respectively. A window with two flame front pixels had a flame front length of two pixels if they were connected horizontally or vertically or $2\sqrt{2}$ pixels if they were connected diagonally. The distribution of Σ values across the measurement domain is shown in Fig. 3.9.

Bell et al. [103] calculated two-dimensional and three-dimensional values for Σ for a turbulent premixed Bunsen flame. These results indicated that the approximate two-dimensional Σ values that may be calculated from PLIF images should be multiplied by a
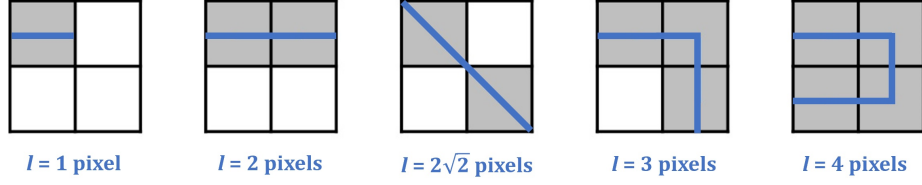
Figure 3.8: Flame front length counting in 2×2 windows. Flame front pixels in grey.
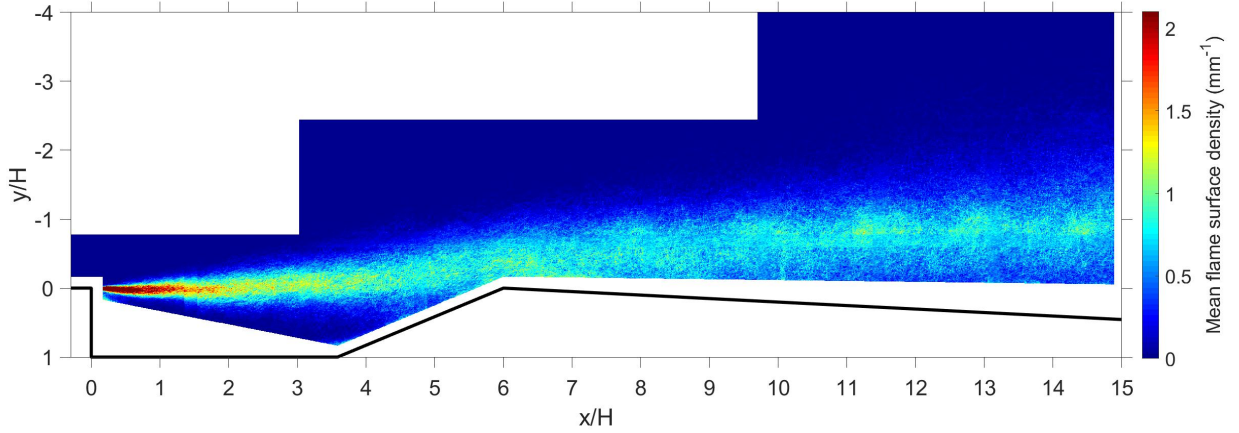
Figure 3.9: Mean local flame surface density (Σ) values.

factor of 1.3 to obtain correct three-dimensional values. It is unknown whether this factor would also be appropriate for a cavity flame; the factor is dependent on the anisotropy of the flame structure relative to the acquisition plane. Such an anisotropy exists in the Bell et al. results, and a different anisotropy may exist in the cavity flame. Therefore, no attempt is made here to correct the approximate two-dimensional Σ values. A DNS investigation of this cavity flame could quantify this anisotropy and provide an appropriate correction factor.

The map of Σ values was compared with the map of $\mathcal{I}$ values from Fig. 3.4. Lawn and Schefer [104] proposed that Σ should reach a maximum value at $\bar{c} = 0.5$ and suggested a relationship between Σ and $\bar{c}$ for turbulent premixed flames. The representation for this relationship shown in Eq. (3.8) substitutes intermittency $\mathcal{I}$ for mean progress variable $\bar{c}$.

$$\Sigma = 4\Sigma_{\max}\mathcal{I}\left(1 - \mathcal{I}\right) \tag{3.8}$$

For selected x'/H locations, Fig. 3.10 compares measured Σ profiles with estimated values

from Eq. (3.8). The profiles agree well with predictions for $x'/H \leq 4$; in these regions, the flame is above the cavity and the flame brush is able to propagate freely. For $x'/H \geq 6$, the profiles deviate from predictions, likely because the flame brush is constrained by the wall. The peak Σ value decreases significantly with downstream distance. Measurements on a turbulent premixed V-flame [105] and a Bunsen slot burner flame [103] observed a similar relationship; as flame brush thickness increases with downstream distance, maximum Σ decreases.
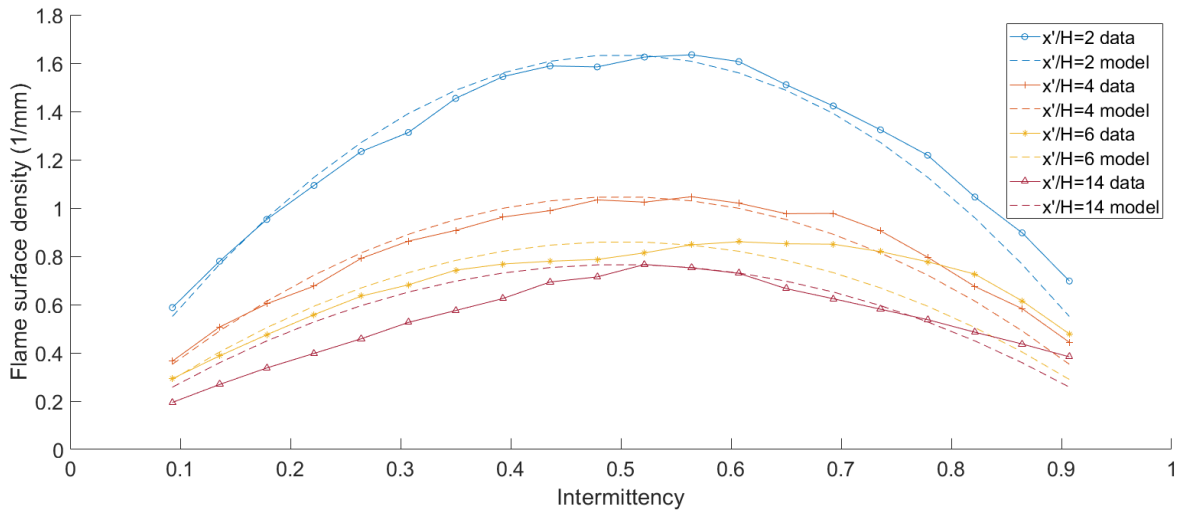
Figure 3.10: Comparison of experimental and theoretical flame surface density profiles.

3.4.2 Integrated flame surface density

The integral of flame surface density across the flame brush $\int \Sigma dy'$ is known as the integrated flame surface density. This quantity is equal to the ratio of the surface area of the turbulent flame A_T to the surface area of an equivalent laminar flame (i.e. a flat plane bisecting the flame brush) A_L. Integrated flame surface density is proportional to the ratio of the turbulent and unstretched laminar burning speeds, S_T/S_L [99]:

$$\frac{A_T}{A_L} = \int_{-\infty}^{\infty} \Sigma dy' \tag{3.9}$$

$$\frac{S_T}{S_L} = I_0 \frac{A_T}{A_L} \tag{3.10}$$

Here, I_0 is an unknown stretch factor. I_0 depends significantly on strain [106]. The flow in the current work is subject to acceleration (and therefore variable strain rate) due to the shear layer and flow interactions with the wall. As a result, variation in S_T/S_L cannot be discerned directly from OH-PLIF flame surface density results.

Integrated flame surface density was computed as a function of x' and plotted in Fig. 3.11. Integrated flame surface density is equal to unity at the cavity leading edge, where the flame approximates a laminar flame. It grows steadily with increasing x' as the brush widens, except for a decrease in the vicinity of the trailing edge of the cavity where the brush narrows slightly (see Fig. 3.6).

Hybrid LES/RANS simulations of the current flowpath [9] estimate the nondimensional turbulence intensity $u'/S_L \approx 7$ to 20 and the ratio of integral length scale to laminar flame thickness $\Lambda/\delta_L \approx 20$ to 70. These values place the flame in the thin reaction zone regime, in which $\text{Re}_\Lambda > 1$ and $1 < \text{Ka}_\eta < 100$ [14]. Gülder and Smallwood [107] investigated the effects of u'/S_L and Λ/δ_L on flame surface density using premixed propane-air Bunsen flames. For measurements in the thin reaction zone regime ($u'/S_L = 5.3$ to 15 and $\Lambda/\delta_L = 32$ to 48), they recorded integrated flame surface density values between 2.5 and 5, with no strong dependence on either parameter. In the current work, integrated flame surface density reaches a value near 3 at the downstream end of the domain.
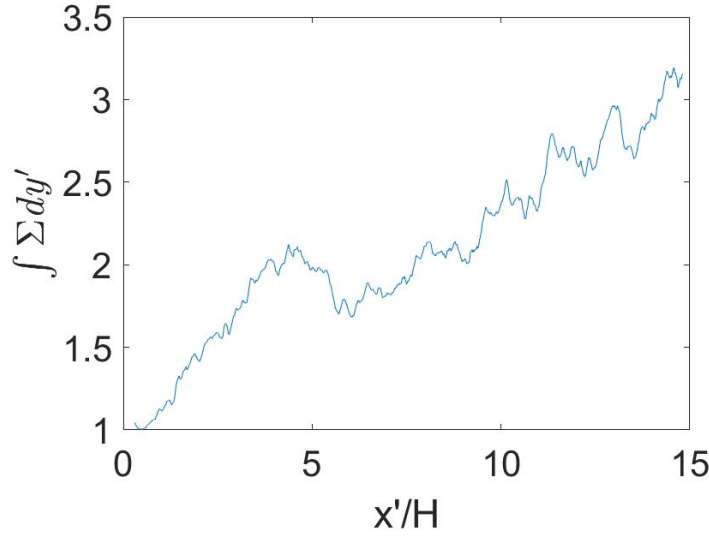
Figure 3.11: Integrated flame surface density as a function of x'/H.

3.5 Flame front curvature

3.5.1 Definition

Flame front curvature is another measure that can be used to quantify the extent to which the flame is wrinkled [94]. Curvature is the inverse of the radius of curvature ($\kappa = 1/r$) and can be calculated locally for any point on a flame front. A straight flame front section has a zero curvature value, and a curved section has a positive or negative value depending on the direction of concavity. The shape of the distribution of flame front curvature values is associated with turbulence characteristics. Wider curvature distributions are indicative of highly-wrinkled flames; they are associated with smaller Taylor and Kolmogorov length scales [108].

An algorithm, similar to one created by Bayley et al. [94], was developed to determine the curvature at each point along each flame front. For each OH-PLIF acquisition, a "flame front image" was generated in which pixels that lie on the flame front are isolated and given a value of 1, and all other pixels are set to 0. Some chains of pixels form loops. All other chains terminate at the image border or at the edge of the flame brush. Pathwise coordinates

are assigned to each pixel. It is important that each chain of pixels is processed in the same direction with respect to the burned area; this work uses the convention that the pathwise coordinate increases in the direction that keeps the burned area on the *right*. This convention produces positive curvature values when the flame front is concave towards products and negative curvature values when the flame front is concave towards reactants.

The following steps were implemented in a MATLAB script for each flame front image. First, all starting points and endpoints were identified. Based on the direction convention, the starting point was assigned the pathwise coordinate $s = 0$. For loops, an arbitrary starting point was assigned $s = 0$. This point was the "current location" for the script. The script checked for pixels adjacent to its current location that had not yet been processed. Then, s was incremented by 1 if the connection between pixels was horizontal or vertical, or s was incremented by $\sqrt{2}$ if the connection between pixels was diagonal. The current location was updated, and its x-, y-, and s-coordinates were recorded. This process was repeated until each pixel in each chain was processed. Chains of pixels in the flame front image occasionally included junctions. At a junction, the script was presented with multiple adjacent flame front pixels. For each option, the script checked if proceeding in that direction would be valid under the direction convention. If there were multiple valid options, then the script took the valid option that resulted in the leftmost turn. The resulting chains of connected pixels either formed loops, terminated at the image boundary, or terminated at the mask hiding the cavity wall.

For a given flame front pixel, the local curvature κ can be calculated from local first and second derivatives of x and y with respect to s. These local derivatives were calculated on the basis of a one-dimensional window of length w centered on the target pixel. No such window is possible for target pixels that were fewer than $w/2$ pixels from an endpoint and no curvature values were calculated at those points. Loops with a circumference smaller than w were disregarded entirely. For loops, the lists of x-, y-, and s-coordinates were padded to permit calculation of curvature at every pixel. Coordinates for the flame front pixels

within the window were used to fit cubic polynomial functions for $x(s)$ and $y(s)$, and these functions were used to obtain the local curvature value using Eq. (3.11) [109]. The curvature calculation process is illustrated in Fig. 3.12. Because the OH-PLIF images have in-plane resolution 40×40 μm, computed radii of curvature smaller than 40 μm were ignored; this is equivalent to rejecting all curvature values with a magnitude greater than 25 mm^{-1}.

$$\kappa = \frac{\frac{dy}{ds}\frac{d^2x}{ds^2} - \frac{dx}{ds}\frac{d^2y}{ds^2}}{\left[\left(\frac{dx}{ds}\right)^2 + \left(\frac{dy}{ds}\right)^2\right]^{\frac{3}{2}}} \tag{3.11}$$
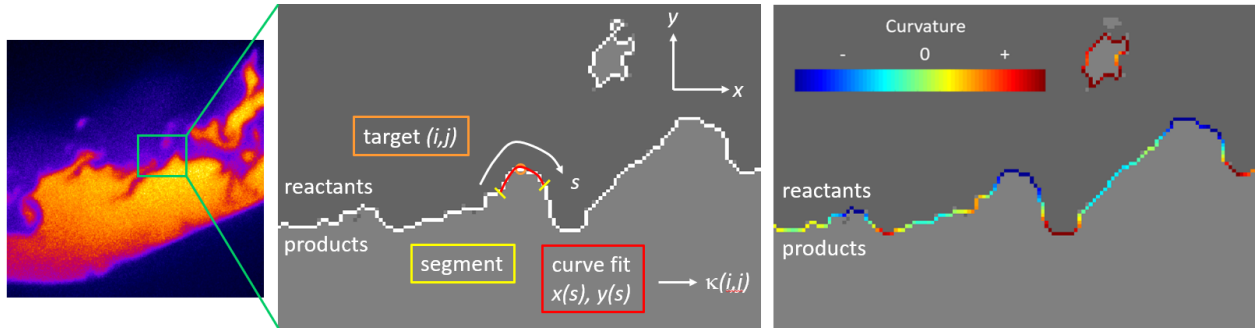
Figure 3.12: Curvature calculation for a flame front section.

3.5.2 Window length sensitivity

The appropriate choice of w is not immediately apparent. If w is too small, then high-magnitude curvature values will frequently appear as the result of noise. As w is increased, the contribution of noise is smoothed out and the variability of curvature decreases; however, the contribution of small flame front structures is also smoothed out. Therefore, a value of w must be chosen that effectively rejects contributions from noise while retaining contributions from small flow structures. The value of w was selected by sensitivity analysis of curvature distributions calculated using different values of w. Ni et al. [110] and Voth et al. [111] use a similar technique to choose a temporal filter length in order to calculate particle acceleration values. The curvature distribution of 1,900 images (100 from each field of view) was used for this analysis. Figure 3.13 shows the relationship between w and the variance of the resulting

distribution. When w is small (around 10 pixels), increases in window length cause an exponential drop in curvature variance as noise is smoothed out. When w is large (around 30 pixels), curvature variance decreases much more slowly with increasing w, as the contribution of flame front structures is smoothed out.

A function that describes the curvature variance as a function of w is the sum of an exponential term representing the contribution due to noise and a linear term representing the contribution due to structures, as shown in Fig. 3.13. A window length of 19 pixels was chosen; at this value, the contribution due to noise is largely rejected and the contribution due to structures is retained.
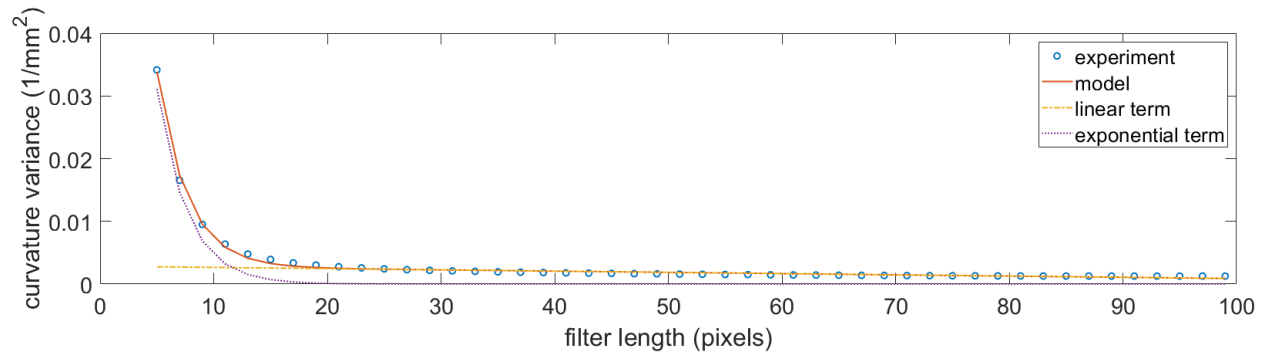
Figure 3.13: Variance of curvature versus filter length, w. A curve is fitted to the data, and its two constituent terms are also plotted.

3.5.3   Calculation

Figure 3.14 shows a subsection of a binarized OH-PLIF image in which the flame front has been colorized based on curvature values. Figure 3.15 shows probability density functions for curvature values in three different regions: the area of the constant-depth portion of the cavity from $x/H = 0$ to 4, the area of the cavity trailing edge from $x/H = 4$ to 8, and the downstream area from $x/H = 8$ to 15. These distributions are approximately Gaussian with means near zero. Table 3.2 lists parameters for these distributions. Uncertainty values for flame front curvature mean correspond to a 95% confidence interval.
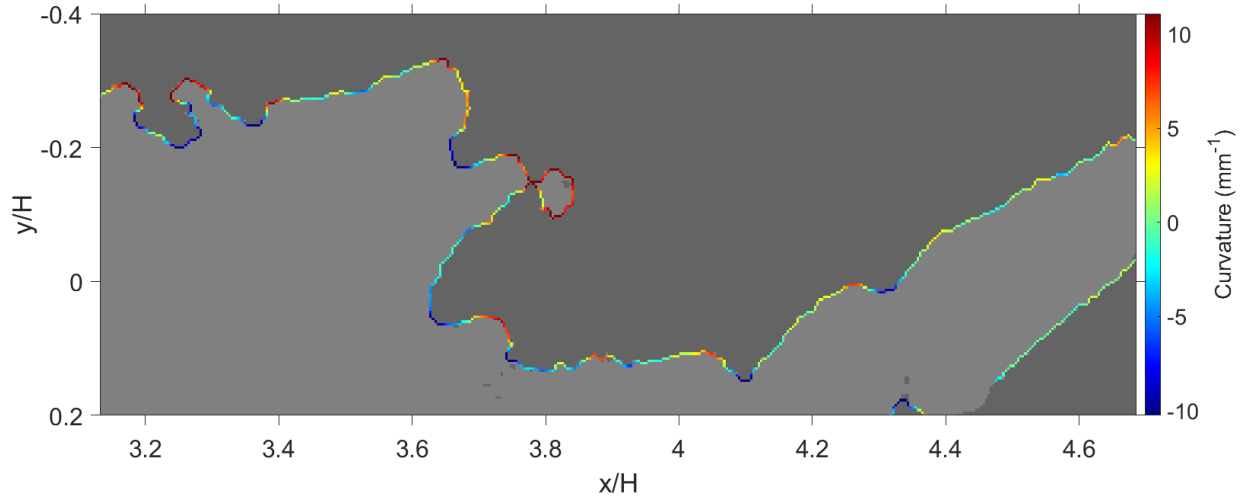
Figure 3.14: Curvature values along flame front. Product regions shown in light gray, reactant regions shown in dark gray.

Figure 3.15: Curvature probability density functions for three domain subsections.

Table 3.2: Curvature distribution parameters

Region	$0 < x/H < 4$	$4 < x/H < 8$	$x/H > 8$
mean (mm^{-1})	-0.256 ± 0.009	-0.042 ± 0.007	-0.104 ± 0.004
standard deviation (mm^{-1})	6.206 ± 0.006	5.923 ± 0.005	5.705 ± 0.003
skewness	-0.110	-0.265	-0.242

As with the flame surface density analysis, the two-dimensional curvature values given here attempt to approximate the true three-dimensional curvature of the flame structure. The relationship between two- and three-dimensional curvature values is unclear. Bell et al. [103] simulated a turbulent premixed Bunsen flame using DNS and compared two- and three-dimensional curvature values. The three-dimensional curvature distribution was

skewed slightly negative relative to the two-dimensional curvature distribution; otherwise, the distributions were similar. This is in contrast to a study by Ashurst and Shepherd [112] on a similar flame; they found the two-dimensional curvature distribution to be greater in magnitude than the three-dimensional distribution by a factor of 1.57. A DNS study of this cavity flame would enable a comparison between two- and three-dimensional curvature values.

Mean and standard deviation curvature values vary only slightly with downstream distance. The distribution of flame front length scales (and by analogy, turbulent length scales) seems to be largely unaffected by the spread of the flame into the main flow. This suggests that flame front length scales are imposed by freestream turbulence and are not significantly affected by combustion. This is consistent with recent combined OH-PLIF/PIV on the flowfield in the current work [77] which indicated that the scales of eddies in the flame above the cavity correlate directly with free stream eddies.

3.6 Large-cavity configuration results

Processing OH-PLIF results from the large cavity configuration dataset involved multiple challenges not present in the small cavity images. One of these challenges was the ablation of the copper combustor insert by the laser sheet. As mentioned previously, this completely prevented imaging in some near-wall locations. It also occasionally marred images in other locations, as shown in Fig. 3.16.

Because the size of the cavity and the flame brush were both larger relative to the size of the field of view, images in which only products or only reactants are visible were much more common. The strongest gradient in these images did not correspond to a flame front; it would often correspond to intensity changes due to noise or slow changes in OH concentration within the region of products. In some images, the highest gradient was associated with light scattered off ablated copper particles. Images that would be improperly binarized in this way had low variability in pixel intensity within an image, whereas images containing the flame
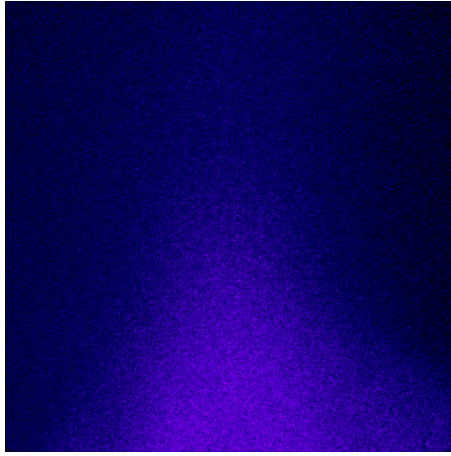
(a) Only ablation scatter visible.   (b) OH-PLIF and ablation scatter visible.
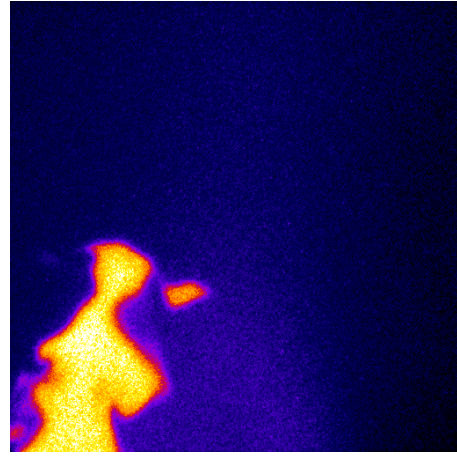
Figure 3.16: OH-PLIF images marred by ablation scatter.

front would have two separated pixel intensity modes. Therefore, images containing only products or only reactants could be identified through a test of pixel variability. Through trial-and error, a threshold of $2.5 \cdot 10^7$ was chosen as the minimum acceptable pixel intensity variance. Images with higher variances were binarized using the algorithm described in Section 3.2. Images with lower variances and with mean pixel intensities above 8,000 were binarized as consisting only of products; the positions of such images are shown in Fig. 3.17. The remaining low variance images were binarized as consisting only of reactants, as shown in Fig. 3.18.
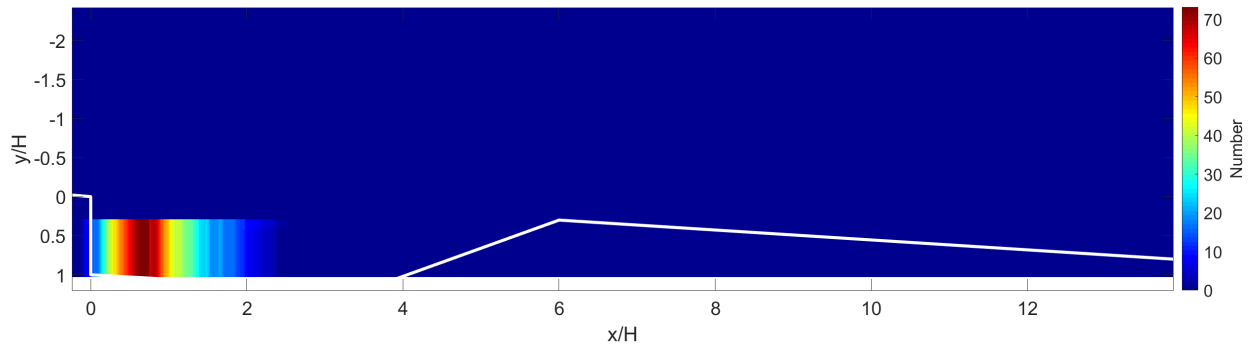
Figure 3.17: Number of acquisitions binarized as products only.
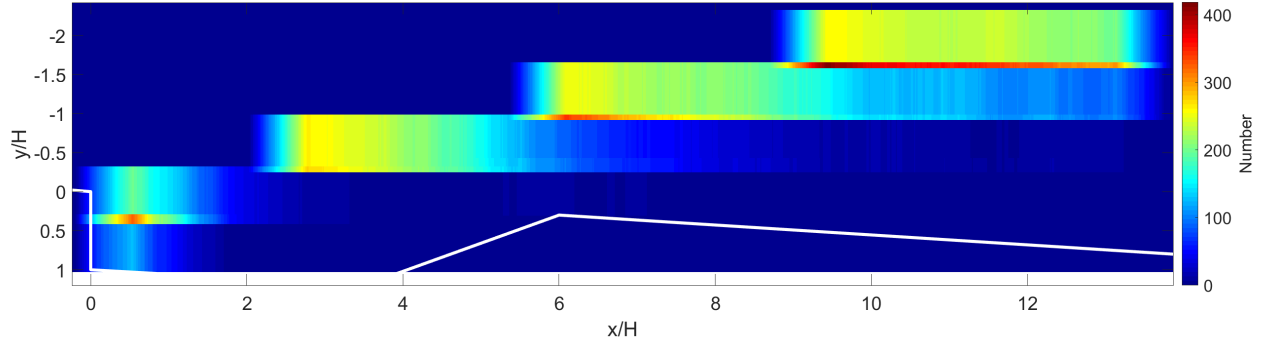
Figure 3.18: Number of acquisitions binarized as reactants only.

Intermittency values across the domain are shown in Fig. 3.19. The flame angle, as defined by the 5% intermittency contour, is about 10°, consistent with previous, lower-resolution OH-PLIF measurements [80]. Two significant differences can be noted between this intermittency distribution and that for the small cavity configuration (Fig. 3.4). First, there is no significant drop in intermittency at the cavity aft ramp (near $x/H \approx 6$), likely because flow acceleration values over the ramp and resulting local strain rate values are lower for the large cavity configuration. Second, there is a larger region of low intermittency near the cavity leading edge ($0 < x/H < 0.5$). This may indicate a difference in flow recirculation dynamics between the two cavities.
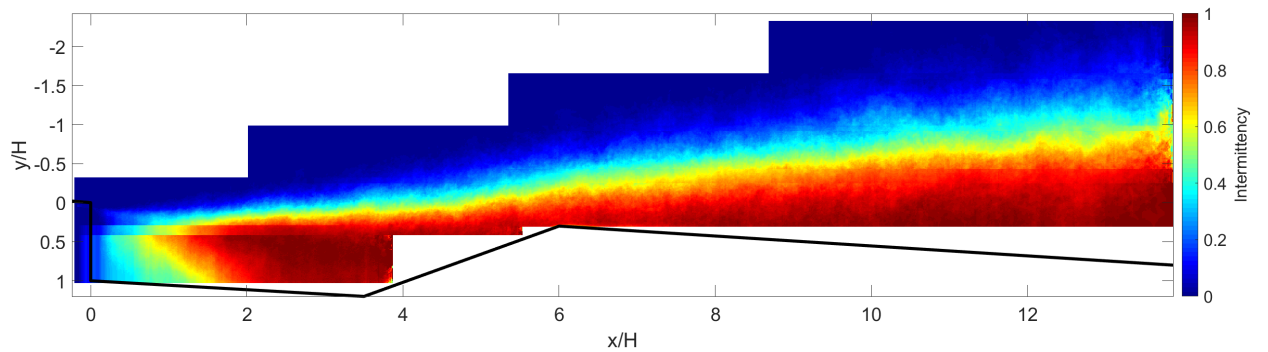
Figure 3.19: Intermittency values across the large cavity domain.

Curvature was calculated for all images in which a flame front was visible using the algorithm presented in Section 3.5. A window length of $w = 17$ pixels was used to match the

length in mm represented by the 19-pixel window used for processing small cavity images. Distributions of flame front curvature values for three subsections of the domain are shown in Fig. 3.20, and the parameters of these distributions are listed in Table 3.3. For $x/H > 4$, curvature distributions are very similar to those observed for the small cavity. For $x/H < 4$, the distribution is somewhat wider, indicating a more highly-wrinkled flame front in the vicinity of the cavity.
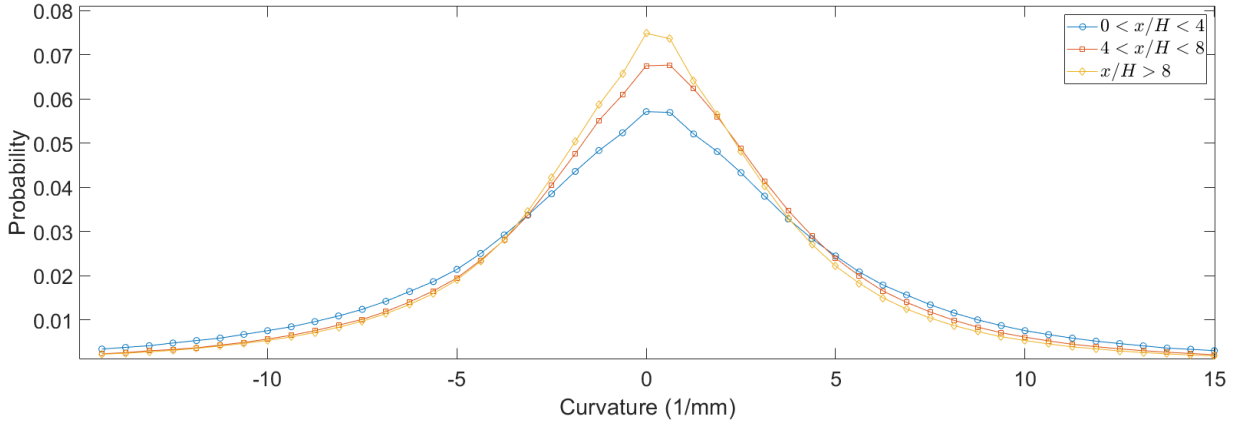
Figure 3.20: Large cavity curvature probability density functions for three domain subsections.

Table 3.3: Large cavity curvature distribution parameters

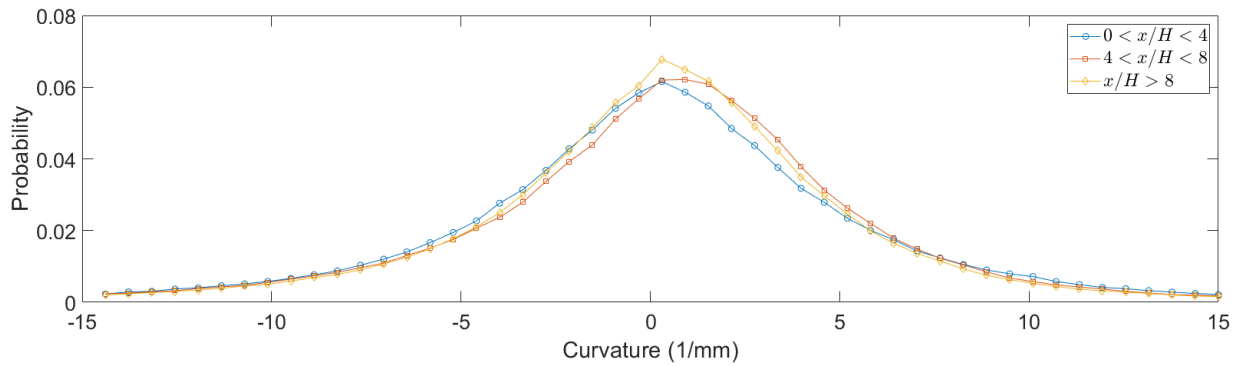| Region	$0 < x/H < 4$	$4 < x/H < 8$	$x/H > 8$
mean (mm^{-1})	-0.183 ± 0.010	-0.060 ± 0.006	-0.201 ± 0.004
standard deviation (mm^{-1})	6.825 ± 0.007	5.889 ± 0.004	5.666 ± 0.003
skewness	-0.032	-0.062	-0.086

3.7   Summary

This chapter has presented the extraction of metrics describing the shape of the flame anchored on cavity flame holders of two different sizes. An automated flame image analysis method was developed to binarize OH-PLIF images into burned and unburned regions; the interface between these regions was defined as the flame front. Measurements of flame surface density suggest that the flame exists in the thin reaction zone turbulent combustion regime.

Local curvature was computed at each pixel of the flame front. These metrics will be used in Chapter 4 to enable a direct comparison between the small cavity experimental results and computational DNS results.

Comparisons of intermittency, flame angle, and flame front curvature indicate that the flame structure is substantially similar between the two cases. The most significant difference between the results of the two experiments occurs at the aft ramp of the cavity, where in the small cavity configuration, high local strain rates are believed to reduce combustion reaction rates, decreasing the intermittency of products. Downstream of the ramp, in the diverging extender section, the OH-PLIF intensity and the flame intermittency were seen to recover and support strong combustion. No such intermittency reduction is seen in the large cavity results.

Chapter 4

Analysis of cavity-stabilized flame simulation results

4.1   Motivation and objectives

The reduced scale of the small-cavity configuration at UVaSCF provides a reduced volume of interest in the area where the flame anchors. This makes it feasible for the first time to perform 3D direct numerical simulation (DNS) for a cavity flame holder, resolving the structure of the turbulent flame at all length and time scales. High-spatial-resolution outputs from DNS can be processed using the tools presented in Chapter 3 to gather metrics describing the flame structure. This enables validation of DNS through a direct comparison with experimental PLIF images. DNS results can also be used to verify whether the experimental PLIF images resolve all flame structure spatial scales.

This chapter is structured as follows. First, the process of simulating OH-PLIF images from DNS outputs is described, followed by the process of extracting flame front metrics from the images. The flame structure of DNS is discussed with reference to the PLIF experiment, with recommendations for future experimental and computational improvements. Finally, a brief comparison is made between PLIF results and two other computational outputs (hybrid

Table 4.1: DNS boundary conditions, from [42].

M	u' [m/s]	p [atm]	T [K]	ϕ
0.3	38.8	1.72	1125	0.42

LES/RANS and discontinuous Galerkin) that do not replicate the fine flame structure seen in PLIF images.

4.2 Direct numerical simulation

The DNS calculation itself is not a focus of this dissertation and is thoroughly described elsewhere [43, 42]; therefore, it will only be summarized here. The DNS solver adopted is the S3D code developed at at Sandia National Laboratories [113] and has been used to simulate a cavity flame holder in conditions similar to the reduced-scale cavity configuration at UVaSCF. S3D solves the full compressible, reacting Navier-Stokes equations coupled with detailed or reduced chemistry. S3D uses an eighth-order explicit central scheme [114] along with tenth-order explicit filtering to prevent spurious oscillations. Time integration is performed with a six-stage fourth-order explicit Runge-Kutta method, and Navier-Stokes characteristic boundary conditions are applied. A multi-block version of S3D was used to simulate a duct of height 14.6 mm and width (in the spanwise direction) 10 mm. Adjoining the duct is a ramp cavity with cross-sectional dimensions equal to those of the cavity used in experiments. The simulation was performed with a uniform grid with grid size equal to 23 μm.

The simulation inflow Mach number was set at 0.3 (in contrast to the experimental value of 0.6) in order to limit the computational cost. Inflow pressure, temperature, and equivalence ratio, as well as wall temperatures, were set based on LES simulations of the same flowpath [9]. Wall temperatures were set as follows: 800 K for $x/H \leq 0$, 1000 K for $0 < x/H < 3.5$, and 1100 K for $x/H > 3.5$. Inflow turbulence intensity was set based on PIV experiments [83]. The spanwise dimension of the domain was subject to periodic boundary conditions. Inlet boundary conditions for the simulation are shown in Table 4.1.

OH mole fraction values for a selected z-position and timestep are shown in Fig. 4.1, and heat release values are shown in Fig. 4.2.
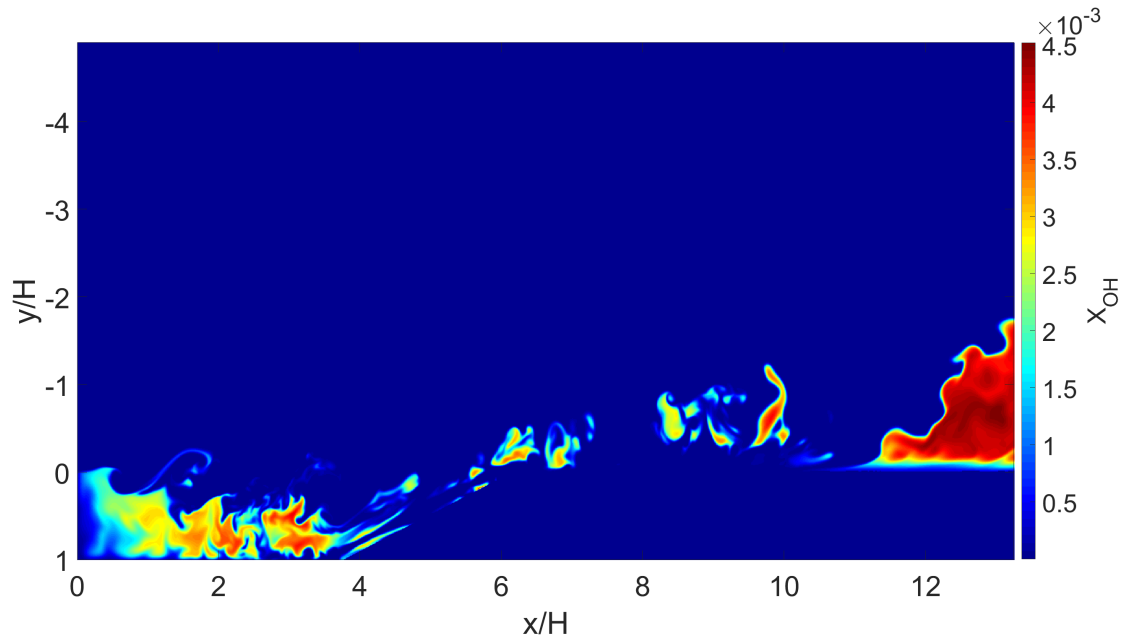
Figure 4.1: Instantaneous DNS OH mole fraction values.
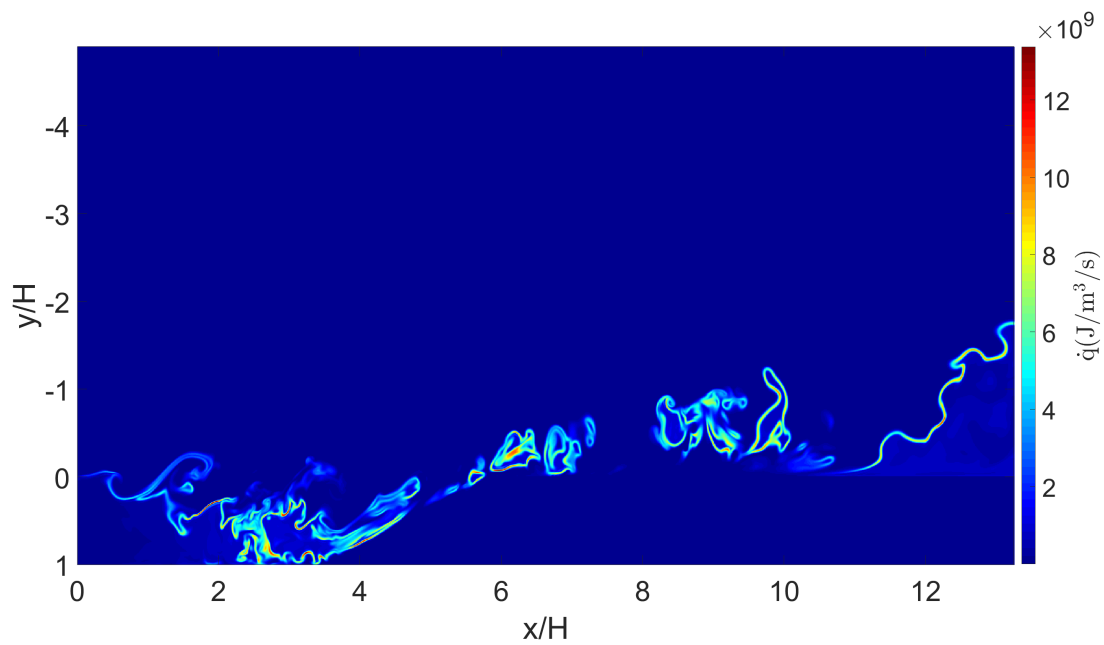
Figure 4.2: Instantaneous DNS heat release values.

4.3 Simulated PLIF

The PLIF measurements presented in Chapters 2 and 3 are not quantitative; that is, they do not provide values for OH concentration. Moreover, PLIF signal values are not directly proportional to OH concentration and should not be used for a one-to-one comparison with OH concentration values from DNS results. In order to make the most accurate comparison between experimental and computational results, simulated PLIF images can be created from DNS results [115]. First, parameters from the LIF excitation process (laser line overlap, laser sheet irradiance, etc.) are taken into account to determine the dependence of the PLIF signal on temperature and pressure. Then, the z-profile of the laser sheet is used to integrate DNS outputs in the z-direction and explore the dependence of PLIF results on laser sheet thickness. The result is a two-dimensional map of simulated PLIF signal with arbitrary units that can be compared directly with experimental PLIF images. The simulated images can also be processed to produce the flame shape metrics discussed in Chapter 3 to enable morphological comparison with experimental results.

4.3.1 Temperature and pressure effects

LIF is typically modeled as a two-level and two-step process [25]. A target species has a population at a ground state, state 1. Molecules absorb laser light and move to an excited electronic state, state 2. The absorption process has a rate coefficient W_{12}. After a period of time on the order of nanoseconds, spontaneous emission (rate coefficient A_{21}) causes molecules to fall back to the ground state. State number densities N_1 and N_2 are also primarily affected by stimulated emission (rate coefficient W_{21}) and collisional quenching (rate coefficient Q_{21}). Based on only these processes, the rate equations for the two states are given by:

$$\frac{dN_2}{dt} = N_1 W_{12} - N_2 \left(W_{21} + A_{21} + Q_{21} \right) = -\frac{dN_1}{dt} \tag{4.1}$$

This model assumes dissociation and photoionization are both negligible. As was shown in Chapter 2, PLIF measurements reported in this work are strongly saturated, with $W_{12} \gg W_{21} + A_{21} + Q_{21}$. Neglecting the smaller rate constants and integrating over the duration of the laser pulse:

$$\int_{N_2(t=0)}^{N_2(t=\infty)} dN_2 = \int_0^\infty N_1 W_{12} dt \tag{4.2}$$

The excitation rate can be represented [88]:

$$W_{12}(t) = I(t) B_{12} \hat{g} / c \tag{4.3}$$

Here, $I(t)$ is the irradiance of the laser pulse, B_{12} is the Einstein-B coefficient for the transition, c is the speed of light, and $\hat{g}$ is the laser overlap integral describing spectral overlap between the laser pulse and the molecular transition. Substituting this representation into Eq. 4.2:

$$\int_{N_2(t=0)}^{N_2(t=\infty)} dN_2 = \frac{N_1 B_{12} \hat{g}}{c} \int_0^\infty I(t) dt \tag{4.4}$$

Integrating with the initial conditions of $I(t=0) = 0$ and $N_2(t=0) = 0$:

$$N_2 = \frac{f_{B,1} N B_{12} \hat{g} E}{c A_c} \tag{4.5}$$

Here, E/A_c is the pulse energy divided by the cross-sectional area of LIF generation - the laser fluence. N_1 has been replaced by $f_B N$, the product of the Boltzmann fraction for the lower state and the total number density of the target species. The LIF signal intensity S_{LIF} is directly proportional to the excited state population N_2 [25]. Therefore, the LIF signal intensity is directly proportional to $\hat{g}$, f_B, and N_2 (which is in turn proportional to the local mole fraction X_{OH}). At each point in the domain, a qualitative LIF signal value S_{LIF} can be calculated in arbitrary units by:
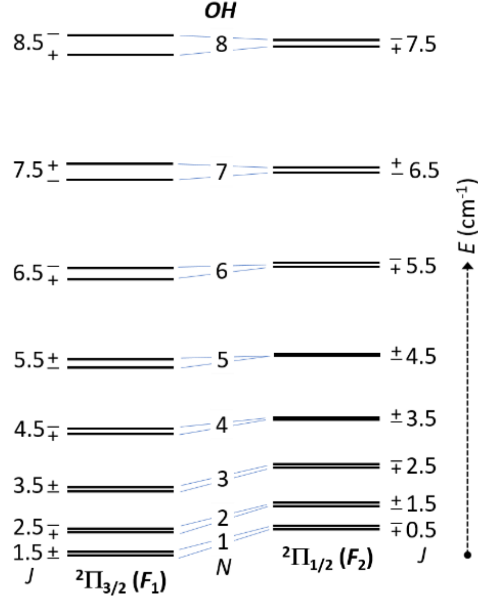
Figure 4.3: OH ground state rotational levels, from Carter and Lee [116].

$$S_{\text{LIF}} = X_{\text{OH}}\hat{g}f_B \tag{4.6}$$

In order to calculate S_{LIF} over the DNS domain, local values of f_B must be calculated. The variation of the Boltzmann fraction with temperature can be modeled using a process described by Carter and Lee [116], which is summarized here. For the OH-PLIF presented here, the lower state is the ground vibrational state $X^2\Pi\,(v'' = 0)$; the structure of the rotational levels of this state are illustrated in Fig. 4.3. These levels are spin-split into the $^2\Pi_{3/2}$ state and the $^2\Pi_{1/2}$ state. The $^2\Pi_{3/2}$ state is associated with a series of rotational states, denoted F_1, which have $J = N + 0.5$. The $^2\Pi_{1/2}$ state is associated with the F_2 series, which have $J = N - 0.5$. These states are further split by Λ-doubling. The split states are given parity symmetry labels "$-$" or "$+$" in Fig. 4.3. However, in the calculation of Boltzmann fractions, it is easier to treat them in two categories: "e" for the state with the lower energy of each Λ-doubled pair, and "f" for the state with the higher energy.

Rotational term energies $F_{ij}(J)$ for spin-split state i and Λ-doubled state j and vibrational term energies $G(v)$ are tabulated by Bernath and Colin [117]; these can be found in Appendix

B.1. They can be used to calculate vibrational and rotational partition functions:

$$Q_{\text{vib}}^{p}(T) = \sum_{v=0}^{6} \exp\left(\frac{-hcG_v}{k_BT}\right) \tag{4.7}$$

$$Q_{\text{rot}}^{p}(T) = \sum_{J=1.5}^{30.5} \left\{(2J+1)\left[\exp\left(\frac{-hcF_{1e}(J)}{k_BT}\right) + \exp\left(\frac{-hcF_{1f}(J)}{k_BT}\right)\right]\right\}$$
$$+ \sum_{J=0.5}^{30.5} \left\{(2J+1)\left[\exp\left(\frac{-hcF_{2e}(J)}{k_BT}\right) + \exp\left(\frac{-hcF_{2f}(J)}{k_BT}\right)\right]\right\} \tag{4.8}$$

The partition functions and term energies can then be used to calculate the Boltzmann fraction for a specific spin-split state i and Λ-doubled state j:

$$f_B(J, i, j, T) = \frac{(2J+1)\exp\left(\dfrac{-hcF_{ij}(J, v)}{k_BT}\right)}{Q_{\text{vib}}^{p}(T)Q_{\text{rot}}^{p}(T)} \tag{4.9}$$

The lower state for the $Q_{(N=8)}$ transition comprises the Λ-split states for both F_1, $J = 8.5$ and F_2, $J = 7.5$. Therefore, the relevant Boltzmann fraction for the OH-PLIF transition is the sum of terms from four states of very similar energy:

$$f_B(N=8, T) = f_B(J=8.5, i=1, j=e, T) + f_B(J=8.5, i=1, j=f, T)$$
$$+ f_B(J=7.5, i=2, j=e, T) + f_B(J=7.5, i=2, j=f, T) \tag{4.10}$$

The variation of Boltzmann fraction for the lower level of the PLIF transition is shown in Fig. 4.4. Local values of f_B for a selected DNS timestep and z-position are shown in 4.5.

At any given location in the flow, the LIF signal produced is also a function of the Doppler broadening linewidth $\Delta\nu_D$ (see Eq. 2.15), which varies with temperature, and the collisional broadening linewidth $\Delta\nu_C$ (see Eq. 2.14), which is a function of temperature, pressure, and the mole fractions of major collisional partners H_2O, CO_2, N_2, and O_2. The dependence of
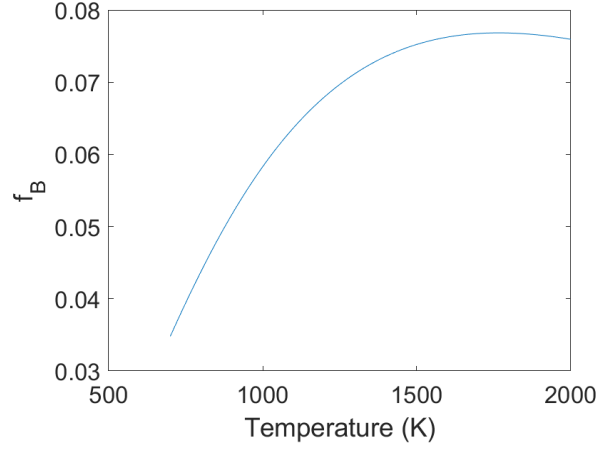
Figure 4.4: Temperature dependence of Boltzmann fraction for OH $X^2\Pi\left(v''=0\right)$
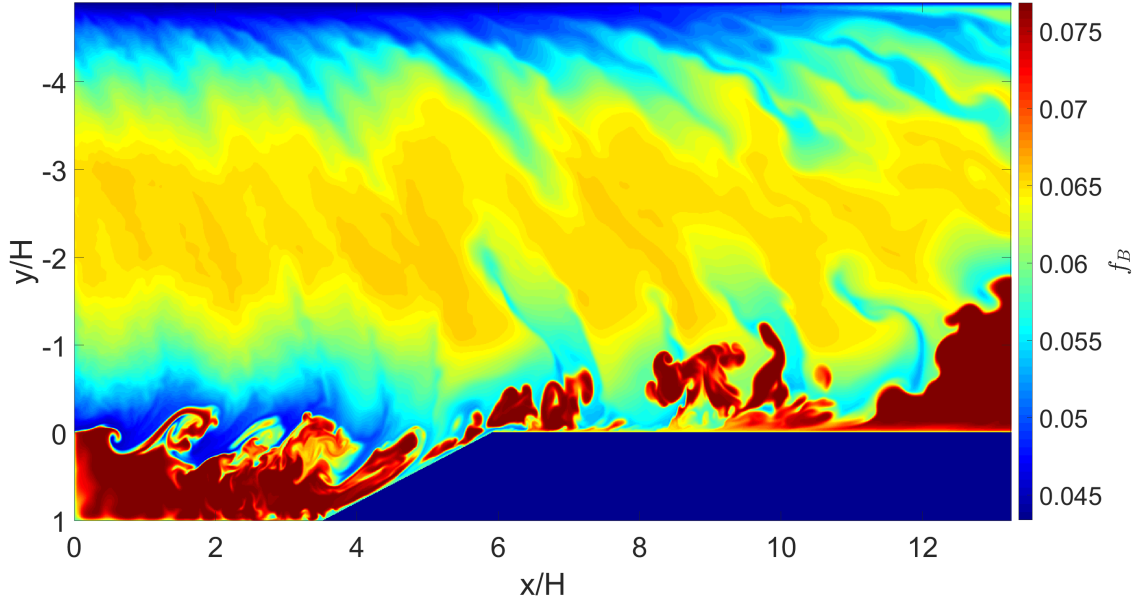
Figure 4.5: Boltzmann fraction values

$\Delta\nu_C$ on other species such as C_2H_4 is unknown and cannot be considered in this analysis. These terms contribute to the calculation of the laser overlap integral $\hat{g}$, whose calculation was described by Eqs. 2.10–2.13, 2.11. Figs. 4.6–4.8 display values for $\Delta\nu_D$, $\Delta\nu_C$, and $\hat{g}$, calculated for a single DNS timestep and z-position.

Finally, with local values of f_B and $\hat{g}$ known, simulated LIF images can be computed by applying Eq. (4.6) at each grid point. Simulated LIF images generated this way do not differ
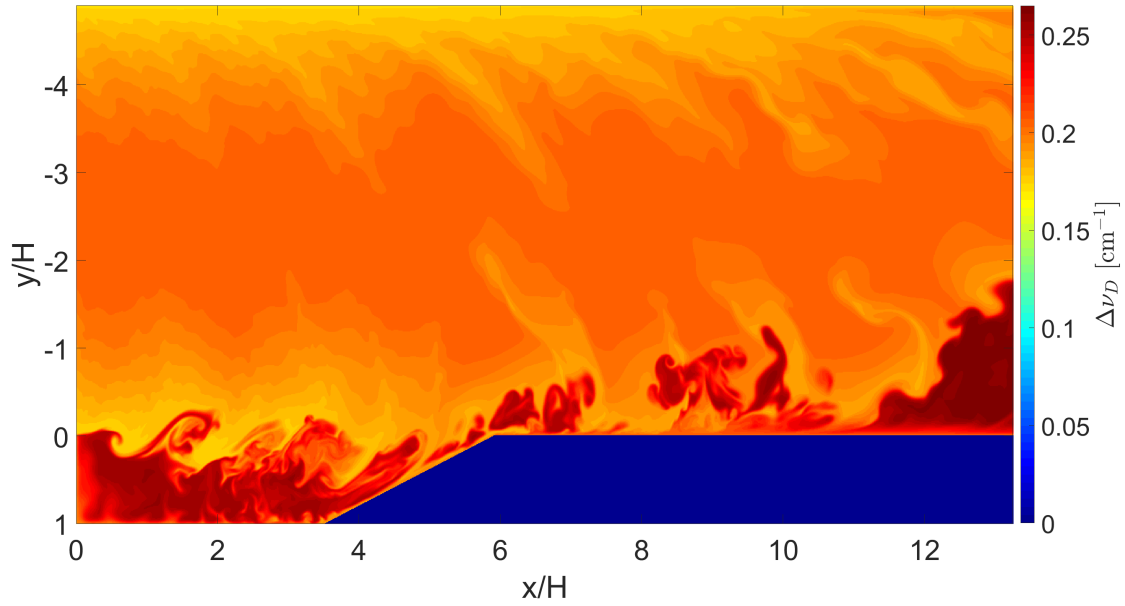
Figure 4.6: Doppler broadening linewidth values
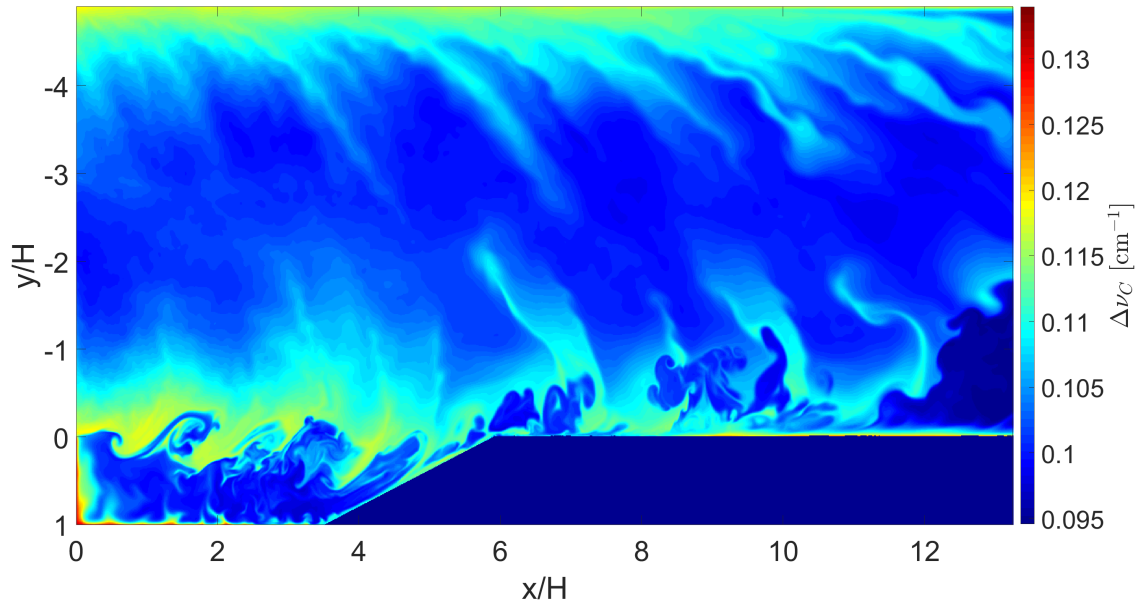
Figure 4.7: Collisional broadening linewidth values

significantly from images of X_{OH}. Fig. 4.9 shows the difference between one S_{LIF} image and its corresponding X_{OH} image, normalized by the maximum X_{OH} value. The largest differences are about 5% of the maximum X_{OH} value, and occur in the interior of pockets of combustion
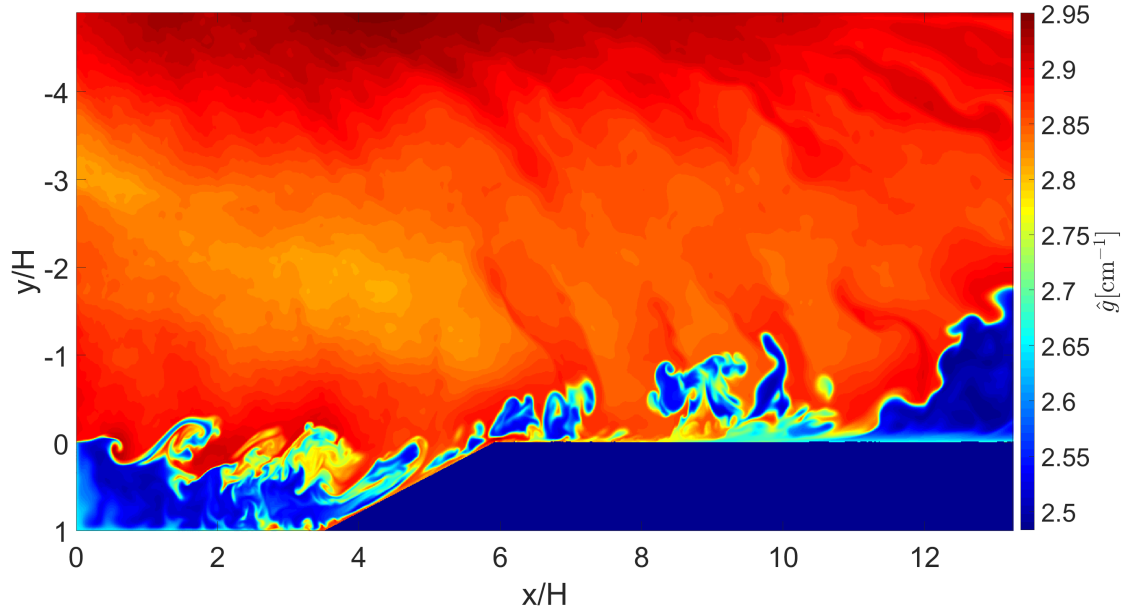
Figure 4.8: Laser overlap integral values

products on the downstream end of the domain. This is attributable to the temperature insensitivity of the selected transition and the low magnitude of pressure variations across the domain.

Importantly, the flame structure is not altered at all between the two images; binarization following the methods of Chapter 3 was performed on X_{OH} and S_{LIF} images, producing nearly identical results. Differences between binarized X_{OH} and Y_{OH} (mass fraction) images are negligible as well. Therefore, it is sufficient to compare experimental PLIF images directly to Y_{OH} for all flame front-based comparisons. This avoids the significant computational expense of X_{OH} and S_{LIF} calculation.
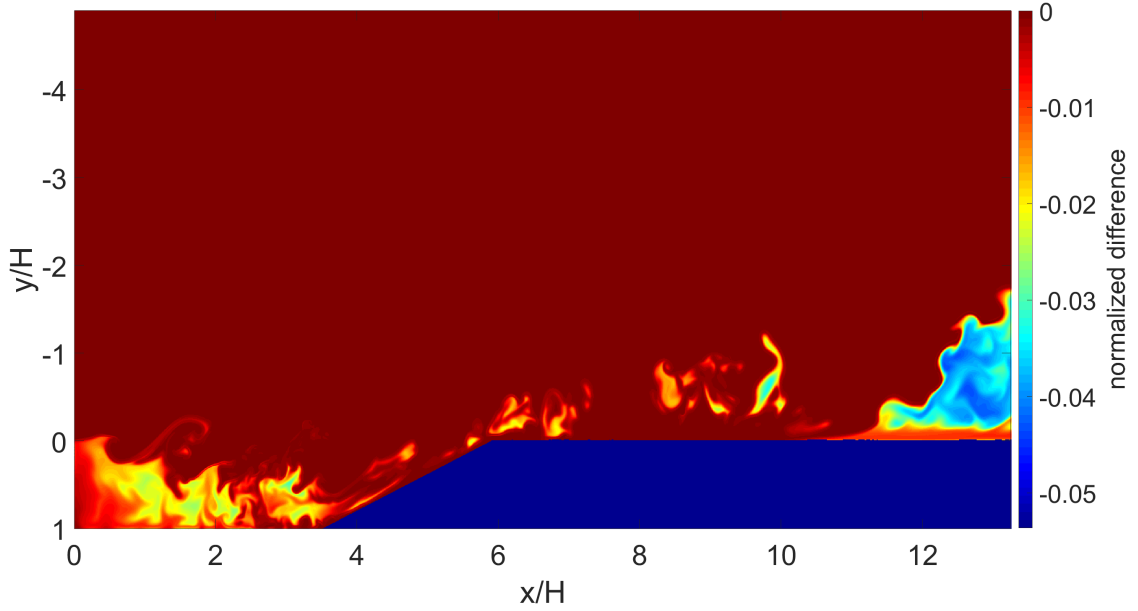
Figure 4.9: $\left(S_{\text{LIF}} - X_{\text{OH}}\right)/\max\left(X_{\text{OH}}\right)$

4.3.2 Laser sheet thickness effects

The z-direction thickness of the laser sheet from experimental images must also be considered when processing DNS results for comparison. Small-cavity PLIF results were acquired using a laser sheet with an approximately-Gaussian intensity profile with a full-width at half-maximum of about 95 μm. If flame structures normal to laser propagation exist that are much smaller than this value, then integration of the signal over the laser sheet could blur the boundaries of these structures.

DNS values for Y_{OH} were extracted in 3D grids spanning the entire domain in x- and y-directions, with 10 grid points in the z-direction, spanning 230 μm. Three simulated PLIF images were generated from each grid:

1. Y_{OH} values from a single, central z-position. This approximates the PLIF image that would be acquired for an infinitely-thin light sheet. This will be denoted $Y_{\text{OH, thin}}$.

2. Y_{OH} values averaged over the z-direction of the grid. This approximates the PLIF image that would be acquired using a 230 μm-wide sheet with a top-hat profile. This
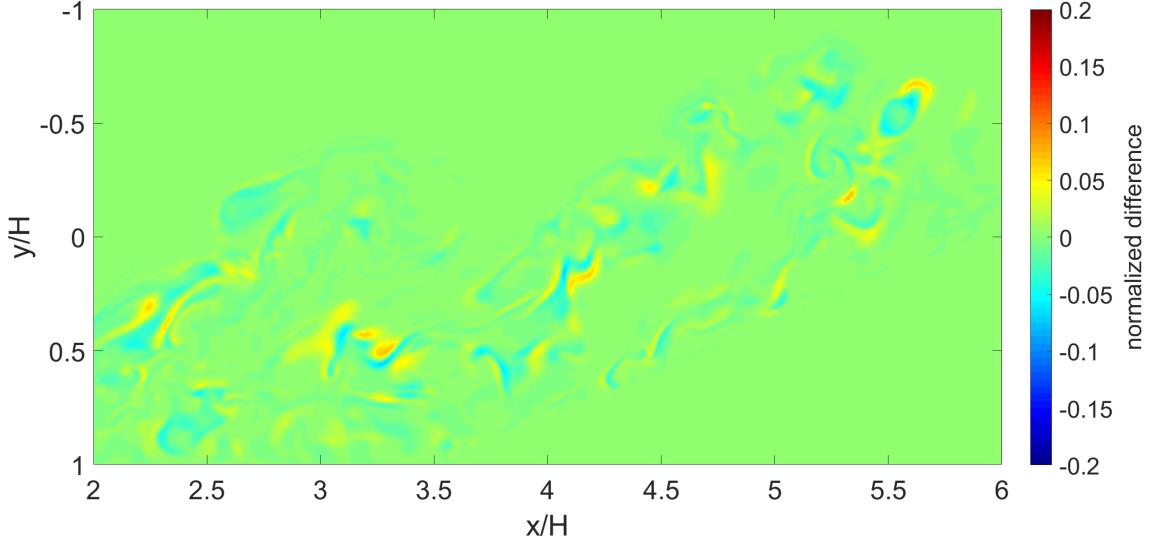
Figure 4.10: $(Y_{\text{OH, Gaussian}} - Y_{\text{OH, thin}}) / \max(Y_{\text{OH, thin}})$

represents a "worst-case scenario" – a sheet much wider than that in the current PLIF work. This will be denoted $Y_{\text{OH, top-hat}}$.

3. $f(z) \cdot Y_{\text{OH}}$ integrated over the z-direction of the grid, where $f(z)$ is a Gaussian function of full-width at half-maximum of 95 μm, centered on the z-position from image #1. This is an attempt to simulate the PLIF images acquired in the current experimental configuration. This will be denoted $Y_{\text{OH, Gaussian}}$.

For a section of one instantaneous DNS output, the normalized difference between the image produced with the infinitely-thin sheet profile that produced with the Gaussian profile is shown in Fig. 4.10. The two images differ by about $\pm 7\%$ of the maximum $Y_{\text{OH, thin}}$ value. The same comparison is made using the top-hat profile in Fig. 4.11; the difference grows to around $\pm 18\%$ of the maximum $Y_{\text{OH, thin}}$ value.

Normalized differences between PLIF signal and pure OH concentration due to temperature and pressure effects were explored in the previous section and were of approximately the same magnitude. Those differences impacted the interior of flame structures and left image flame front positions undisturbed. In contrast, the differences between simulated PLIF images
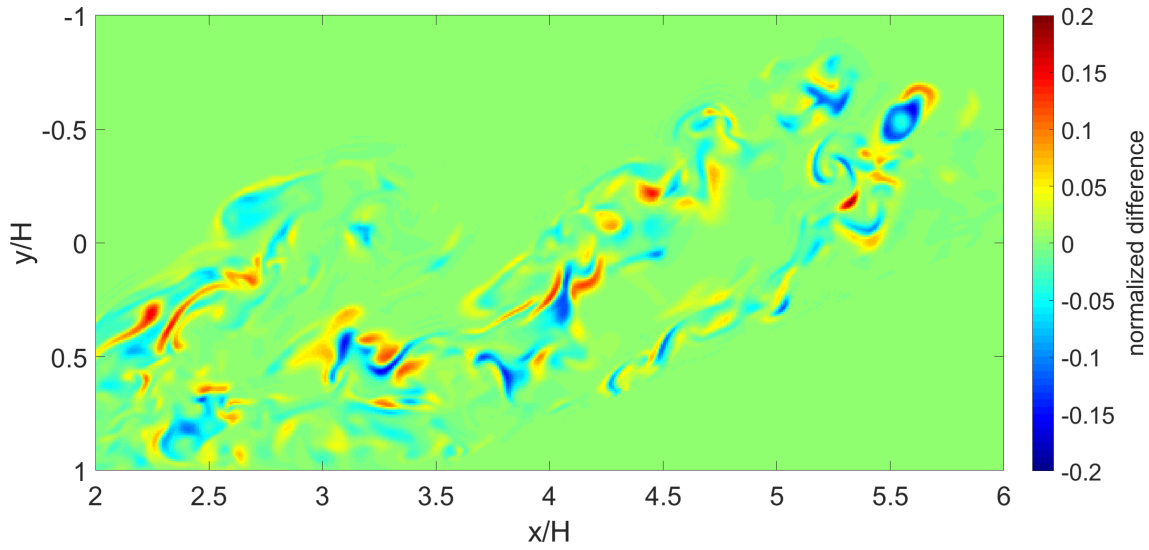
Figure 4.11: $\left(Y_{\text{OH, top-hat}} - Y_{\text{OH, thin}}\right)/\max\left(Y_{\text{OH, thin}}\right)$

obtained with different light sheets occur mostly at the edges of flame structures, altering the observed flame front position. Using the previously-described binarization methods, flame front locations were extracted from all three images. These are overlaid on $Y_{\text{OH, thin}}$ in Fig. 4.12. In many positions, the three flame fronts are co-located. In others, they deviate significantly. In general, as the sheet widens, the portion of the image binarized as products expands as new flame structures are integrated into the image. In some locations, contiguous areas of products that are separate from one another in the $Y_{\text{OH, thin}}$ image become connected as the sheet widens (see $x/H \approx 3$, $y/H \approx 0.5$). This illustrates a potential pitfall in the interpretation of PLIF images; while isolated pockets of combustion products in PLIF images may appear to indicate the presence of broken reaction zones, these pockets may actually be connected outside the plane of the image.
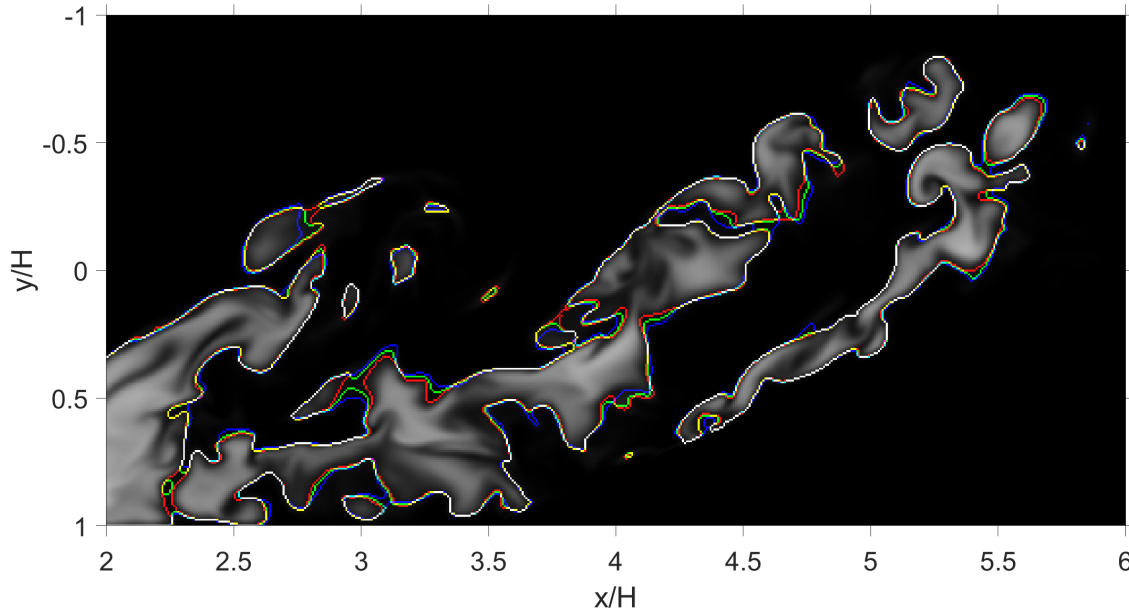
Figure 4.12: Instantaneous $Y_{\text{OH, thin}}$ in grayscale, extracted flame fronts overlaid. Red: flame front based on $Y_{\text{OH, thin}}$. Blue: flame front based on $Y_{\text{OH, Gaussian}}$. Green: flame front based on $Y_{\text{OH, top-hat}}$.

4.4   DNS flame front processing

4.4.1   Image processing algorithm validation

The flame front identified by the binarization algorithm is overlaid on a $Y_{\text{OH, thin}}$ image in Fig. 4.13, and on an image of heat release values in Fig. 4.14. The flame front position agrees very well with the positions of thin heat release regions, with some bias towards the outside of those regions. Some regions (such as $x/H \approx 2.5$, $y/H \approx 0.6$) are characterized by diffuse regions of heat release and relatively-weak OH gradients; here, the bias of the flame front position towards the outside of the heat release regions is more pronounced. In general, the flame front algorithm accurately reproduces the shape of the flame structures present in the DNS outputs.
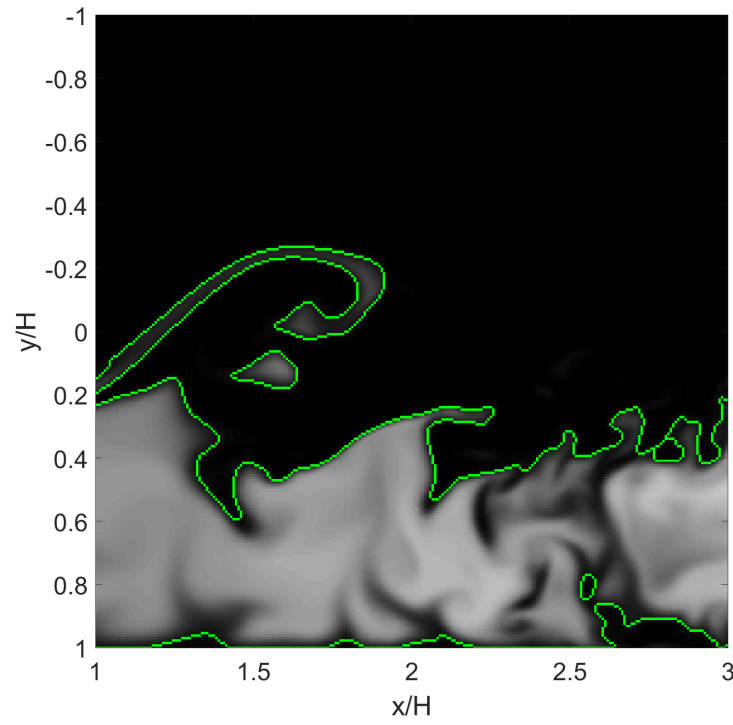
Figure 4.13: $Y_{\text{OH, thin}}$ in grayscale, extracted flame front overlaid in green.
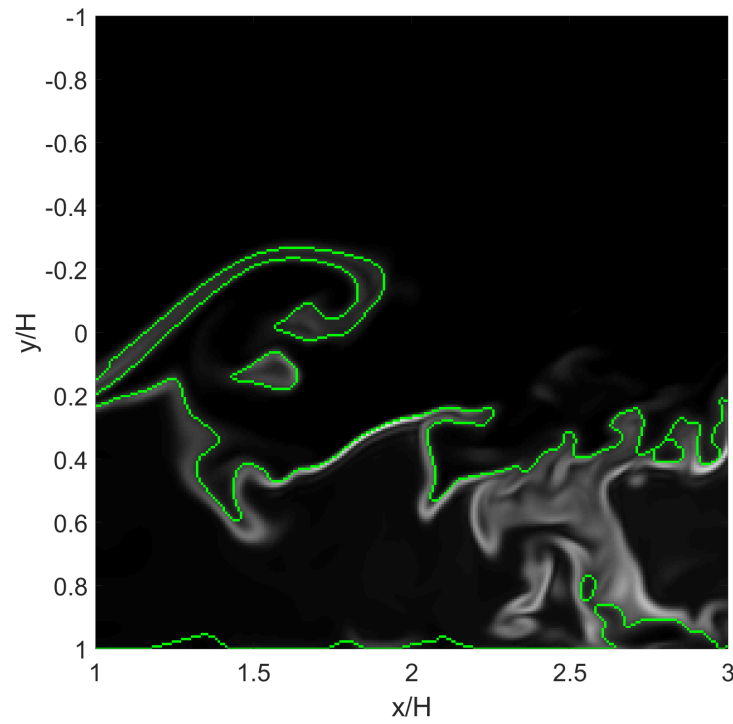
Figure 4.14: Heat release (from Fig. 4.2) in grayscale, extracted flame front overlaid in green.

4.4.2   Flame front metrics

3D grids of Y_{OH} outputs were used to generate simulated PLIF images using each of the three z-integration methods. 336 such grids were processed; these were extracted from 7 z-locations, spaced 700 μm from each other, and 48 different values of simulation time, spaced 18 μs from each other. Unfortunately, the images are not uncorrelated with respect to time or z-location. Uncorrelated images would provide a better comparison with experimental PLIF acquisitions but would be very computationally-expensive to produce.

$Y_{OH, \text{Gaussian}}$ images were used to produce a plot of intermittency, shown in Fig. 4.15. Comparison with experimental intermittency (Fig. 3.4), provides some insight into the relative behavior of the simulation and the experiment. The flame angle (based on the 5% intermittency contour) from the DNS output is 8.2°, agreeing very well with the experimental value of 8.75°, and indicating a similar value of s_T/u between DNS and experiment [14, 9].

A decrease in intermittency within the flame brush is noted near the aft ramp, followed by a subsequent increase further downstream; a similar effect was noted in the experimental results and attributed to high local strain rates as flow accelerates around the ramp. This effect is significantly more pronounced in the simulation than in the experiment. As in the experiment, DNS intermittency shows a kernel of constant OH presence near the cavity leading edge serving as a source of radicals sustaining combustion. Unlike the experiment, there is no region of reduced intermittency in the interior of the cavity near $x/H \approx 0$, $y/H \approx 1$. For the experimental images, this region was theorized to host a recirculation region where products became trapped for long residence times during which OH radicals would recombine. Its absence in the DNS images suggests that this recombination is not occurring. It is possible that the wall temperature boundary condition for the simulation is set too high and that lower wall temperatures in the experiment enable this recombination.

$Y_{OH, \text{Gaussian}}$ images were binarized and flame front curvature values were calculated based on the methods of Chapter 3. Curvature calculation was performed using a window of length $w = 9$ pixels, corresponding to the same approximate length in real space (~ 200μm)
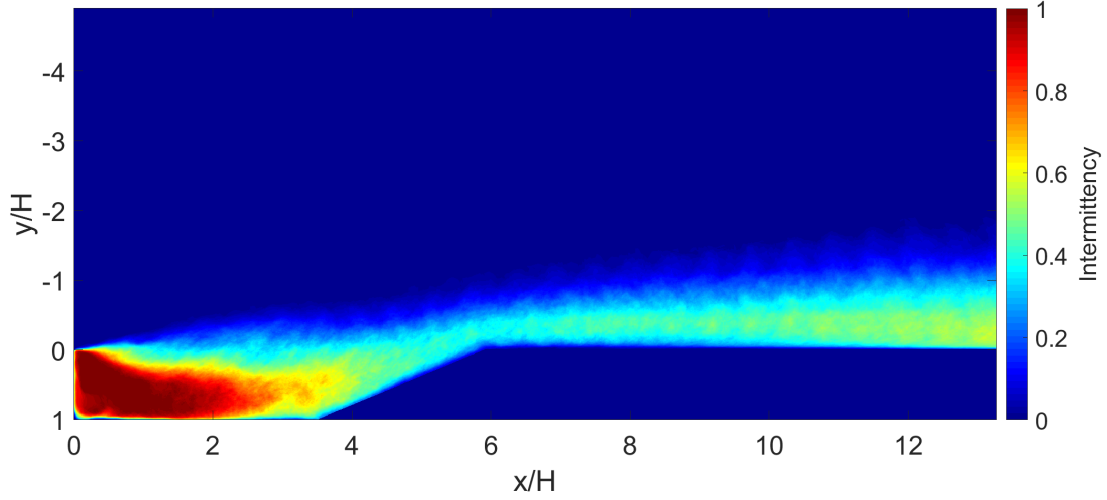
Figure 4.15: DNS intermittency, PLIF simulated using Gaussian sheet.

as the window used to process the small cavity OH-PLIF experimental data. Curvature values for a section of one instantaneous flame front are displayed in Fig. 4.16. Curvature distributions for three different domain regions are displayed in Fig. 4.17, and parameters for these distributions are listed in Table 4.2. Relative to $Y_{\text{OH, Gaussian}}$ results, $Y_{\text{OH, thin}}$ images had curvature standard deviation values that were greater by 0.04–0.1 mm^{-1}. $Y_{\text{OH, top-hat}}$ curvature standard deviation values were smaller by 0.05–0.07 mm^{-1}.

Table 4.2: DNS curvature distribution parameters, PLIF simulated using Gaussian laser sheet.

Region	$0 < x/H < 4$	$4 < x/H < 8$	$x/H > 8$
mean (mm^{-1})	-0.438 ± 0.013	0.265 ± 0.015	0.323 ± 0.012
standard deviation (mm^{-1})	5.351 ± 0.009	5.376 ± 0.011	4.687 ± 0.009
skewness	-0.115	-0.149	-0.281

Similar to curvature distributions calculated for experimental results (see Table 3.2), DNS curvature distributions are approximately normal with means near zero. The curvature histograms shown in Fig. 4.17 deviate further from normal distributions than those for experimental measurements (see Fig. 3.15). This is likely due to the reduced window length
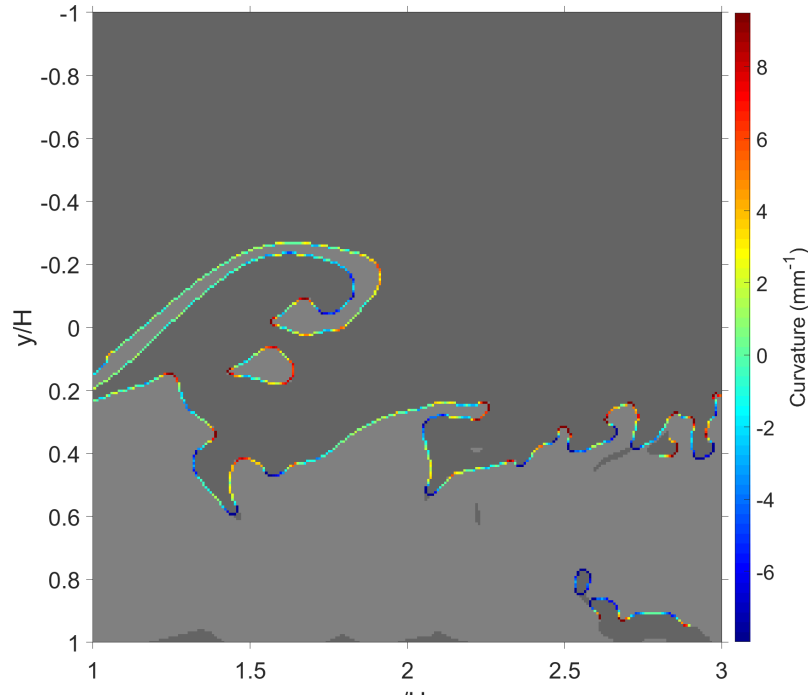
Figure 4.16: Instantaneous DNS flame front curvature.
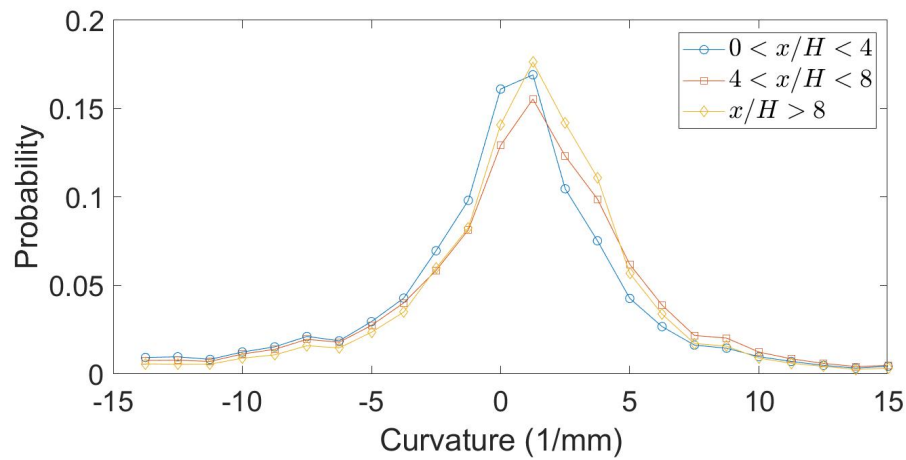
Figure 4.17: DNS flame front curvature probability density functions, PLIF simulated using Gaussian laser sheet.

w used to calculate curvature from DNS results. DNS flame front sections of length $w = 9$ pixels can be arranged in fewer distinct shapes than the flame front sections of length $w = 19$ pixels used for experimental calculations. Therefore, the DNS curvature calculation output has fewer possible discrete results than the experimental calculation, resulting in a "rougher" histogram.

DNS curvature distributions have standard deviations near 5 mm^{-1}, as opposed to experimental curvature distributions with standard deviations near 6 mm^{-1}. This indicates that flame structures produced by DNS have sizes in moderate agreement with experimental results. A systematic evaluation of the sensitivity of this agreement to algorithm parameters (binarization threshold levels, flame front curve fit order, etc.) has not been performed. Such an analysis could provide more context for future comparisons of experimental and simulated PLIF images.

In addition to enabling a quantitative comparison between experimental and computational results, the DNS curvature results also provide additional context to the resolution of the PLIF system discussed in Chapter 2. The calculated resolution of the PLIF experiment was 40 × 40 × 95 μm. The DNS results do not show evidence of flame structures with radii of curvature smaller than 40 μm (which would have curvature values greater than 25 mm^{-1}). This suggests that the PLIF experiment successfully resolved flame structures of all length scales smaller than the width of the field of view.

4.5 Comparison with other simulation results

Nielsen et al. [9] performed a computational investigation of the small-cavity flowpath using a hybrid large eddy simulation/Reynolds-averaged Navier Stokes (LES/RANS) method, and compared LES/RANS results with the small-cavity OH-PLIF images presented in Chapter 2. While LES/RANS does not resolve the finest flame wrinkling scales observed in the OH-PLIF images, the flame appears to propagate into the main flow at approximately the same angle in both experiment and simulation. Nielsen et al. also show that this flame angle is predicted well by the Peters one-dimensional turbulent flame speed relation [14]. A comparison between the LES/RANS model and OH-PLIF results is shown in Fig. 4.18.

Johnson et al. [118] and Goodwin et al. [119, 120] investigated the small-cavity scramjet configuration using 2D and 3D discontinuous Galerkin (DG) models. Results of this study

(a) Means   (b) Standard deviations
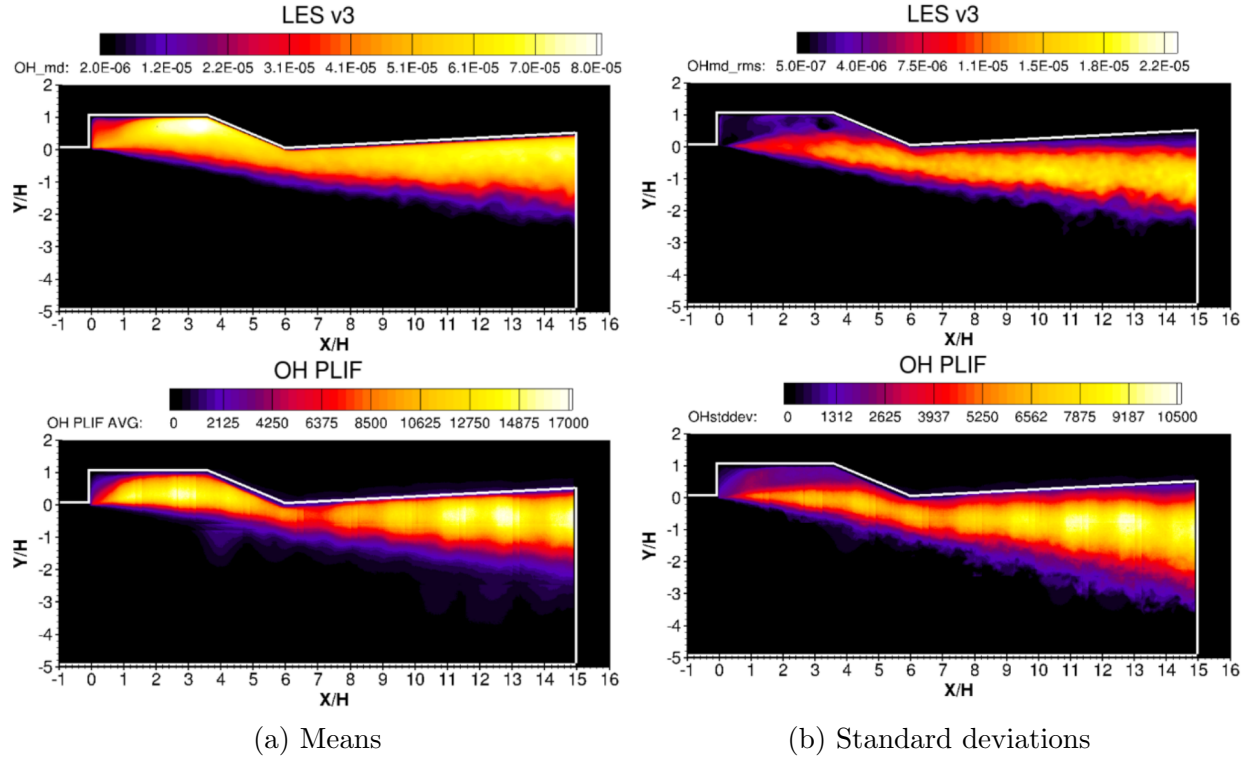
Figure 4.18: Comparison between LES/RANS OH molar density statistics and experimental OH-PLIF signal statistics, from Nielsen et al. [9]. Note that the positive y-direction in this figure is opposite that used elsewhere.

also show moderate agreement between the DG model, experimental OH-PLIF, and the Peters flame speed relation. Like DNS, OH reduction due to stretching around the aft ramp is observed in the DG model. An instantaneous image of Y_{OH} distribution across the 2D DG domain is shown in Fig. 4.19; it is immediately apparent that flame structure sizes are not replicated by this simulation at smaller scales. Binarization and curvature calculation confirms this; curvature distributions are presented in Table 4.3. Standard deviations of curvature distributions are much smaller than in experiments – between 3 and 4 mm^{-1}. The DG simulation produces significantly larger, less curved structures than are seen in experiments, possibly indicating an issue with the simulated inflow turbulence.
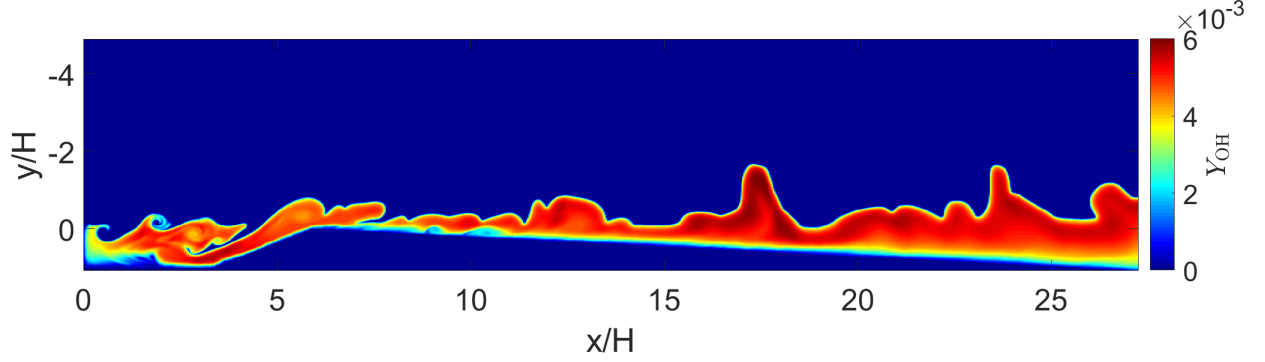
Figure 4.19: Instantaneous discontinuous Galerkin Y_{OH}, from [119, 120].

Table 4.3: Discontinuous Galerkin curvature distribution parameters

Region	$0 < x/H < 4$	$4 < x/H < 8$	$8 < x/H < 15$
mean (mm^{-1})	-0.324 ± 0.015	-0.050 ± 0.016	-0.021 ± 0.011
standard deviation (mm^{-1})	3.913 ± 0.015	3.342 ± 0.011	3.217 ± 0.008
skewness	0.341	-0.096	-0.112

4.6 Summary

This chapter presented an analysis of the structure of a cavity-stabilized flame produced by a direct numerical simulation model. Simulated OH PLIF images were produced from DNS outputs for comparison with experimental images. The effects of temperature and pressure variations on the LIF process were considered and found to have a negligible effect on the position of the flame front as identified from regions of high OH gradient. Laser sheet thickness has a much greater effect on the identified flame front position and shape; final simulated images approximated the PLIF signal that would be acquired with a Gaussian light sheet with a full-width at half-maximum of 95 μm.

Using methods previously applied to experimental results, OH intermittency and flame front curvature were computed from simulated PLIF images and used for direct quantitative comparison with experimental PLIF images. Flame structure sizes in the DNS output were in moderate agreement with experimental structures sizes, and the flame spread into the free stream at approximately the same angle as in experiments. The DNS output does not show OH recombination in the cavity; this may indicate that the chosen wall temperature

boundary conditions are set too high.

Chapter 5

Characterization of a high-spatial-resolution hybrid fs/ps CARS system

5.1 Motivation and objectives

Coherent anti-Stokes Raman scattering is a useful technique for noninvasive temperature and species measurement in combustion environments [44, 45]. Each CARS measurement provides an average of local temperature and species concentration values over the volume in which the pump, probe, and Stokes beams interact – the "interrogation volume". The size of the interrogation volume determines the extent to which CARS temperature and species measurements are averaged over space. Many environments of interest for CARS measurements involve very small spatial scales. For example, the flame thickness in premixed scramjet flames is expected to be on the order of 100 μm [121]. Spatial averaging effects have been observed in CARS measurements of a scramjet flame [64], a premixed swirl flame [63], and a turbulent pool fire [122]. Various methods exist for modeling and correcting for spatial averaging effects [123, 124, 64]. Another approach to this problem is to reduce

spatial averaging effects by reducing the size of the interrogation volume. For a BOXCARS phase-matching configuration, this can be achieved by increasing the crossing angle of the incoming beams or decreasing the diameter of the beams at the location of crossing.

An accurate method for measuring the interrogation volume size is needed for systematic minimization of the measurement volume and for characterizing final spatial averaging effects. As was discussed in Section 1.1.4, the size of this volume is commonly measured by translating a thin glass coverslip along the direction of beam propagation, and recording the rise and fall of nonresonant CARS signal generation in glass. Severe attenuation of all beams is required for this method, which potentially alters the result of the measurement. This chapter will discuss a reliable way to measure interrogation volume size without beam attenuation and investigate ways to minimize the size of the volume.

This chapter is structured as follows. First, the construction of a new ultrafast CARS system is described. A femtosecond laser source is used to create broadband pump and Stokes beams, while a pulse shaper is used to create a narrowband probe beam several picoseconds in duration. CARS signal was generated in air using a variety of beam crossing conditions; the CARS interrogation volume for each of these cases was measured using a microscale jet of nonresonant gas. From these measurements, the effects of beam focal length, crossing angle, and astigmatism on interrogation volume size are discussed. The uncertainty inherent in the glass coverslip measurement method is explored by measuring the interrogation volume with varying levels of beam attenuation. A computational model of the interrogation volume size is also presented and compared with experimental results.

5.2   CARS system design

A dual-pump fs/ps CARS system similar to that described by Dedic et al.   [125] was constructed. An ultrafast Ti:sapphire laser (Astrella, Coherent) centered at 798 nm was used as the source to produce 60 fs pulses at 1 kHz. To avoid self-phase modulation effects during

beamsplitting, the amplified beam was split prior to pulse compression and one portion was directed to an external compressor module. The output of the internal compressor had pulse energy ~3.5 mJ and was used to pump an optical parametric amplifier (OPA, Topas, Light Conversion), which produced a pulse with tunable frequency through optical parametric generation and subsequent frequency mixing for use as the vibrational pump pulse. For all results in this chapter, the vibrational pump pulse was tuned to a central wavelength of 678 nm using the second harmonic of the OPA signal pulse. The output of the OPA was about 375 µJ; using a polarizing beam splitter, the energy of the vibrational pump pulse was reduced to about 70 µJ. It was further attenuated as needed using neutral density filters.

The output of the external compressor was also split, and one portion is directed into a $4f$ pulse shaper with a $f = 200$ mm cylindrical lens to form a narrowband probe pulse. The $4f$ pulse-shaping technique [126] used a grating and lens to disperse the laser beam, then focus to a Fourier plane. The distance from grating to lens and from lens to Fourier plane was f. At the Fourier plane, an adjustable slit was used to block all but the central frequency and a mirror routed the resulting narrowband ps pulse back through the lens and grating for recollimation.

The other portion of the external compressor output was split again into two equally-intense pulses for use as the Stokes and rotational pump beams. Stokes and rotational pump beams had fine energy adjustment using a half-waveplate and two polarizing beam splitters. Probe energy was typically kept at a constant value. In Section 5.4.7, it was attenuated using neutral density filters.

Each of the four beams was routed through delay stages to ensure temporal overlap, and a final half-waveplate for each line allowed fine polarization adjustment. The two pump beams were aligned approximately-collinearly through a dichroic, and the beams were focused at the interrogation volume using a 300 mm lens in a folded BOXCARS phase-matching configuration. The resultant CARS signal was directed into a 0.32 m spectrometer (IsoPlane-320, Teledyne Princeton Instruments) with a 1200 g/mm grating and resolution 0.034 nm.

When necessary, CARS signal was attenuated using neutral density filters. Spectra were recorded using an electron-multiplied CCD camera (ProEM, Teledyne Princeton Instruments) capable of kHz imaging. Broadband (~ 245 cm^{-1}) pulse generation using fs pulses can used to simultaneously excite transitions of multiple species of interest, including N_2, O_2, C_2H_4, and CO_2. A schematic of the CARS system is shown in Fig. 5.1.
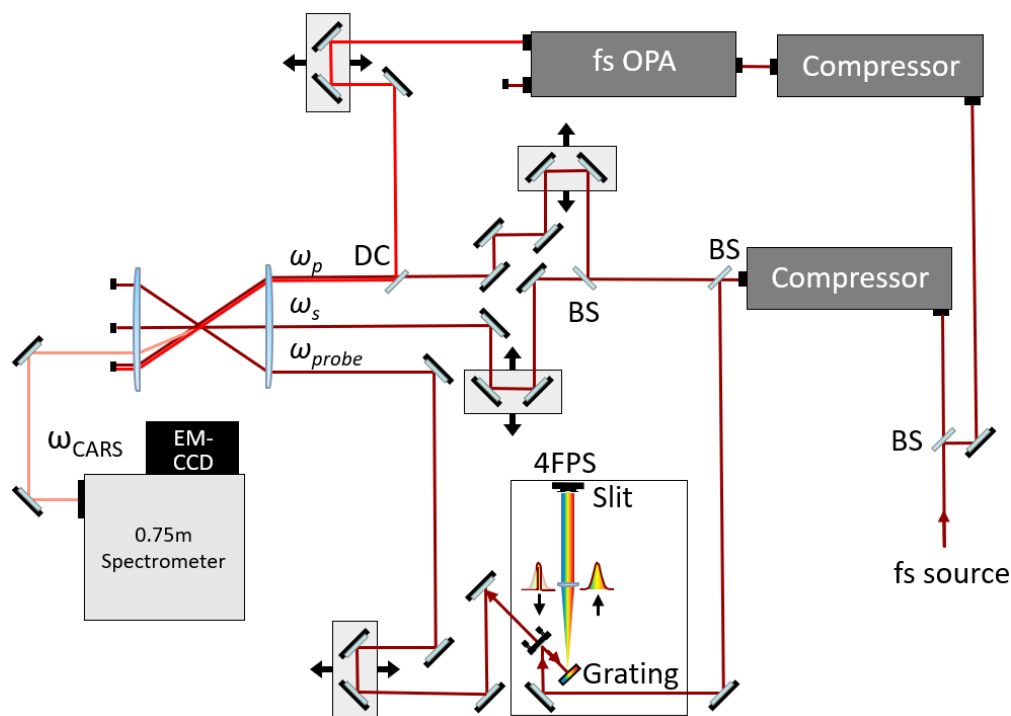
Figure 5.1: fs/ps CARS optical setup. Abbreviations: BS, beam splitter; OPA, optical parametric amplifier; 4FPS, $4f$ pulse shaper; DC, dichroic.

5.3 CARS measurement challenges

5.3.1 Robustness

Ultrafast CARS measurements of combustion environments face several major challenges that impose limits on any given CARS system. One challenge particularly relevant to the current system is that of robustness. When the system was first completed, the CARS signal level would at times remain stable over the course of hours; at other times, a gradual, unexpected
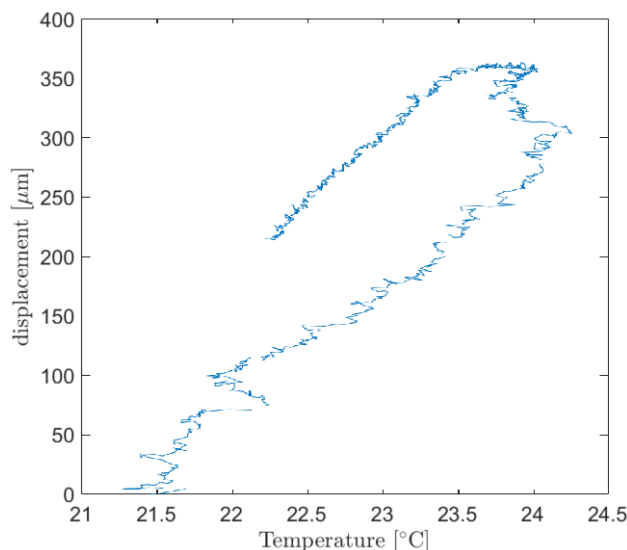
Figure 5.2: Probe focus position vs. room temperature over the course of 850 minutes, prior to system improvement.

decrease was observed. When this decrease occurred, it could be fixed by making small adjustments to the mirrors immediately prior to the focusing lens. This was found to be the result of room temperature fluctuations in the U.Va. Reacting Flow Laboratory. Figure 5.2 shows the variation in the position of the focus of the probe beam (as measured by a CCD beam profiling camera) over more than 14 hours, as the temperature in the room (as measured by a thermocouple on the main optical table) varied by about 3° C. The probe beam focus drifted by 350 μm during this time, enough to completely inhibit CARS signal generation. The drift also displayed hysteresis; after the room temperature rose and fell again, the beam position would not return to its previous value. While change in position with temperature was observed for all beams, the probe beam exhibited the largest change.

Several changes were made to the system to mitigate this problem. Optical mounts identified as temperature-sensitive were replaced. Air handling in the laboratory was changed to restrict room temperature to tighter bounds. Finally, hot air being expelled from the chiller attached to the Astrella laser was ducted outside of the building (rather than expelled into the room air) in order to improve laboratory temperature stability. This improved but did not completely eliminate the problem. Figure 5.3 shows CARS signal variation with time
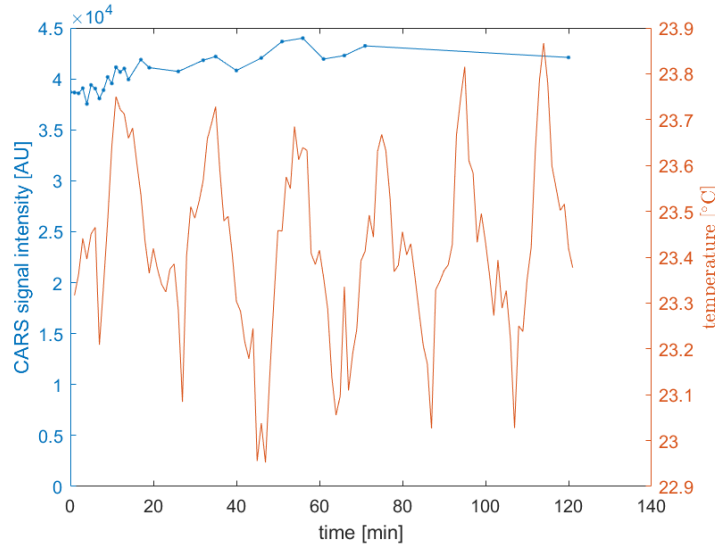
Figure 5.3: CARS signal and room temperature, shown as a function of time, post system improvement.

while the room temperature was well-controlled by the air handling system. Temperature in the room rises and falls within ± 0.5 °C and the intensity of the acquired CARS signal remains steady.

Future test campaigns in the scramjet facility using this (or another) ultrafast CARS system will have to address this problem by improving the temperature sensitivity of optics. The room containing the scramjet must remain very well ventilated and is therefore very susceptible to room temperature fluctuations during experiments. Systematic testing of each optical component for temperature sensitivity will likely be required.

Additionally, the CARS system was required to be robust with respect to the movement of the four translation stages used to overlap the pulses in time. The direction of beam travel was required to be aligned to the direction of stage travel with a high degree of precision such that movement of these stages would modify the relative arrival time of the beams at the interrogation volume without changing the positions of the beams in space. Furthermore, Appendix A documents an application of the CARS system in which the interrogation volume is moved in space. This requires optics for beam injection and optics for CARS signal collection to be mounted on systems of translation stages which must also be carefully aligned

with beam propagation directions. The appendix includes a test of the sensitivity of the positions of these beams to stage movement.

5.3.2   Accuracy and precision

Characterization and improvement of the accuracy and precision of CARS measurements is another important consideration for the design of CARS experiments. Kearney [52] used hybrid fs/ps rotational CARS to measure temperature and O_2/N_2 ratio in Hencken and McKenna flames, indicating 1–3% accuracy and 1–2% precision. Similar values were obtained for Hencken burner measurements by Miller et al. [127]. The accuracy and precision of fs/ps CARS can exceed that of ns CARS; Seeger and Leipertz [65] measured the temperature of hot air using vibrational and rotational ns CARS with 2–5% accuracy and 3–5% precision. The increased accuracy and precision is likely attributable to improved stability of laser sources and lower susceptibility to nonresonant and collisional interferences.

High-accuracy CARS measurements are desirable in experiments aiming to improve computational chemical-kinetic models. For example, one-dimensional models of C_2H_4-air combustion in a counterflow diffusion flame have uncertainties in maximum temperature as large as 2% at the high-strain extinction limit [128, 129]. CARS measurements of extinction temperatures could reduce uncertainties in chemical reaction rate constants, but only if measurement accuracy is within 2%.

Hencken burner vibrational CARS measurements were made using the present system at several different equivalence ratios. Temperatures were calculated for measured spectra using a time- and frequency-resolved fs/ps CARS model [130, 51] and compared to adiabatic-equilibrium flame temperature calculations [131]. Two selected spectra are shown in Fig. 5.4a, and a comparison between measured temperatures and calculations is shown in Fig. 5.4b. The measurements show strong agreement with calculations for low flame temperatures but precision becomes unacceptable for $\phi \geq 1$ due to decreased signal-to-noise ratio at high temperatures and due to temperature-related drift in beam positions, as discussed in Section
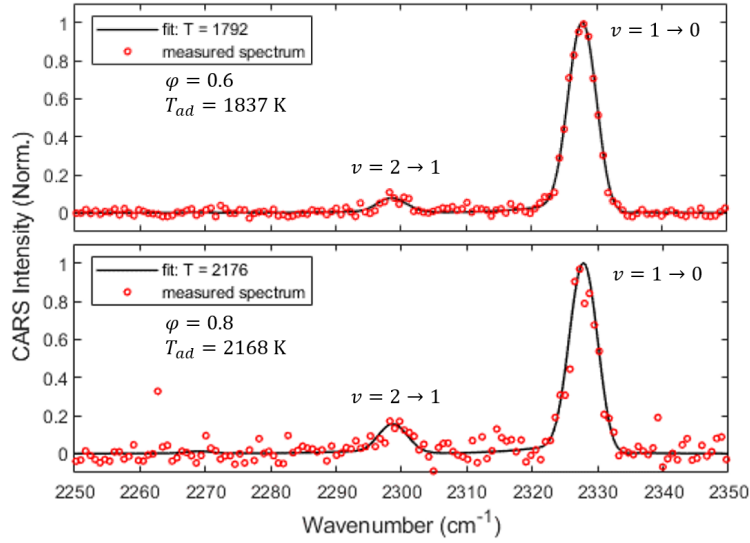
(a) Selected CARS spectra.
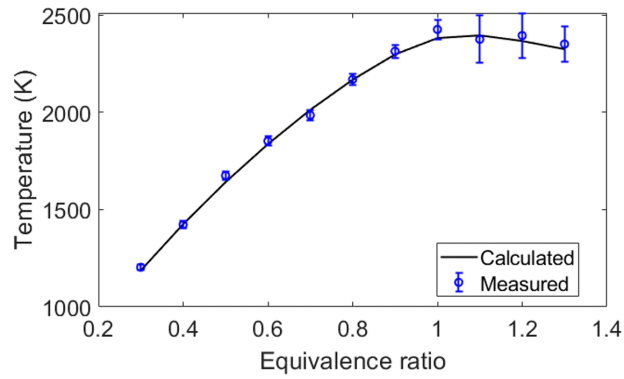
(b) Temperature measurements. Error bars encompass $\pm\sigma$.

Figure 5.4: Vibrational CARS measurements of a Hencken burner.

5.3.1. Data presented in Fig. 5.4 were collected prior to the system robustness improvements described in Section 5.3.1. These improvements are expected to improve signal-to-noise ratio and measurement precision.

To optimize accuracy and precision of measurements, it is important to avoid gas breakdown and Raman transition saturation effects that can occur when the energies of the incoming beams are increased above a threshold level [25, 132]. Gas breakdown introduces broadband noise that varies in intensity between acquisitions, reducing measurement precision. Transition saturation can alter the relative intensities of signal peaks, reducing measurement
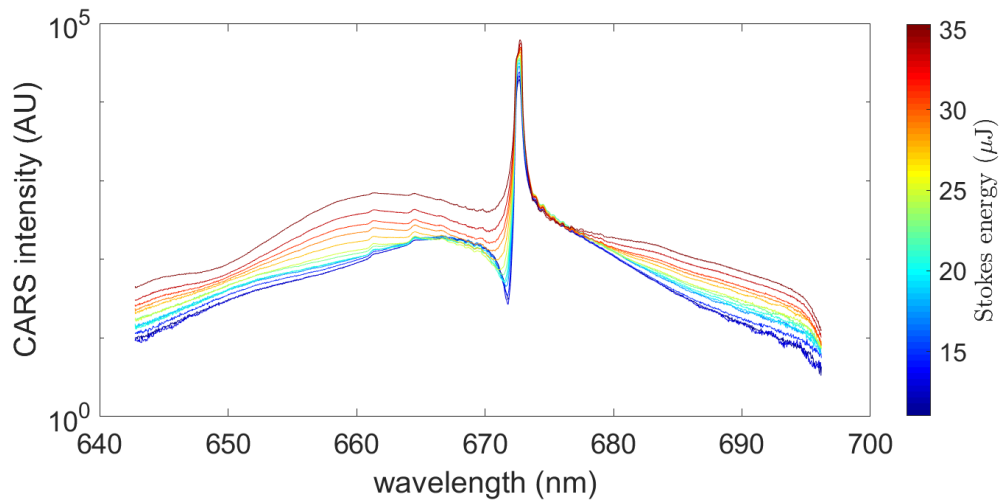
Figure 5.5: Vibrational CARS spectra at several Stokes energy values (logarithmic y-axis scale).

accuracy.

At each of the CARS generation cases discussed later in this chapter, pump and Stokes beam energies were manipulated in order to maximize the available signal while avoiding both saturation of the CARS transitions and gas ionization. Fig. 5.5 shows vibrational CARS spectra acquired at several different values of Stokes beam energy with no probe delay. (These spectra were acquired at the Case B beam configuration, as defined in Section 5.4.4.) Resonant N_2 CARS signal is seen as the sharp peak around 672 nm. At low Stokes energies, the smaller peak around 668 nm is the nonresonant contribution. As Stokes energy is increased above about 15 µm/pulse (for this case), saturation and ionization effects distort the shape of the spectrum to either side of the resonant peak.

The remainder of this chapter discusses improvements to spatial resolution. This also reduces measurement uncertainty by reducing spatial averaging in environments with large spatial gradients of temperature and species concentration.

5.3.3 Resolution

Characterizing the spatial resolution of the ultrafast CARS system and improving that resolution are two main goals of this work. The extent of the spatial averaging inherent in a given CARS measurement is critical for interpreting the results produced. For example, CARS measurements applied to the scramjet combustor, if finely-resolved, could provide kHz-rate point-based measurements of flame intermittency as measured by high temperatures or the presence of product species. However, if the measurement volume were very large (> 1 mm in length), it would routinely average regions of products and regions of reactants together. Other applications, such as the measurement of high-pressure counterflow flames [129, 133], also require very small interrogation volumes to probe very thin reaction zones with lengths on the order of hundreds of microns.

Figure 5.6 serves as a demonstration for the need to understand and account for spatial averaging in CARS measurements. Previously, Dedic et al. [134, 51] used rotational and vibrational hybrid fs/ps CARS to study vibrational-rotational nonequilibrium in a plasma and surrounding shock wave generated by a ns-laser spark. Temperature measurements were acquired close to the shock wave at multiple time steps as the shock wave expanded radially. Shadowgraph images acquired at 700 ns and 1800 ns after the ns-laser spark are shown in Figs. 5.6a and 5.6b with the approximate position of the ~ 1 mm interrogation volume overlaid. Rotational temperature measurements differed between the two time steps, as shown in Figs. 5.6c and 5.6d. However, as the shock curvature was greater at the earlier time step, temperature gradients along the interrogation volume length were significant, as evidenced by the mismatch between the experimental data and the best-fit simulation. In this case, spatial averaging biases the best-fit temperature to low-temperature gas within the interrogation volume. Without a well-characterized value for the spatial resolution of the CARS system, it is unknown to what extent the difference in measured temperature is due to spatial averaging over these temperature gradients.

(a) Interrogation volume 1 mm from initial kernel center

(b) Interrogation volume 2 mm from initial kernel center

(c) CARS spectrum 1 mm from initial kernel center

(d) CARS spectrum 2 mm from initial kernel center
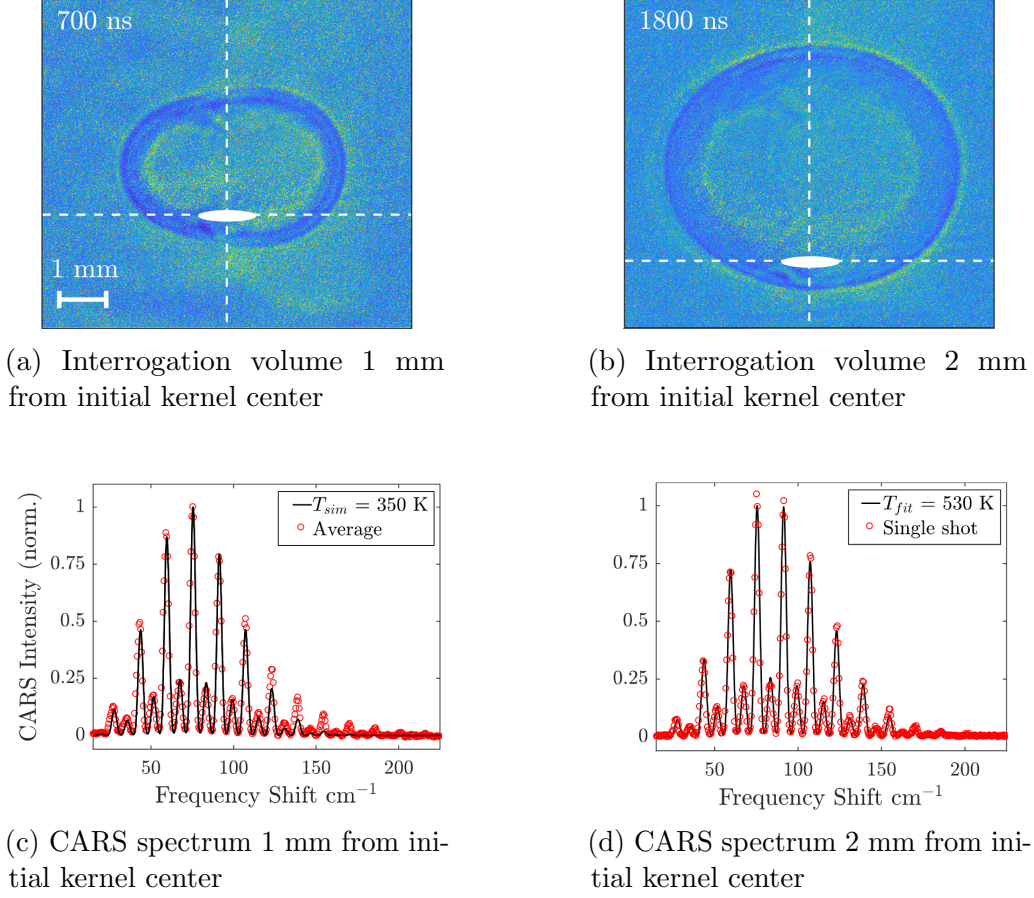
Figure 5.6: Rotational CARS measurements near a shock wave produced by a ns laser spark [134, 51].

5.4   Interrogation volume characterization

5.4.1   fs/ps CARS generation

The CARS process generates a signal proportional to the square of the sum of third-order polarization terms arising from nonresonant wavemixing and the CARS process, as shown in Eq. (5.1) [25, 130].

$$I_{\mathrm{CARS}}\left(\omega, \tau_{12}, \tau_{23}\right) \propto \left| P_{NR}^{(3)}\left(\omega, \tau_{12}, \tau_{23}\right) + P_{\mathrm{CARS}}^{(3)}\left(\omega, \tau_{12}, \tau_{23}\right) \right|^2 \tag{5.1}$$

The four interacting electric fields will be denoted in this section using subscripts 1 (pump), 2 (Stokes), 3 (probe), and 4 (CARS). Interactions between the electric fields and the medium

that are resonant with real molecular transitions produce the resonant polarization $P_{\text{CARS}}^{(3)}$. The nonresonant polarization $P_{\text{NR}}^{(3)}$ is produced by interactions involving virtual states only. Energy diagrams for resonant and nonresonant CARS processes are shown in Fig. 5.7. The polarizations are both dependent on the delay in time between the pump and Stokes pulses, τ_{12}, and the delay between the Stokes and probe pulses τ_{23}.
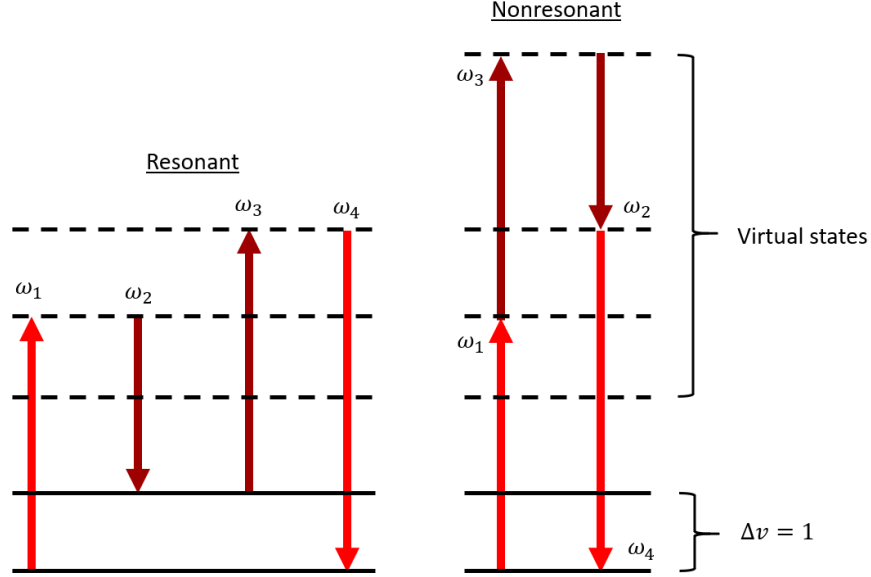
Figure 5.7: Resonant and nonresonant CARS energy diagrams.

The time-domain representation of the resonant polarization is given in Eq. (5.2) [130, 135]. Here, $\times$ is the convolution operator and $E_n e^{i\omega_n t_n}$ are the incoming electric fields with field strengths E_n, frequencies ω_n, and coherence timescales t_n.

$$
\begin{aligned}
P_{\text{CARS}}^{(3)}\left(t, \tau_{12}, \tau_{23}\right) = \left(\frac{i}{\hbar}\right)^3 &\int_0^\infty dt_3 \int_0^\infty dt_2 \int_0^\infty dt_1 \Big[R_4\left(t_3, t_2, t_1\right) \\
\times\ & E_3\left(t - t_3\right) E_2^*\left(t + \tau_{23} - t_3 - t_2\right) \\
\times\ & E_1\left(t + \tau_{23} + \tau_{12} - t_3 - t_2 - t_1\right) \\
\times\ & e^{i(\omega_1 - \omega_2 + \omega_3)t_3} e^{i(\omega_1 - \omega_2)t_2} e^{i\omega_1 t_1} \Big]
\end{aligned}
\tag{5.2}
$$

R_4 is the molecular response function for the CARS process. The molecular response is

often assumed to be instantaneous over the t_1 and t_3 timescales. In this simplification, R_4 is represented by Eq. (5.3) [130]. Here, I_{ca} are transition strengths weighted according to Boltzmann populations, ω_{ca} are Bohr frequencies for those transitions, and Γ_{ca} are collisional dephasing rates for those transitions, where initial states are denoted a and Raman active states are denoted c. The Heaviside step function is represented by θ.

$$R_4\left(t_2\right) = \sum_{a,c} I_{ca}\theta\left(t_2\right) e^{-i\omega_{ca}t_2 - \Gamma_{ca}t_2} \tag{5.3}$$

With a sufficient probe delay τ_{23}, the nonresonant CARS polarization is suppressed [136], and CARS signal intensity can be described in the frequency domain using the Fourier transform of $P_{\mathrm{CARS}}^{(3)}\left(t,\tau_{23}\right)$ as shown in Eq. (5.4), where ω refers to the frequency of the CARS signal.

$$I_{\mathrm{CARS}}\left(\omega\right) \propto \left|P_{\mathrm{CARS}}^{(3)}\left(\omega\right)\right|^2 = \left|\sqrt{\frac{1}{2\pi}}\int_{-\infty}^{\infty} P_{\mathrm{CARS}}^{(3)}\left(t,\tau_{23}\right) e^{-i\omega t} dt\right|^2 \tag{5.4}$$

In the frequency domain, CARS signal intensity can be expressed using the frequency-domain CARS polarization susceptibility $\chi_{\mathrm{CARS}}^{(3)}$, which is related to R_4 through the Fourier transform.

$$I_{\mathrm{CARS}}\left(\omega,\vec{r}\right) \propto \left|\epsilon_0\chi_{\mathrm{CARS}}^{(3)}E_1\left(\omega_1,\vec{r}\right)E_2\left(\omega_2,\vec{r}\right)E_3\left(\omega_3,\vec{r}\right)\right|^2 \tag{5.5}$$

The CARS polarization susceptibility is directly proportional to the number density N of resonant species [25]. The three incoming electric fields vary in amplitude over space. Therefore, for the current work, the total CARS signal intensity can be considered to be the integral over space of a function of local values for density and field amplitude, as shown in Eq. (5.6).

$$I_{\mathrm{CARS}} \propto \int_{-\infty}^{\infty}\int_{-\infty}^{\infty}\int_{-\infty}^{\infty} N^2\left|E_1E_2E_3\right|^2 dxdydz \tag{5.6}$$

The quantity $|E_1E_2E_3|^2$ is expected to vary as a three-dimensional Gaussian distribution as shown in Eq. (5.7). For a folded BOXCARS phase matching configuration with beams inclined by a crossing angle $\alpha < 45°$ from a central axis z, the distribution is expected to resemble a prolate ellipsoid with $\sigma_x = \sigma_y < \sigma_z$.

$$I_{\text{CARS}} \propto \int_{-\infty}^{\infty} \int_{-\infty}^{\infty} \int_{-\infty}^{\infty} \frac{N^2}{2\pi\sigma_x\sigma_y\sigma_z} \exp\left(-\frac{x^2}{2\sigma_x^2} - \frac{y^2}{2\sigma_y^2} - \frac{z^2}{2\sigma_z^2}\right) dxdydz \qquad (5.7)$$

The spatial extent of the interaction between the three incoming electric fields is the interrogation volume (which is in literature often termed the "probe volume" or the "interaction volume").

5.4.2 Micro-scale jet measurement

The size of the interrogation volume of the CARS system was measured using a microscale jet. A 33-gauge needle (Hamilton, ID 108 μm, OD 210 μm) was placed on a system of three translation stages. Argon (Ar) flowed through the needle at 0.049 SLPM. When the nonresonant jet was intersected with the CARS interrogation volume, the resonant N_2 CARS signal dropped. As the jet was translated through the volume, the magnitude of the signal drop could be recorded as a function of position along the principal axes of the interrogation volume. In order to use this jet for quantitative measurements of CARS resolution, the size of the jet was first measured using a technique known as femtosecond laser electronic excitation and tagging (FLEET), in which a high-energy, short-duration pulse is used to electronically excite gaseous species, resulting in a visible broadband emission as the species returns to the ground state [137, 138].

In air, the laser pulse caused N_2 to dissociate into N atoms which recombine into excited electronic states. The primary contributor to the long-lived N_2 FLEET emission is the $B^3\Pi_g \to A^3\Sigma_u^+$ transition. This produces emission between 500 and 950 nm with duration on the order of 100 μs. In Ar-air mixtures, energy moves from excited argon atoms (Ar* 4^3P_2)

to ground-state N_2, moving more molecules to excited N_2 states and increasing the overall intensity of the FLEET signal. The presence of Ar also enhances FLEET signal by encouraging the dissociation of N_2 and reducing the rate of collisional quenching of N_2 with itself. In pure Ar and in Ar-air mixtures, emissions with durations on the order of 10 μs are also produced by Ar ionization-recombination processes [139].

A mirror was placed at the output of the external compressor; this was used to direct the beam through a spherical lens of focal length 300 mm. A region of ionized air was produced at the focus of this beam. An intensified CCD camera (PIMAX 4, Princeton Instruments) was set up to image the FLEET signal using a 105 mm lens (Nikon Nikor) and a 750 nm shortpass filter (Thorlabs FES0750) in order to block reflections of the 800 nm laser light. The camera was focused on the region of ionization. The needle was positioned vertically, directly underneath the ionization region. As the needle was translated closer to the beam center, beams began to ablate the needle; this imposed a minimum distance between the beam center and the needle for the jet measurements described here. The needle was translated downward, and FLEET images were acquired at 15 different needle positions. Background images were collected at each position with the Ar jet off. Natural light and ICCD images of the FLEET measurement are shown in Fig. 5.8. Figure 5.9 presents profiles of Ar FLEET signal along the direction of laser beam propagation. Figure 5.10 shows the variation of FLEET signal and the FWHM of the Ar FLEET signal profile as the needle is translated away from the laser beam focus. For about one millimeter (or about five needle inner diameters) downstream of the needle exit, the jet had a relatively-constant width of about 86 μm.
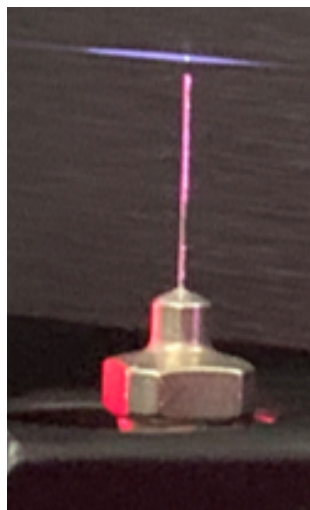
(a) Natural light.
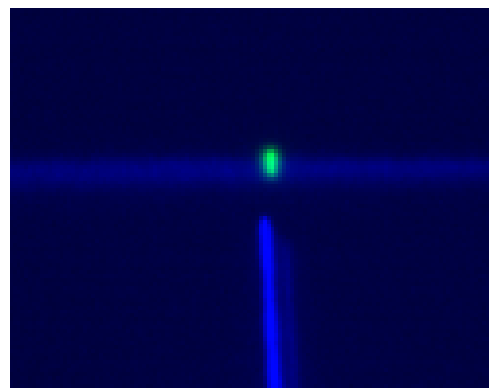
(b) ICCD images. In blue, FLEET signal with no Ar jet (and laser scatter off of the needle). In green, FLEET signal with Ar jet.

Figure 5.8: Micro-scale Ar jet enhancing FLEET emission.
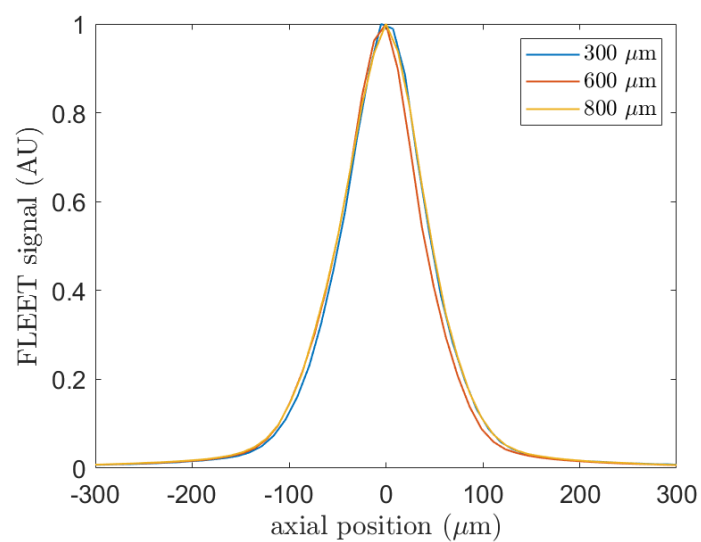
Figure 5.9: Normalized FLEET signal axial profiles, at three distances from needle exit.
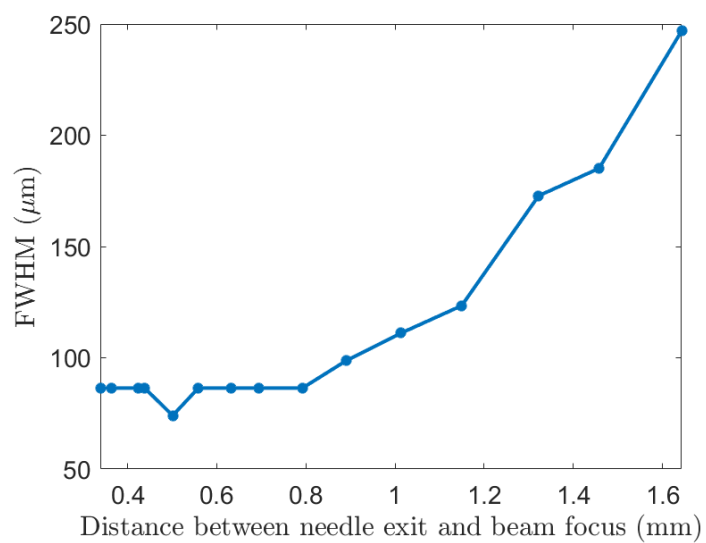
Figure 5.10: FLEET signal variation with jet position.

5.4.3 Data collection and processing

CARS signal was produced in air using various different focusing lenses and beam positions; these will be detailed in the following sections. A schematic of an example BOXCARS beam crossing configuration is shown in Fig. 5.11. The coordinate system originates at the foci of the beams. The beams propagated along an axis inclined by a shallow crossing angle α relative to the z-axis. The resulting probe volume had a major axis along the z-axis; measurements in this direction will be termed "axial direction measurements". Measurements made perpendicular to this axis will be termed "transverse direction measurements".
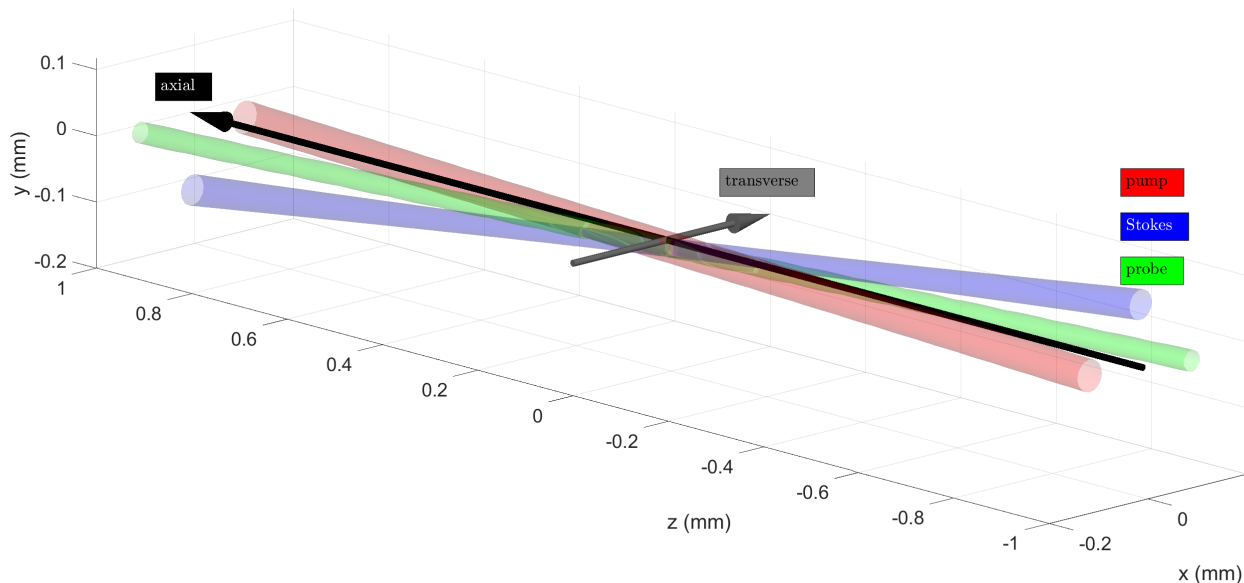
Figure 5.11: Beam crossing coordinate system and terminology.

At each case, beam energies, polarizations, and relative delays were changed to optimize CARS signal. A 5 ps probe delay was used to suppress nonresonant signal. The jet was moved with translation stages to be centered on the interrogation volume; this was done by finding the jet position at which N_2 CARS signal was minimized. A schematic depicting the jet measurement technique is shown in Fig. 5.12. The vertical needle height was set as close

as possible to the interrogation volume. As the needle was raised it would begin to scatter the vibrational pump beam into the spectrometer; this enforced a maximum vertical position on the needle. CARS spectra were acquired at many different points in axial and transverse directions. At each point, 3,000 spectra were acquired at a rate of 1,000 Hz; these were used to create an average spectrum. Occasionally, an event such as light scattering off dust would saturate the spectrometer camera sensor; these outliers were removed. A set of background spectra were acquired with the probe beam blocked for each beam crossing configuration. Then, the CARS signal recorded at each point $S(x)$ was the sum of pixel intensities across the entire spectral range of resonant signal generation.
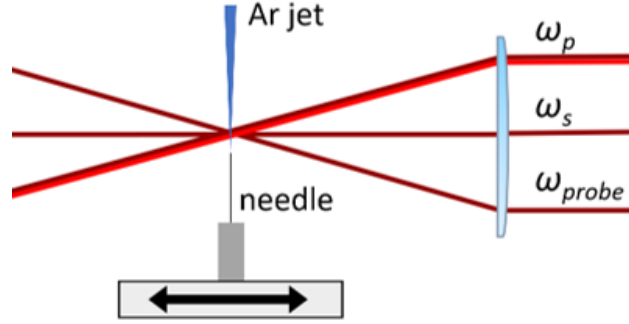
Figure 5.12: Schematic of resolution measurement using the nonresonant jet.

The size of the interrogation volume itself can be determined analytically, as discussed next. A Gaussian function $f(x)$ is used to approximate the profile of Ar concentration within the jet. More specifically, $f(x)$ is an approximation for the Ar concentration as a function of position along a line passing through the axis of the jet, near to the jet exit. This function has a known variance σ_f^2 from the FLEET images.

$$f(x) = a_f \exp\left[\frac{-(x - \mu_f)^2}{2\sigma_f^2}\right] \tag{5.8}$$

Another Gaussian function $g(x)$ is used to approximate the local CARS signal irradiance along one of the axes of the interrogation volume. This function has an unknown variance σ_g^2.

$$g\left(x\right) = a_g \, \exp\left[\frac{-\left(x - \mu_g\right)^2}{2\sigma_g^2}\right] \tag{5.9}$$

As the jet was passed through the interrogation volume, N_2 CARS signal dropped to a minimum and then returned to a baseline value as the jet and interrogation volume interact. $h(x)$ can then be defined as the positive change in signal as a function of jet position; it is the convolution of $f(x)$ and $g(x)$.

$$h\left(x\right) \equiv f\left(x\right) * g\left(x\right) = \int_{-\infty}^{\infty} f\left(\tau\right) g\left(x - \tau\right) d\tau \tag{5.10}$$

The two Gaussian functions can be convolved analytically. $h(x)$ is also a Gaussian function with a variance $\sigma_h^2 = \sigma_f^2 + \sigma_g^2$.

$$h\left(x\right) = a_f a_g \int_{-\infty}^{\infty} \exp\left[\frac{-\left(\tau - \mu_f\right)^2}{2\sigma_f^2}\right] \exp\left[\frac{-\left(x - \mu_g - \tau\right)^2}{2\sigma_f^2}\right] d\tau \propto \exp\left[\frac{-\left(x - \mu_h\right)^2}{2\left(\sigma_f^2 + \sigma_g^2\right)}\right] \tag{5.11}$$

Therefore, because the width of the jet and the width of the jet/interrogation volume interaction are known, the width of the interrogation volume can be calculated. In this work, the widths of these functions and the diameters of individual laser beams will be reported using the $1/e^2$ beam diameter (or $1/e^2$-full-width) $2w = 4\sigma$. The beam radius w is the spatial distance between the maximum value of the function and the location at which the function has fallen to $1/e^2$ of maximum. Using this definition, the widths of the three functions satisfy the relationship $\left(2w_h\right)^2 = \left(2w_f\right)^2 + \left(2w_g\right)^2$.

The CARS signal acquired as a function of jet position is termed $S\left(x\right)$. It had a baseline signal value S_0; this is the CARS signal level when there was no interaction with the jet. The baseline CARS signal was observed to drift gradually in some cases, therefore S_0 is modeled as a linear function. A best-fit model can be applied to $S\left(x\right)$; this model is shown in Eq. (5.12). The model has fitting constants $S_0\left(0\right)$ (baseline signal at $x = 0$), m (baseline signal
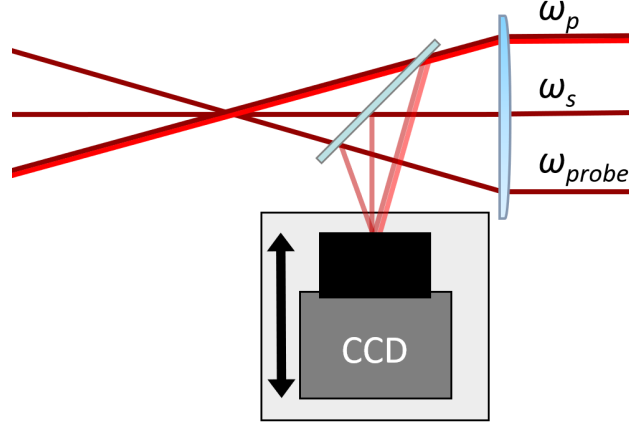
Figure 5.13: Beam profiler system schematic.

slope), a (amplitude of signal drop), μ_h (jet center position), and σ_h (jet center standard deviation).

$$S(x) = S_0(x) - h(x) \approx S_0(0) + mx - a \cdot \exp\left[\frac{-(x - \mu_h)^2}{2\sigma_h^2}\right] \tag{5.12}$$

In order to visualize the interaction between the CARS beams, a fused silica window was placed in the beam path directly after the focusing lens. The weak reflections of each beam produced by the beam splitter were attenuated by neutral density filters, and imaged directly onto the sensor of a CCD camera (Blackfly, Point Grey). A translation stage was used to move the camera along the average direction of beam propagation (hereafter termed the "axial direction" $\hat{z}$), allowing cross-sectional images of each beam to be acquired at various axial positions. The beam splitter was then removed whenever CARS measurements were made using the spectrometer. A schematic of the beam profiling system is shown in Fig. 5.13.

Using the beam profile images, for any given beam crossing condition, the location z_c of beam crossing relative to the beams' foci could be determined. A schematic of two different crossing configurations is shown in Fig. 5.14. The position at which the beams were imaged closest to one another on the CCD sensor was used to approximate the beam crossing position. The beam images typically did not overlap perfectly at any position; a beam sampler with improved surface flatness could improve beam image overlap in future studies.

(a) Beams crossing at foci.

(b) Beams crossing away from foci.
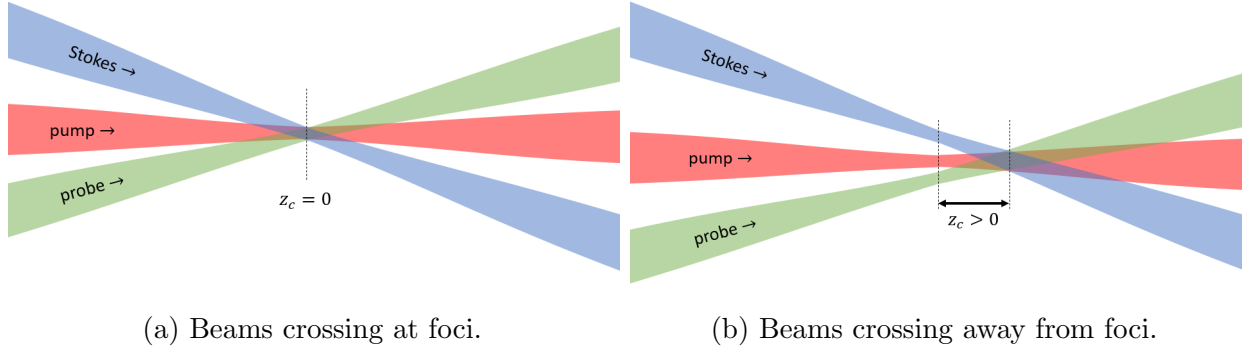
Figure 5.14: Beam crossing configurations

The diameter of each beam at the crossing position was approximated from the beam profile images. In some cases, the intensity distribution of the beam profile often deviated significantly from a radially-symmetric Gaussian beam. These beam profiles were elliptic with major and minor axes of different lengths. In order to evaluate both major and minor beam diameters at the crossing position, a two-dimensional Gaussian function of the form shown in Eq. (5.13) was fitted to the beam profile images. Here, $x' = x\cos\theta + y\sin\theta$ and $y' = -x\sin\theta + y\cos\theta$ are the major and minor axes of the beam profile, inclined by an angle θ from the image axes x and y. The fitting routine has coefficients θ, $\mu_{x'}$ and $\mu_{y'}$ (profile center coordinates), $\sigma_{x'}$ and $\sigma_{y'}$ (profile standard deviations), and a (maximum 8-bit intensity on the CCD sensor).

$$I(x,y) = a \cdot \exp\left\{-\left[\frac{(x\cos\theta + y\sin\theta - \mu_{x'})^2}{2\sigma_{x'}^2} + \frac{(-x\sin\theta + y\cos\theta - \mu_{y'})^2}{2\sigma_{y'}^2}\right]\right\} \quad (5.13)$$

5.4.4 Effects of lens focal length

The system was aligned to produce vibrational CARS signal with four different combining lenses of diameter 50.4 mm and with focal lengths 150, 200, 250, and 300 mm. Pump, probe, and Stokes beams were directed into the single focusing lens; each beam propagated parallel to the lens axis but offset from it, such that the beams would cross in a BOXCARS
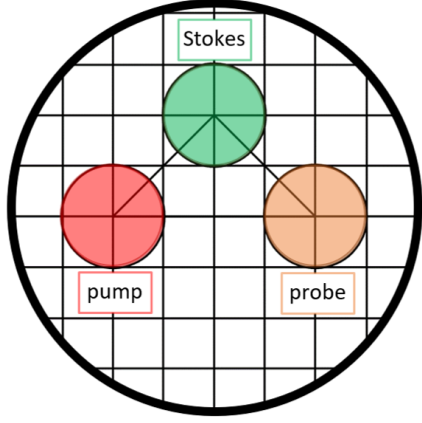
(a) Beam positions on combining lens with diameter 50.4 mm.
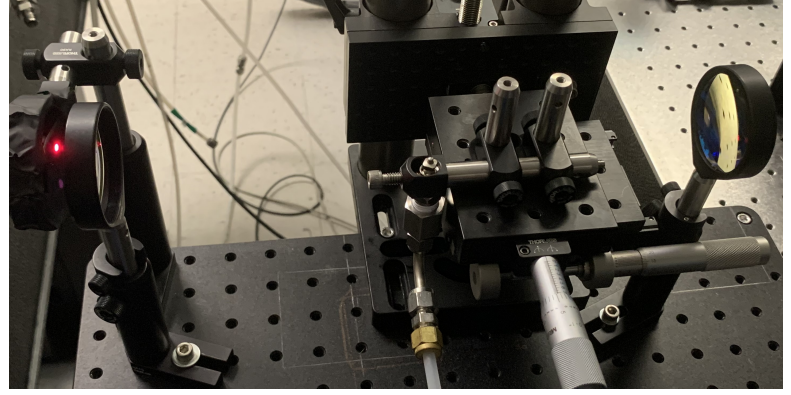
(b) Case A configuration, 150 mm focal length

Figure 5.15: Single combining lens configuration.

phase-matching configuration close to their foci. Beam positions on the combining lens are shown in Fig. 5.15a. Fig. 5.15b shows an image of one of the lens configurations, and Table 5.1 lists relevant parameters for each case: lens focal lengths f, crossing angles α, pulse energies U, crossing positions z_c, and beam diameters (in both major and minor axes) at the crossing position $2w(z_c)$. A fifth case with a focal length of 400 mm was attempted. However, no appreciable drop in signal as a result of the Ar jet was observed due to the large size of the interrogation volume relative to the jet. In future studies, volumes longer than those reported here (produced by large lens focal lengths or shallow crossing angles) could be measured using jets with larger diameters.

Table 5.1: Focal length experiment cases. Lengths in [mm], energies in [µJ/pulse].

Case	f	z_c	α	U_{pump}	U_{probe}	U_{Stokes}	$2w_{pump}(z_c)$	$2w_{probe}(z_c)$	$2w_{Stokes}(z_c)$
A	150	0	4.9°	22	38	26	40, 150	62, 63	34, 42
B	200	-1.6	3.6°	20	38	25	77, 49	106, 30	66, 78
C	250	-1.6	2.9°	28.5	38	27	80, 60	95, 35	67, 85
D	300	-1.5	2.4°	39.7	38	35	90, 71	82, 39	57, 81

Figure 5.16 shows CARS intensity as a function of jet position in both axial and transverse directions for Case B. (The width of the jet has not yet been deconvolved from these measured data.) Symbols represent measured data. The dashed line is the best-fit model applied

to the data, as described in Eq. (5.12). Jet scan figures for other cases can be found in Appendix B.2. As expected, the width of the signal drop in the transverse direction was always smaller than the width in the axial direction. The magnitude of the drop in signal varied between about 20% and 80% of the baseline signal. When the interrogation volume was large, the Ar jet evacuated only a small portion of the N_2 present within the volume. When the interrogation volume was small, the volume evacuated by the jet was much more significant.
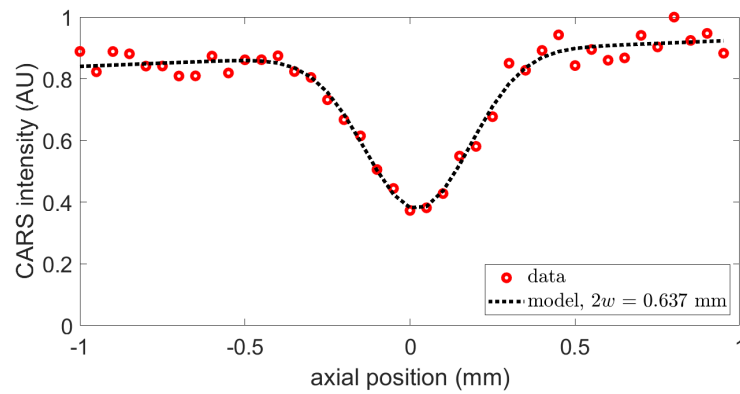
(a) Axial jet scan.
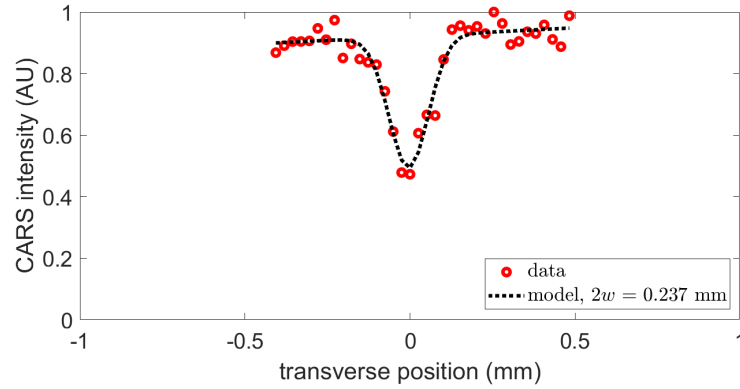
(b) Transverse jet scan.

Figure 5.16: Case B jet measurements.

Figure 5.17 displays Case B profile images for all three beams at the crossing position, as well as two-dimensional best-fit models for the three beams as described by Eq. (5.13). Beam profile figures for other cases can be found in Appendix B.3. Significant stretching of

the beam profiles due to astigmatism is evident.

(a) Beam profile images.

(b) Beam profile model.
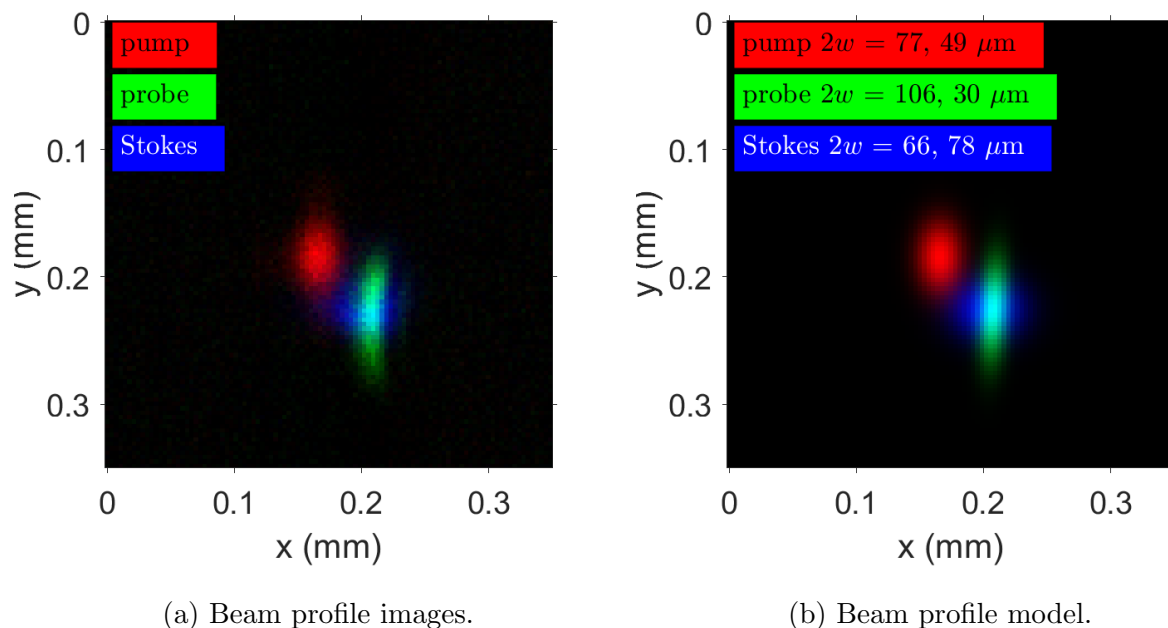
Figure 5.17: Case B beam profiles.

The width of the jet was deconvolved from the jet measurement to calculate the interrogation volume length for each case. Variations in the axial length of the interrogation volume and the acquired CARS signal strength for these cases are shown in Fig. 5.18. The CARS interrogation volume length increased linearly as lens focal length was increased from 200 to 300 mm. The increased volume of sampled gas enabled the use of higher pulse energies without incurring saturation effects; this also caused a linear increase in CARS signal intensity. However, the 150 mm lens (Case A) produced a longer interrogation volume than the 200 mm lens (Case B). The increased astigmatism experienced by the Case A beams (see Fig. B.17) likely limited the minimum focused spot size, therefore limiting the interrogation volume.
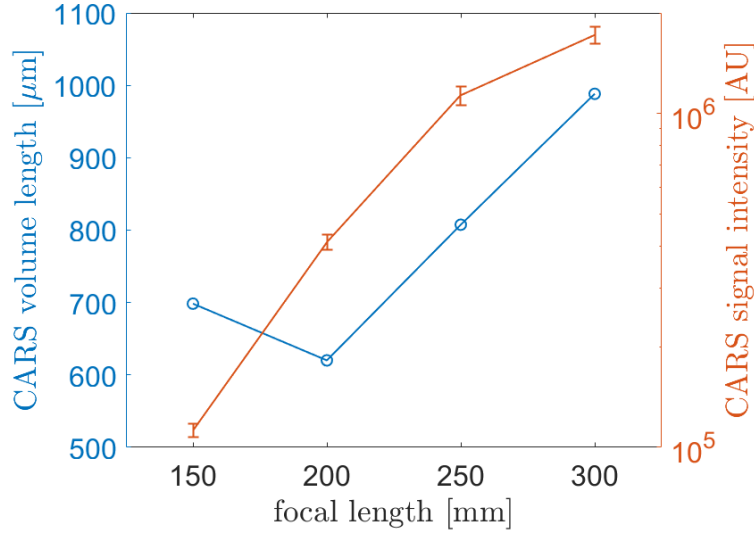
Figure 5.18: Effects of lens focal length on CARS production. $2w$ volume lengths are reported. Error bars encompass $\pm\sigma$.

5.4.5 Effects of beam crossing position

Another set of CARS configurations were tested in which the beams were focused by a single 200 mm lens and crossing position relative to beam foci z_c was varied. These cases are listed in Table 5.2. These include cases in which crossing occurred upstream of the foci ($z_c < 0$) and others in which crossing occurred downstream of the foci ($z_c > 0$). For each of these cases, the crossing angle was approximately 3.6°.

Table 5.2: Crossing position experiment cases. Lengths in [mm], energies in [μJ/pulse].

Case	z_c	U_{pump}	U_{probe}	U_{Stokes}	$2w_{pump}(z_c)$	$2w_{probe}(z_c)$	$2w_{Stokes}(z_c)$
B	-1.6	22	38	26	77, 49	106, 30	66, 78
E	-1	19	38	11	70, 51	83, 28	44, 51
F	0	9	38	10	56, 87	46, 57	31, 27
G	1	14	38	13	49, 118	32, 105	43, 57
H	1.5	16	38	18	49, 125	39, 124	64, 79
I	2.1	22	38	20	45, 150	51, 146	89, 105

An additional set of tests were performed in which pump, probe, and Stokes beams each passed through an individual lens of focal length 200 mm and diameter 25.8 mm. This individual-lens configuration, as shown in Fig. 5.19, has two principal benefits. First, because
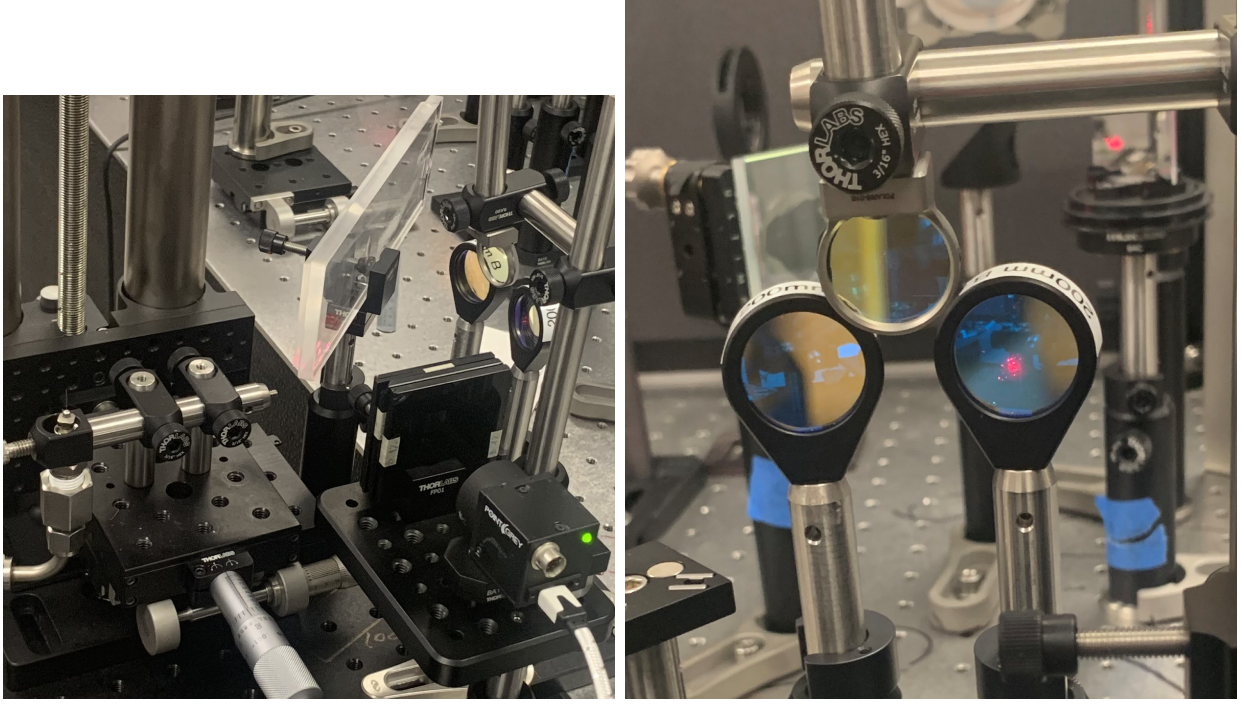
Figure 5.19: Individual-lens configuration with beam profile imaging setup.

each beam can be aligned to the axis of its own dedicated lens, astigmatism effects are minimized compared to the common-lens setup, which requires beams to enter the lens off-axis. Second, the three lenses can be moved relative to one another to enable greater crossing angles than can be achieved with a single 50.8 mm diameter lens. Individual-lens test cases are described in Table 5.3. z_c values reported here are measured relative to the average position of the foci of the beams; the beams focused in slightly different positions owing to the relative positions of their focusing lenses. These cases were conducted with lenses of focal length 200 mm at a crossing angle of about 6°. Axial jet measurements and beam profile images for a single case (Case L) are shown in Figs. 5.20 and 5.21.

Table 5.3: Individual-lens experiment cases. Lengths in [mm], energies in [μJ/pulse].

Case	z_c	U_{pump}	U_{probe}	U_{Stokes}	$2w_{pump}(z_c)$	$2w_{probe}(z_c)$	$2w_{Stokes}(z_c)$
J	-2.4	58	37	58	88, 138	101, 140	114, 143
K	-1.6	27	37	29	77, 66	66, 96	64, 90
L	0.05	5	37	6	72, 43	38, 31	25, 36
M	0.5	5	37	6	45, 45	52, 40	22, 27
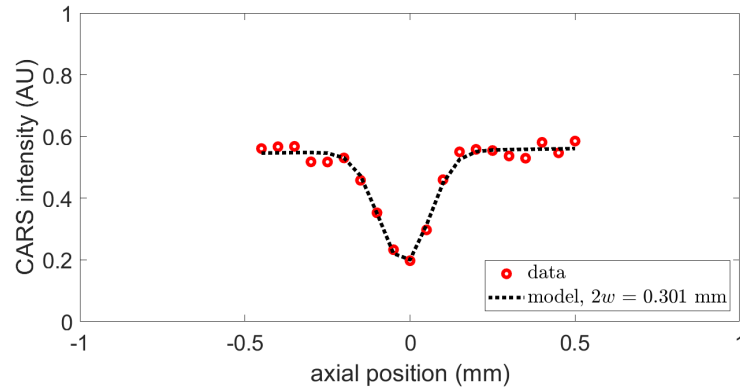
Figure 5.20: Case L, axial jet scan.

(a) Beam profile images.

(b) Beam profile model.
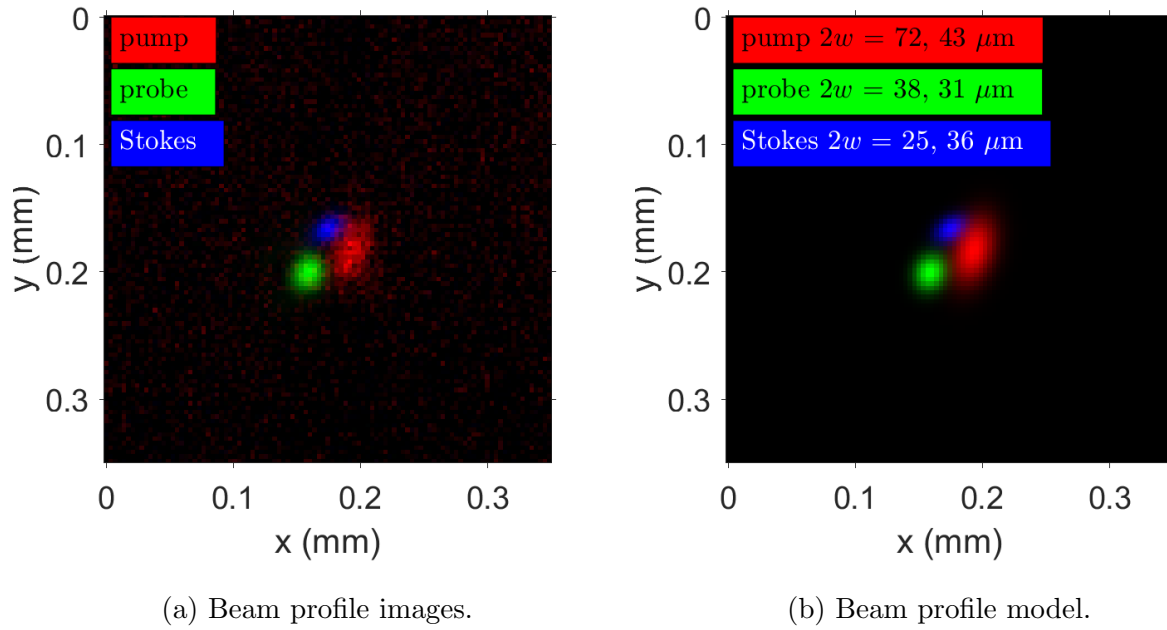
Figure 5.21: Case L beam profiles.

For both common-lens and individual-lens setups, CARS signal intensities and interrogation volume widths are shown as a function of crossing position in Fig. 5.22. Both crossing position and lens setup had significant effects on CARS generation. For both setups, minimum interrogation volume widths and minimum CARS signal generation occured when beams were crossed close to the foci. As the beam crossing was moved away from the foci, CARS signal generation was increased by about an order of magnitude, as the interrogation volume also widened. The common-lens setup produced a minimum interrogation volume of
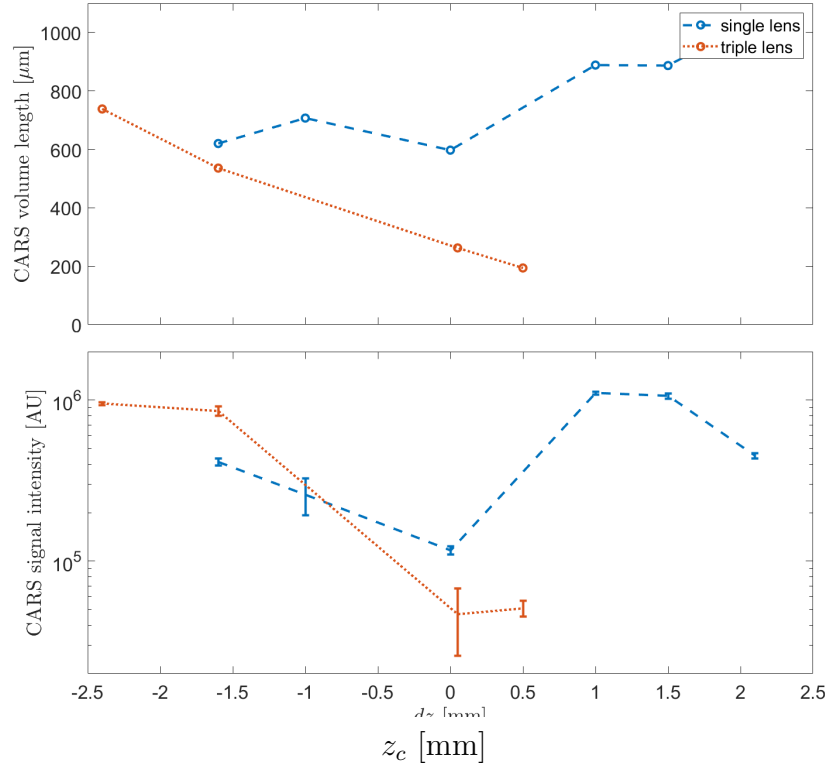
Figure 5.22: Effects of beam crossing configuration on CARS production. $2w$ volume lengths are reported. Error bars encompass $\pm\sigma$.

length 600 μm. This was reduced to 200 μm for the individual-lens setup due to the increased crossing angle and decreased astigmatism effects.

Transverse-direction volume width varied between jet cases. For most cases (A–G, J–M), calculated volume widths were smaller than 200 μm. In some transverse scans of the jet (A, C, M), the region of reduced CARS signal was approximately as wide as the jet itself, indicating a width too small to be resolved using this method. In common-lens cases in which the beams were significantly expanded at crossing (H, I), volume widths of 300–350 μm were observed.

The 200 μm axial interrogation volume length is significantly smaller than lengths reported for other CARS experiments with similar BOXCARS crossing configurations. This can be attributed to the increased crossing angle $\alpha = 6°$ and very small Stokes beam diameter at crossing $d \approx 25 - 27$ μm. The interrogation volume length as determined by the jet

measurement is somewhat smaller than $d/\sin\alpha \approx 210 - 260$ μm. Smaller interrogation volume lengths have been achieved using very large crossing angles [70, 140, 57]. This work is compared with reference cases in Table 5.4.

Table 5.4: Comparison of interrogation volume lengths. Unknown values are marked by "–". $1/e^2$ volume lengths are reported, where possible; some sources do not specify the standard by which volume lengths are measured.

Type	lens	α	Volume length	Source
fs/ps vib./rot.	150 mm	–	1.1 mm (nonresonant jet)	[51, 125]
ns vib./rot	600 mm, 750 mm	2.1°, 1.9°	1 mm (estimated)	[64]
ns rot.	300 mm	2.2°	1.3 mm (glass coverslip)	[63]
ns rot.	300 mm	1.1°	1–2 mm (estimated)	[141]
fs/ps rot. 1D	300 mm cyl.	6°	600 μm (glass coverslip)	[58]
ps rot. 1D	300 mm cyl.	–	1.9 mm (glass coverslip)	[142]
fs/ps vib.	200 mm × 3	6°	200 μm (nonresonant jet)	This work
ns rot. 1D	–	90°	100 μm (nonresonant jet)	[70]
fs/ps rot. 1D	750 mm	33°	155 μm (estimated)	[140]
fs/ps rot. 1D	300 mm	33°	65 μm (estimated)	[57]

5.4.6 Dual-pump CARS characterization

Rotational and vibrational CARS were performed simultaneously, using a common combining lens of focal length 200 mm and diameter 50.4 mm. CARS measurements were performed for three different cases, each with slightly different beam positions, as detailed in Table 5.5. An example rotational CARS spectrum is provided in Fig. B.33. Example axial scans for two different cases (N and O) are shown in Fig. 5.23. In Case N, vibrational and rotational CARS interrogation volumes were significantly offset from one another. In Case O, a special effort was made to improve the overlap between the two volumes; however, the vibrational CARS interrogation volume was significantly widened in the process from 570 to 640 μm. This verification is necessary to confirm the co-location of simultaneous vibrational and rotational CARS measurements.

Table 5.5: Dual-pump experiment cases. Lengths in [mm], energies in [μJ/pulse].

Case	z_c	$U_{\text{pump,v}}$	$U_{\text{pump,r}}$	U_{probe}	U_{Stokes}
N	1.1	12	37	38	35
O	1.1	11.7	35	38	31.5
P	1.9	10	52	38	47

Case	$2w_{\text{pump,v}}(z_c)$	$2w_{\text{pump,r}}(z_c)$	$2w_{\text{probe}}(z_c)$	$2w_{\text{Stokes}}(z_c)$
N	62, 51	123, 36	94, 28	50, 57
O	70, 58	48, 53	101, 29	50, 54
P	76, 52	149, 56	134, 37	86, 96
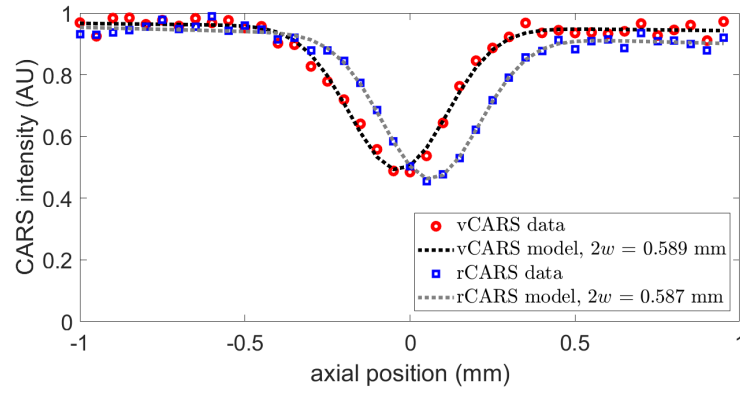
(a) Case N.
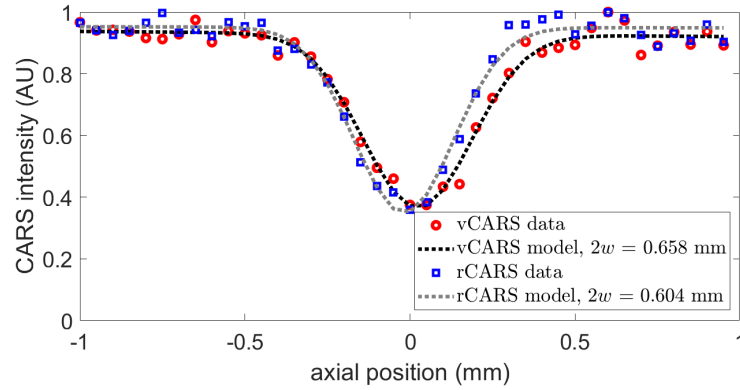
(b) Case O.

Figure 5.23: Dual-pump axial jet scans.

5.4.7   Comparison with glass coverslip translation method

The more commonly-used method of CARS resolution characterization – the translation of a glass coverslip through the interrogation volume – was also executed. Fig. 5.24 is an
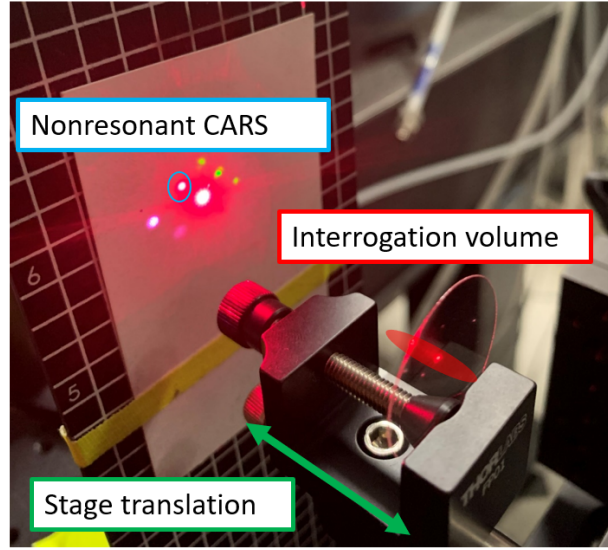
Figure 5.24: CARS signal generation in glass.

annotated image of nonresonant CARS signal being generated in glass. CARS signal is the topmost spot that appears red/white in color. The other three red/white spots are the input beams, and the yellow/green spots are created by other mixing processes. CARS signal was measured by the spectrometer as the coverslip was translated to several different positions along the axial direction.

This test was performed with vibrational CARS in the individual-lens configuration with a crossing angle of 6°. All three beams were significantly attenuated; this was necessary to avoid burning the coverslip. The test was repeated four times with different sets of beam energies; the four cases are listed in Table 5.6.

Table 5.6: Glass coverslip experiment cases, energies in [µJ/pulse]. In cases Q and S, the Stokes pulse energy was below the detection limit for the power meter.

Case	U_{pump}	U_{probe}	U_{Stokes}
Q	10	5	< 0.5
R	2	4.5	1.5
S	2	3.2	< 0.5
T	2	3.3	4.5

CARS signal intensity as a function of coverslip position for each case is displayed in Fig. 5.25. The glass coverslip scattered some light from the pump beam into the spectrometer at
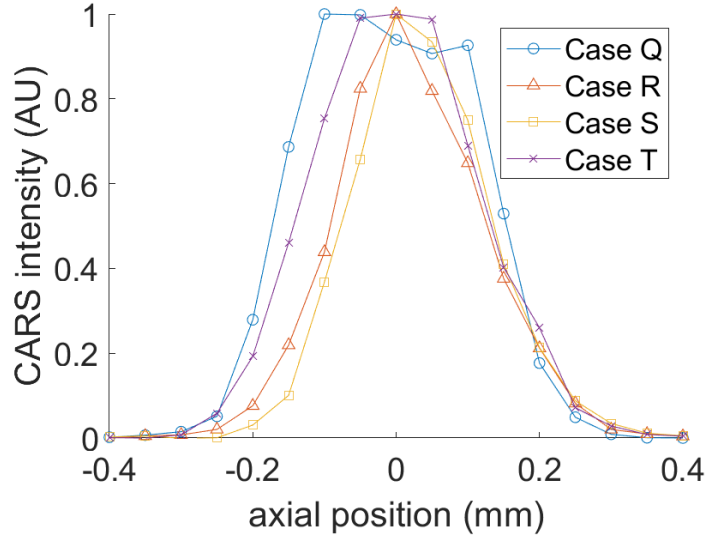
Figure 5.25: CARS signal intensity as a function of glass coverslip position.

some positions of the coverslip. To correct for this, background spectra (with the probe beam blocked) were acquired at each coverslip position and these were subtracted from CARS spectra. Input beam energies had a significant effect on the distance over which CARS signal was observed. Higher input beam energies tend to produce wider distributions. The distributions in high-energy cases also have non-Gaussian, flat tops, suggesting the CARS transition in glass becomes saturated.

5.5   Interrogation volume modeling

The size and shape of the CARS interrogation volume was modeled by representing the pump, probe, and Stokes beams as idealized Gaussian beams propagating along different vectors in a three-dimensional space. Though beam profile images demonstrate that the beams deviate from ideal Gaussian behavior, this model provides a useful approximation. CARS signal irradiance that is produced at any spatial location is proportional to the square of the magnitude of the product of the local electric field strengths of the three beams [25]:

$$I_{\mathrm{CARS}} \propto |E_{\mathrm{CARS}}|^2 \propto |E_{\mathrm{pump}} E_{\mathrm{probe}} E_{\mathrm{Stokes}}|^2 \tag{5.14}$$

For a Gaussian beam, each of these electric field strengths was modeled as a function of axial distance z from the beam waist and radial distance r from the beam axis [143, 144]:

$$E\left(r, z\right) = E_0 \frac{w_0}{w\left(z\right)} \exp\left[\frac{-r^2}{w\left(z\right)^2}\right] \exp\left\{-i\left[kz + \frac{kr^2}{2R\left(z\right)}\right]\right\} \exp\left[i\psi\left(z\right)\right] \tag{5.15}$$

The origin $\left(z = 0, \ r = 0\right)$ is the location along the beam axis at which the beam is most tightly focused. E_0 is the electric field strength at the beam focus, related to the impedance of the medium through which the beam moves η, the measured beam power P_0, and the beam waist radius w_0:

$$E_0 = 2\sqrt{\frac{\eta P_0}{\pi w_0^2}} \tag{5.16}$$

The wavenumber k of the beam depends on the wavelength λ of the beam and the local index of refraction n:

$$k = \frac{2\pi n}{\lambda} \tag{5.17}$$

The beam width $w\left(z\right)$ is a function of w_0 and the Rayleigh range z_R:

$$w\left(z\right) = w_0\sqrt{1 + \left(\frac{z}{z_R}\right)^2} \tag{5.18}$$

$$z_R = \frac{\pi w_0^2 n}{\lambda} \tag{5.19}$$

Finally, the phase of the beam is influenced by the radius of curvature $R\left(z\right)$ of the beam's wavefronts and the Gouy phase shift $\psi\left(z\right)$:

$$R\left(z\right) = z\left[1 + \left(\frac{z_R}{z}\right)^2\right] \tag{5.20}$$

$$\psi\left(z\right) = \tan^{-1}\left(\frac{z}{z_R}\right) \tag{5.21}$$

This model was used to approximate the size of the interrogation volumes in Cases L and K. The $\hat{\mathbf{x}}$-axes of each of the three beams is inclined to the global z-axis by the measured crossing angles. Beam profile images were used to set the distance from the crossing position to each beam focus individually. Measured beam energies, pulse durations, and beam waists (as measured by the beam profiling camera) were used as inputs. The model does not account for astigmatism, therefore beam cross-sections are always circular. Fig. 5.26 shows the Case L $1/e^2$-surface for each of the three beams. In this and subsequent figures, the origin corresponds to the crossing position. This should not be confused with the focus-centered origin of Eqs. (5.15) - (5.21) used to calculate each beam. Fig. 5.27 shows the Case L $1/e^2$-surface for $|E_{\text{pump}}E_{\text{probe}}E_{\text{Stokes}}|^2$; this is a representation of the extent of the CARS interrogation volume. Figs. 5.28 and 5.29 present the same information for Case K. The Case L modeled volume length agrees very well with the value calculated from a jet scan. However, the Case K modeled volume length underpredicts the jet scan length by about 30%. Nonetheless, this model could be a useful tool for estimating the volume size without performing jet measurements, or for planning new experimental setups.
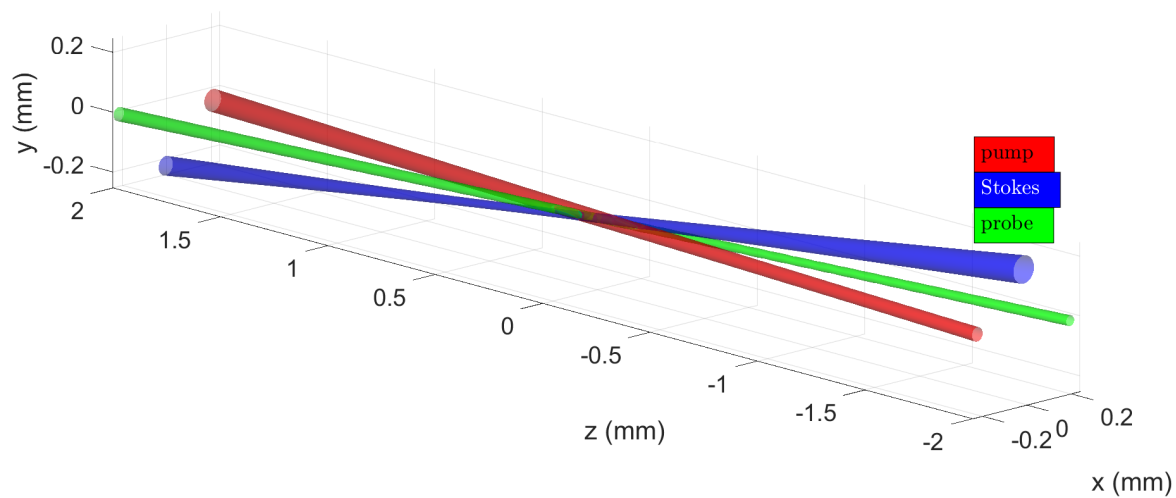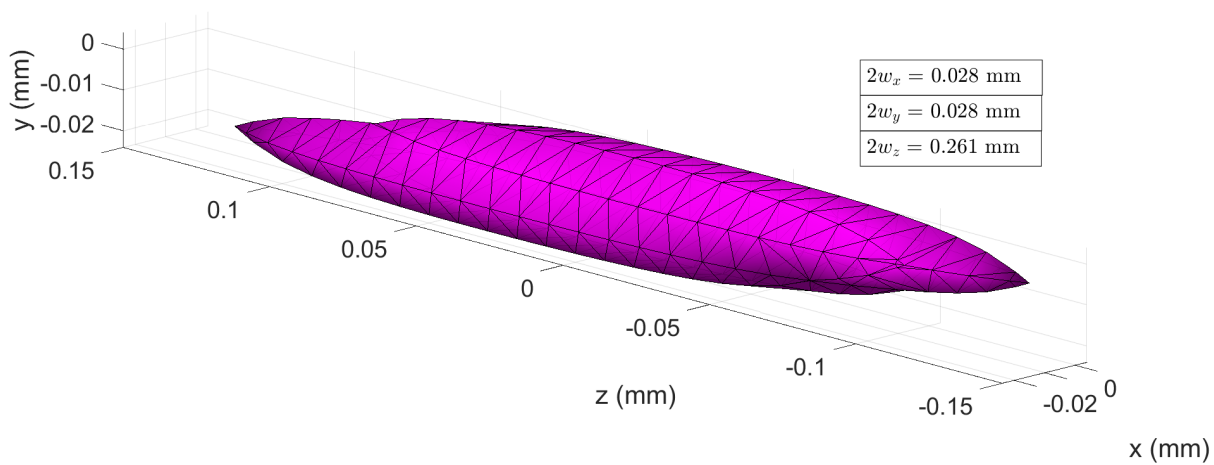
Figure 5.26: Case L beam crossing model.

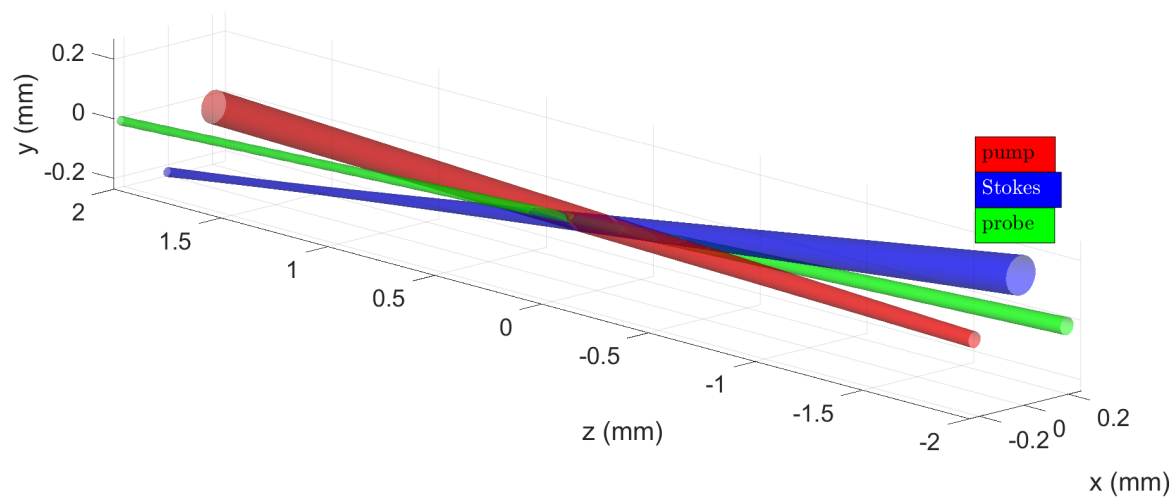Figure 5.27: Case L interrogation volume model.

Figure 5.28: Case K beam crossing model.
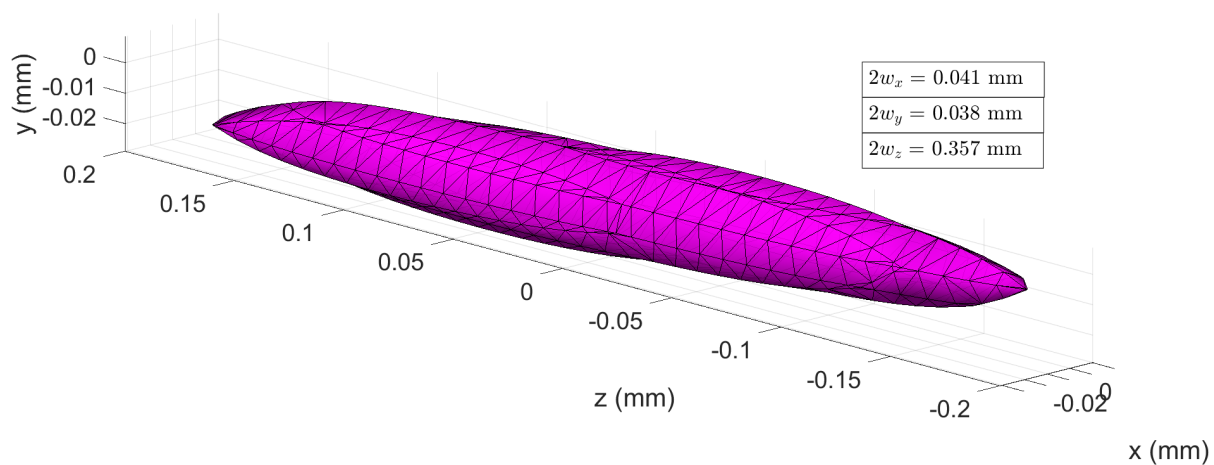
Figure 5.29: Case K interrogation volume model.

5.6 Summary

This chapter described the construction and characterization of a new hybrid fs/ps CARS system at the University of Virginia. CARS signal was generated using several different focusing lenses, beam crossing angles, and beam crossing positions relative to beam foci. The spatial resolution of each of these cases was characterized using a micro-scale jet of nonresonant gas. As beams are crossed further from their foci, or as the beam crossing angle is decreased, CARS signal level and the length of the interrogation volume both increase. Switching from a single focusing lens to a dedicated lens each for pump, probe, and Stokes significantly reduces the astigmatism effects present at the beam crossing and produces a smaller interrogation volume. The smallest observed interrogation volume was about 200 μm long. This represents a significant increase in spatial resolution relative to other published experiments with similar BOXCARS crossing angles. The reduced interrogation volume size will be used to minimize spatial averaging effects in future experiments in combustion environments with temperature gradients over small length scales.

The size of the interrogation volume was also measured using the traditionally-employed glass coverslip method. This method is flawed; the attenuation of the beams required for this method was shown to alter the measured length of the volume. As the jet measurement method does not require beam attenuation, it provides a more-accurate volume measurement. Additionally, a MATLAB model was constructed to simulate the interrogation volume size at different beam crossing conditions, using input data from beam profile images. This model was able to approximate the size of the interrogation volume for two different beam crossing configurations, and could be used in the future for designing new experiments which balance spatial resolution requirements with experimental geometry constraints.

Conclusions

Summary

Laser diagnostic techniques such as PLIF and CARS are vital tools for investigating flame structure and behavior under compressible, turbulent conditions. This dissertation focused on improving the spatial resolution of these measurement techniques, characterizing that resolution, and employing these high-spatial-resolution measurements to improve understanding of premixed cavity-stabilized scramjet flames.

An OH-PLIF system was built using a spatial filter to minimize light sheet thickness and optimize imaging resolution; the maximum spatial resolution of this system was $40 \times 40 \times 25$ μm. This system was used to image two different premixed turbulent flames at the U.Va. scramjet facility, stabilized on cavity flameholders characterized by different cavity heights. These measurements exceed the spatial resolution of other ducted flow PLIF measurements reported in the literature.

OH-PLIF measurements presented here include the first measurements made of a new additively-manufactured cavity flameholder of height $H = 3$ mm. This new combustor provided a smaller domain of interest relative to previously-studied combustors such that it was feasible to simulate using DNS. OH-PLIF measurements were collected both for this small-scale cavity and for a large-scale cavity of height $H = 9$ mm. Both cavities produce regions in which combustion products recirculate; the flames are controlled by turbulent mixing in a shear layer between the recirculation region and the incoming flow of premixed

reactants. The two flames are similar in structure and spread into the main duct flow at similar angles. At the aft end of the small-scale cavity, the flame became stretched, reducing OH production; this behavior is not observed in the large-scale cavity experiment, where local strain rates are smaller in magnitude.

For the small-scale cavity, experimental OH-PLIF images and simulated OH-PLIF images generated from a DNS investigation were binarized based on the location of high OH signal gradient. DNS results showed that the position of the flame front as identified by this method agreed well with regions of heat release. Flame intermittency and flame front curvature were calculated; DNS values were in moderate agreement with experimental results. Discrepancies observed in DNS relative to the experiment may be caused by a reduced inflow Mach number or inaccurate wall temperature boundary conditions. Methods provided here for image binarization and processing can be used to evaluate future simulation outputs for fidelity to experimental results.

A hybrid fs/ps CARS system was also constructed; a micro-scale jet of spectrally nonresonant gas was used to measure the size of the interrogation volume produced with several different focusing lenses and beam crossing conditions. The micro-scale jet method of resolution measurement was demonstrated as an improvement upon the widely-used method involving nonresonant CARS signal generated in a thin glass coverslip. A measurement volume 200 μm in length was produced using dedicated focusing lenses for each beam and a folded BOXCARS phase-matching configuration with a crossing angle of 6°. The spatial resolution of this system significantly exceeds that of experiments with similar crossing angles. This system will be used in for future temperature and species measurements in the U.Va. scramjet facility.

Recommendations for future work

In the small-cavity scramjet experiments, inflow turbulence and boundary layer thickness were controlled by the inlet/isolator shock train. One key control of the present experiments, within narrow limits [145], was the shock train location, which could be changed by varying the fuel-air equivalence ratio and air-throttle flow rate [10]. Future experiments could carefully modify the shock train location relative to the cavity in order to explore the effects of varying turbulence and boundary layer profile on flame structure. Alternatively, future experiments could insert a wire grid in the isolator, artificially changing turbulence levels and scales, to observe the effect on flame structure. High-resolution velocimetry measurements would be necessary at any new inflow condition to quantify the new turbulence level and boundary layer profile. Careful parametric variation of flow conditions would determine the dependence of flame structure on inflow turbulence, heat release, and flow compressibility effects.

While the comparison between DNS outputs and experimental results showed moderate agreement in flame structures, future DNS work could address small discrepancies in flame front curvature and large discrepancies in flame intermittency. This may be accomplished by raising the Mach number of the simulation to match experiments. The apparent absence in the DNS output of OH recombination in certain regions near the combustor wall suggests a possible discrepancy in wall temperature boundary conditions between simulation and experiment. Experimental measurement of wall temperatures would be useful for future simulation and design efforts. This could potentially be accomplished using a thermographic phosphor [146, 147, 148] or through near-surface CARS thermometry measurements of the gas.

Algorithms for calculating flame front curvature and flame surface density could be extended to three dimensions for DNS output processing. 3-D flame front metrics from DNS could be compared with their 2-D counterparts from DNS and from PLIF to determine the effects of anisotropy on flame structure.

The CARS system developed and characterized in this work is now suitable for testing

a combustion environment such as a counterflow burner in which small-scale temperature and species structures can be resolved (see Appendix A for preliminary experiment setup information). Scans of CARS measurements across these structures can be deconvolved with the expected interrogation volume size. The result of the deconvolution can be compared with chemical-kinetic simulations of these scans; agreement between experiments and simulations would further support resolution measurements presented here.

The CARS system could in the future be used to study the U.Va. scramjet facility. Temperature and species measurements in that environment would provide new information about the flow over the aft ramp of the small-scale cavity. If the reduction in OH-PLIF signal in that region is accompanied by a reduction in temperature, this would further suggest that high strain rates in that region are reducing chemical reaction rates. Lieber [83] suggested that the ejection of products at the aft ramp of the cavity may be controlled by thermoacoustic oscillations on the order of 100 Hz between the flame front and the thermal throat of the facility; kHz-rate CARS measurements may be able to resolve the effects of these oscillations in time.

Appendices

A   Counterflow burner experiment

The University of Virginia Reacting Flow Laboratory counterflow burner produces opposing jets of fuel and oxidizer using co-annular nozzles. An inert gas such as N_2 or H_2 flows through the annulus of each jet, shielding the fuel and oxidizer in the inner flow. The jets are contained within a pressure chamber with a maximum operating pressure of 50 atm with optical access through fused silica windows on four sides. Each jet is 6.5 mm in diameter. The distance between nozzles is variable but has been set at 5.45 mm for the current investigation. A schematic of the burner is shown in Fig. A.1. The burner has been run at pressures up to 30 atm. Inert gas dilution of fuel and oxidizer is necessary to maintain a laminar flame. N_2 suffices for pressures less than 8 atm; H_2 is used at greater pressures. A full description of the burner can be found in [133, 129].
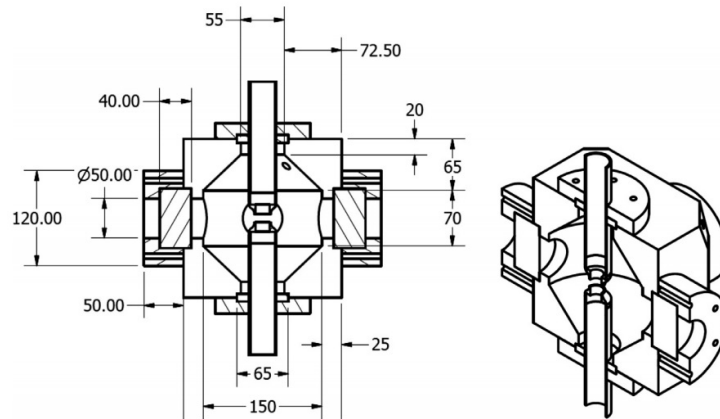
Figure A.1: UVa counterflow burner schematic with dimensions in mm, from [133].

In order to set up the CARS experiment at the counterflow burner, optics required for final beam positioning and focusing, as well as optics required to split Stokes and rotational pump beams, were moved off of the laser optical table and onto a breadboard. This breadboard was mounted on a system of translation stages that enabled the movement of the CARS interrogation volume in three dimensions. Figure A.2 shows the system of mirrors used to route the beams through the translation system. The beams propagated for approximately 5 m between the laser table and the breadboard. Figure A.3 shows the breadboard optics, including the three final focusing lenses of focal length 200 mm.
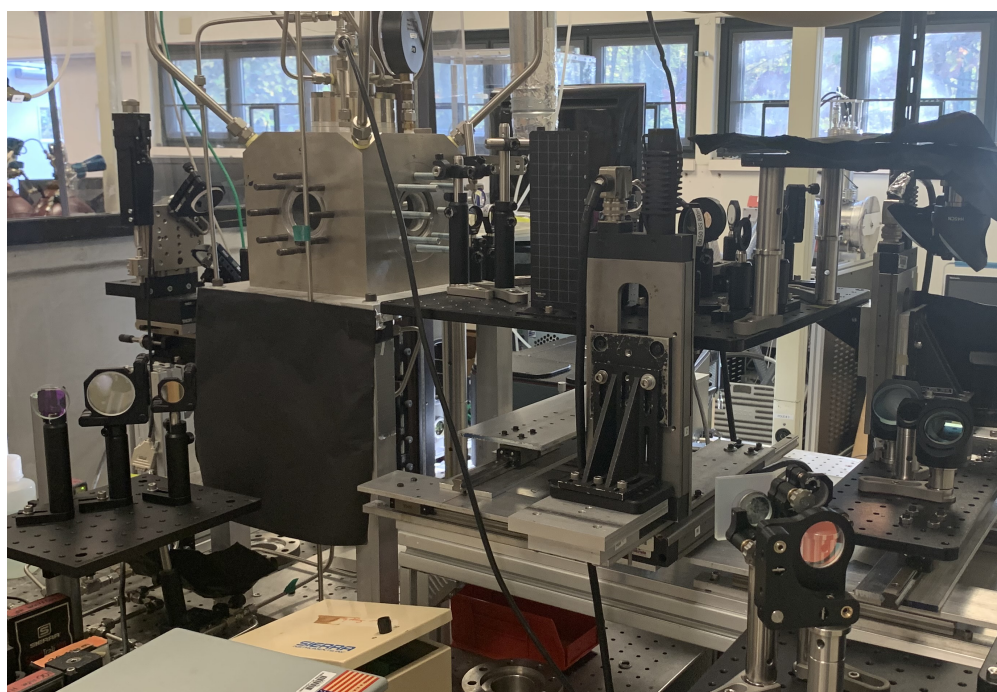
Figure A.2: Three-axis translation system beam path for counterflow burner CARS experiment.

Figure A.4 shows optics for CARS signal collection, on a separate motorized stage system, routing the signal into the spectrometer. Also pictured here is an apparatus holding a very small sliver of glass between the two nozzles of the counterflow burner. Nonresonant CARS signal generated in the glass sliver is used to verify beam overlap in space and in time; this signal is then coupled into the spectrometer.

Figure A.3: Injection optics for counterflow burner CARS experiment.

A beam splitter and beam profiling camera were set up on the breadboard, and beam profile images were acquired with the translation system in multiple different positions, in order to test the alignment of the beams with the translation stages. Fig. A.5 shows beam profiles near the crossing position as horizontal and vertical stages are translated throughout the experimental domain (± 3 mm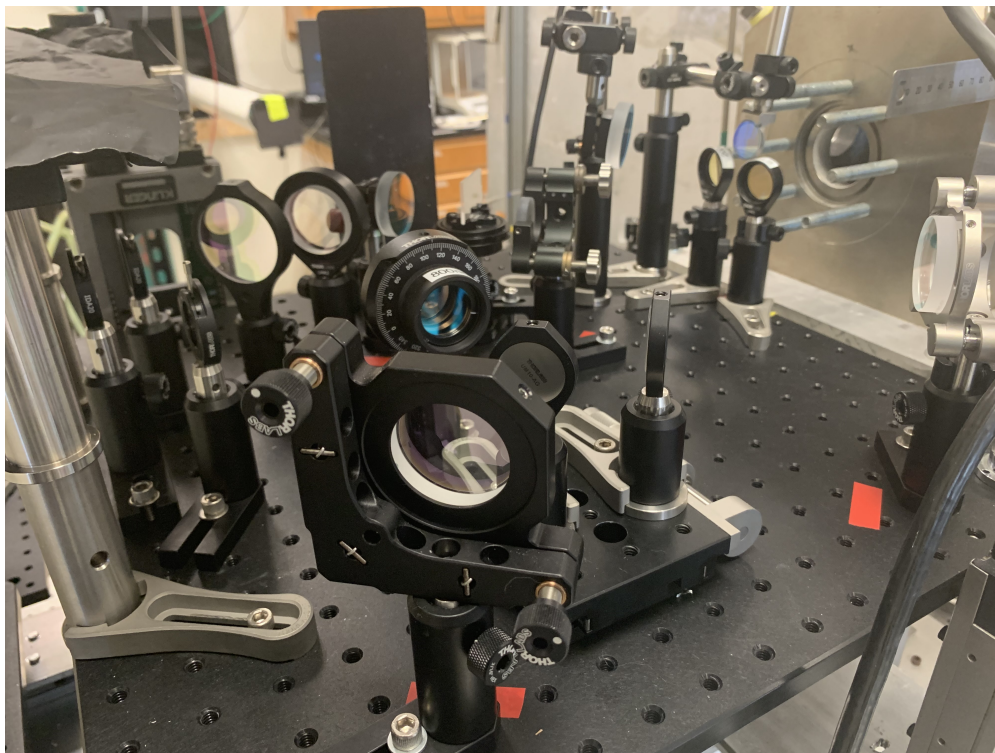). The images show that beams drift approximately 50 µm, all in the same direction, as the stages move. Fig. A.6 shows the movement of the probe profile image as the probe delay stage is moved throughout its range; a similar ~ 50 µm beam drift is observed. Therefore, the beams will remain aligned with each other (and produce CARS signal) throughout the domain of the counterflow experiment. The relative position of the CARS interrogation volume is known within ± 50 µm as the volume is moved to different regions of the flame.

Limits are imposed on the vertical travel of the CARS interrogation volume by the counterflow burner nozzles. Either the incoming Stokes beam (angled downwards) or the outgoing CARS signal (angled upwards) is blocked by the nozzle at each limit. With the
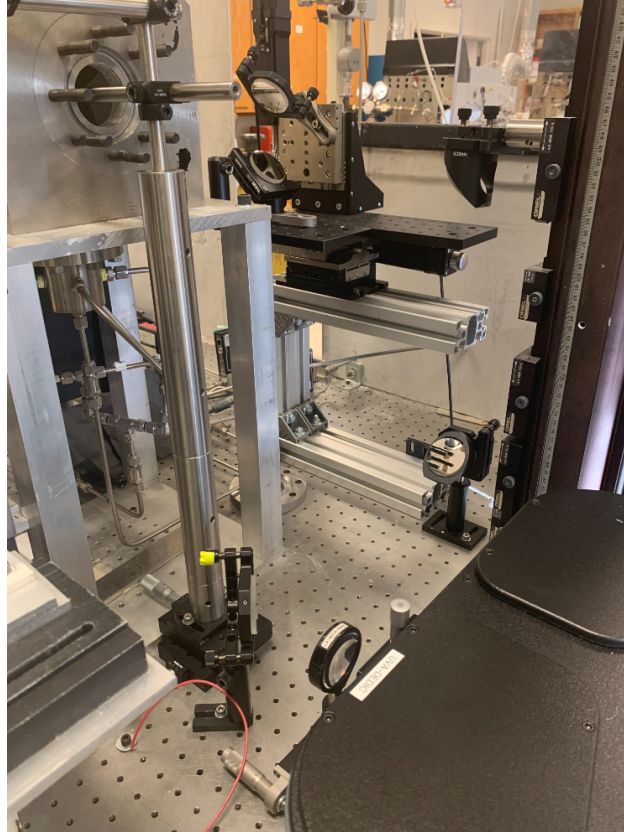
Figure A.4: Detection optics for counterflow burner CARS experiment.

(a) Horizontal stage scan.

(b) Vertical stage scan.
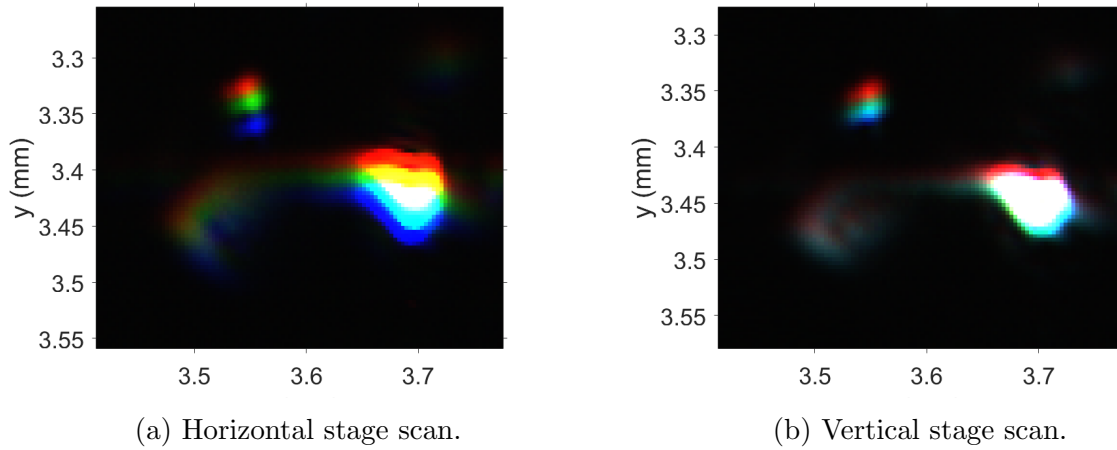
Figure A.5: Beam profile image sets. Green: interrogation volume centered in burner. Red/blue: stages moved ± 3 mm off-center.

current beam crossing configuration, the vertical distance over which the Stokes beam is unobstructed is 5.1 µm; this is an estimate of the vertical size of the experimental domain that can be investigated with the CARS system.

Figure A.6: Probe beam profile images, colored by probe delay. Red: -210 ps. Green: 0 ps. Blue: $+130$ ps.

B   Supplementary tables and figures

B.1   Tables for simulated PLIF calculation

The following tables are used in Section 4.3.1 to calculate simulated OH LIF values for DNS results.

Table B.1: DNS species list with molecular weights [kg/mol]

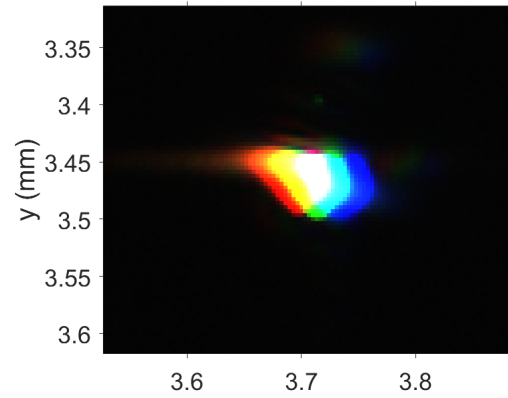| Species	W
H_2	$2.015 \cdot 10^{-3}$
H	$1.008 \cdot 10^{-3}$
O	$1.600 \cdot 10^{-2}$
O_2	$3.120 \cdot 10^{-2}$
OH	$1.701 \cdot 10^{-2}$
H_2O	$1.802 \cdot 10^{-2}$
HO_2	$3.301 \cdot 10^{-2}$
H_2O_2	$3.401 \cdot 10^{-2}$
CH_3	$1.504 \cdot 10^{-2}$
CH_4	$1.604 \cdot 10^{-2}$
CO	$2.801 \cdot 10^{-2}$
CO_2	$4.401 \cdot 10^{-2}$
CH_2O	$3.003 \cdot 10^{-2}$
C_2H_2	$2.604 \cdot 10^{-2}$
C_2H_4	$2.805 \cdot 10^{-2}$
C_2H_6	$3.007 \cdot 10^{-2}$
HCCO	$4.103 \cdot 10^{-2}$
CH_2CO	$4.204 \cdot 10^{-2}$
CH_3CHO	$4.405 \cdot 10^{-2}$
aC_3H_5	$4.107 \cdot 10^{-2}$
C_3H_6	$4.208 \cdot 10^{-2}$
N_2	$2.801 \cdot 10^{-2}$

Table B.2: OH $X^2\Pi$ vibrational term energies (cm^{-1}), from Bernath and Colin [117].

v	G_v
0	0.0
1	3570.35
2	6975.09
3	10216.1
4	13294.6
5	16210.6
6	18963.0

Table B.3: OH $X^2\Pi$ $(v'' = 0)$ rotational term energies (cm^{-1}), from Bernath and Colin [117].

J	F_{1e}	F_{1f}	F_{2e}	F_{2f}
0.5	N/A	N/A	126.292	126.450
1.5	0.0000	0.0556	187.493	187.753
2.5	83.723	83.925	288.772	289.044
3.5	201.931	202.380	429.279	429.462
4.5	355.120	335.915	608.198	608.194
5.5	543.596	544.829	824.816	824.531
6.5	767.482	769.240	1078.51	1077.86
7.5	1026.76	1029.12	1368.72	1367.62
8.5	1321.28	1324.32	1694.90	1693.29
9.5	1650.81	1654.60	2056.55	2054.34
10.5	2015.05	2019.65	2453.11	2450.25
11.5	2413.61	2419.09	2884.06	2880.49
12.5	2846.08	2852.48	3348.81	3344.47
13.5	3311.95	3319.33	3846.77	3841.61
14.5	3810.71	3819.12	4377.31	4371.28
15.5	4341.78	4351.26	4939.77	4932.84
16.5	4904.54	4915.13	5533.47	5525.59
17.5	5498.35	5510.08	6157.70	6148.83
18.5	6122.52	6135.41	6811.69	6801.82
19.5	6776.32	6790.40	7494.69	7483.78
20.5	7458.99	7474.29	8205.88	8193.92
21.5	8169.77	8186.29	8944.43	8931.41
22.5	8907.82	8925.57	9709.49	9695.39
23.5	9672.30	9691.29	10500.17	10484.99
24.5	10462.36	10482.58	11315.57	11299.32
25.5	11277.08	11298.53	12154.77	12137.44
26.5	12115.57	12138.23	13016.81	12998.42
27.5	12976.87	13000.73	13900.72	13881.29
28.5	13860.03	13885.06	14805.52	14785.06
29.5	14764.07	14790.25	15730.20	15708.74
30.5	15688.00	15715.28	16673.74	16651.32

B.2   CARS interrogation volume measurements

The following figures present measurements of different interrogation volumes described in Chapter 5 using a micro-scale jet.

(a) Axial jet scan.   (b) Transverse jet scan.
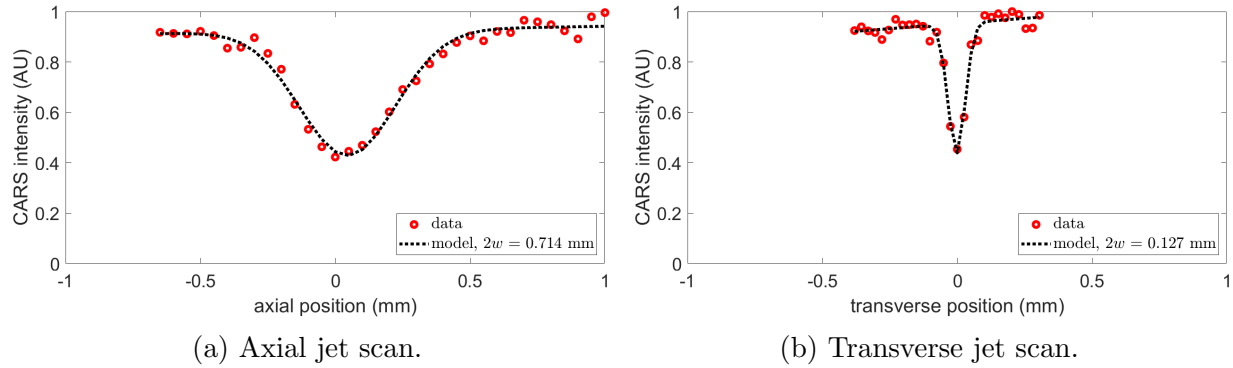
Figure B.1: Case A jet measurements.

(a) Axial jet scan.   (b) Transverse jet scan.
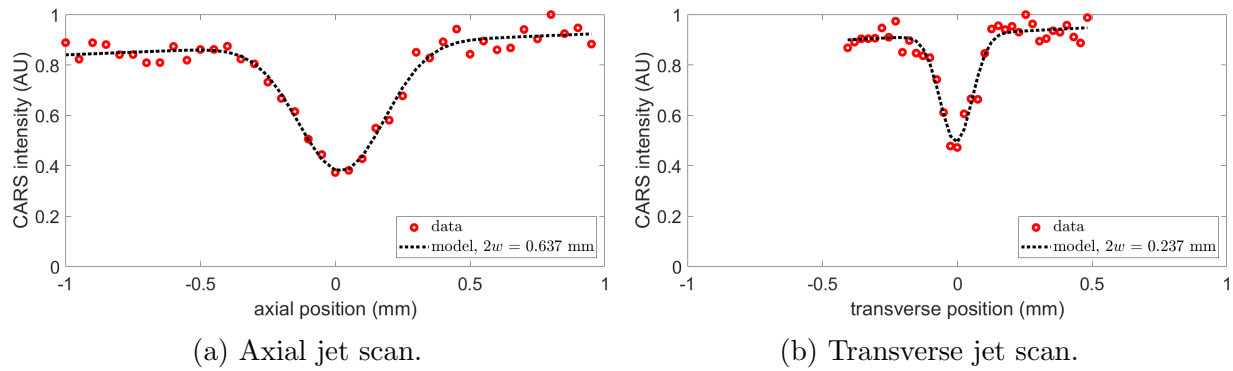
Figure B.2: Case B jet measurements.

(a) Axial jet scan.   (b) Transverse jet scan.
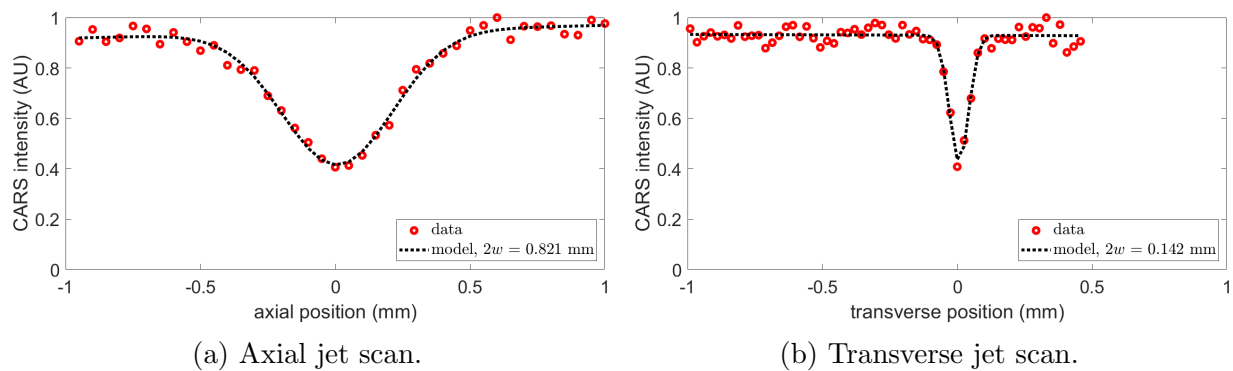
Figure B.3: Case C jet measurements.

(a) Axial jet scan.

(b) Transverse jet scan.
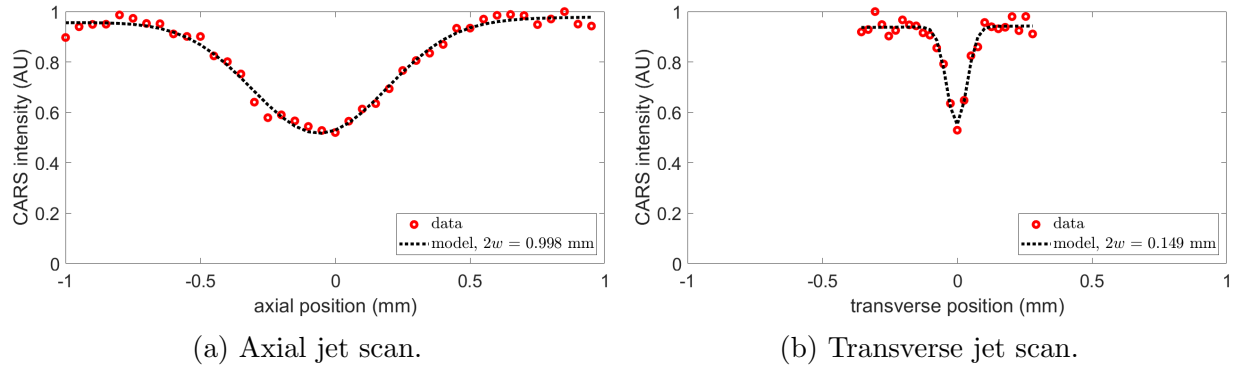
Figure B.4: Case D jet measurements.

(a) Axial jet scan.

(b) Transverse jet scan.
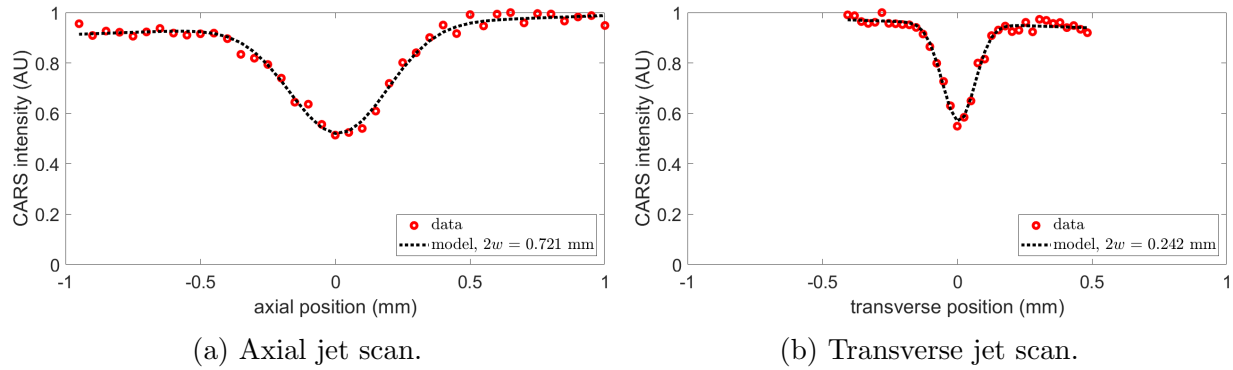
Figure B.5: Case E jet measurements.

(a) Axial jet scan.

(b) Transverse jet scan.

Figure B.6: Case F jet measurements.

(a) Axial jet scan.

(b) Transverse jet scan.

Figure B.7: Case G jet measurements.
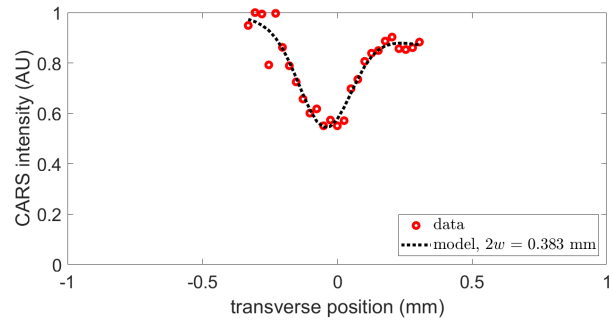
(a) Axial jet scan.

(b) Transverse jet scan.

Figure B.8: Case H jet measurements.
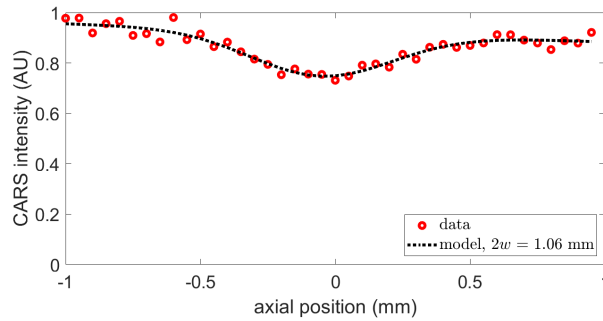
(a) Axial jet scan.
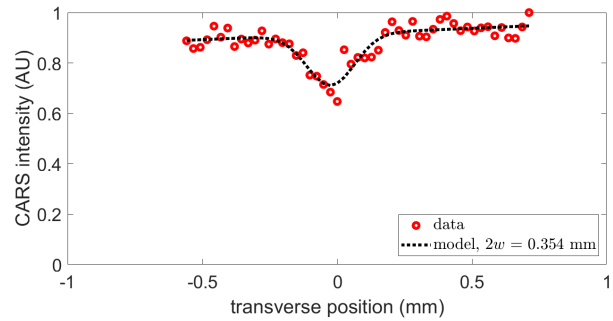
(b) Transverse jet scan.

Figure B.9: Case I jet measurements.

(a) Axial jet scan.

(b) Transverse jet scan.
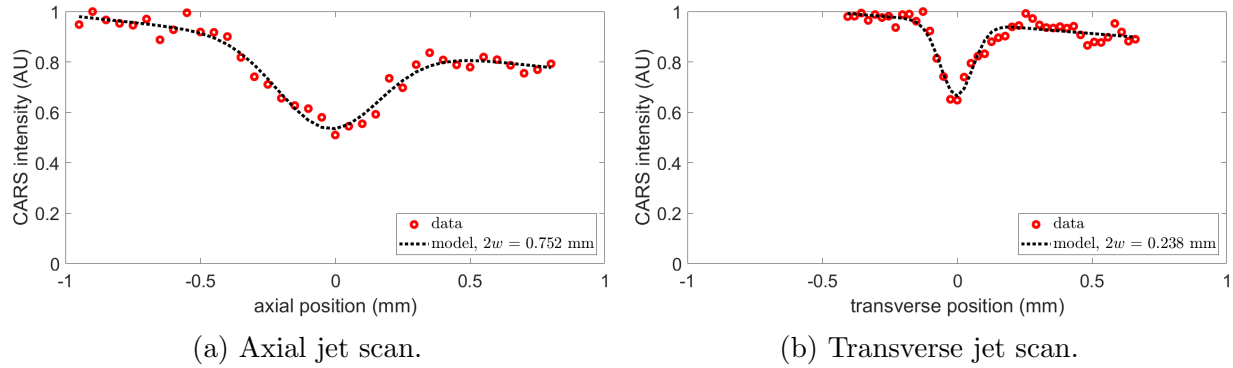
Figure B.10: Case J jet measurements.

(a) Axial jet scan.

(b) Transverse jet scan.
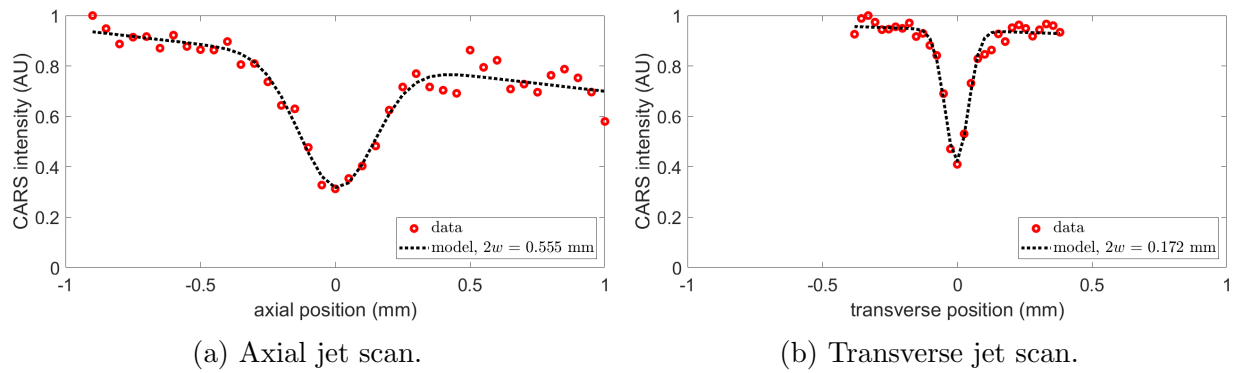
Figure B.11: Case K jet measurements.

(a) Axial jet scan.

(b) Transverse jet scan.
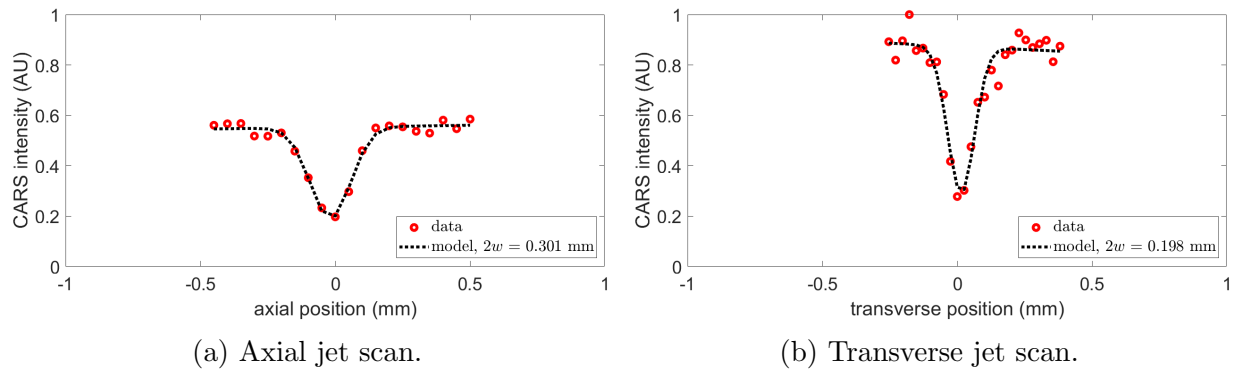
Figure B.12: Case L jet measurements.

(a) Axial jet scan.

(b) Transverse jet scan.
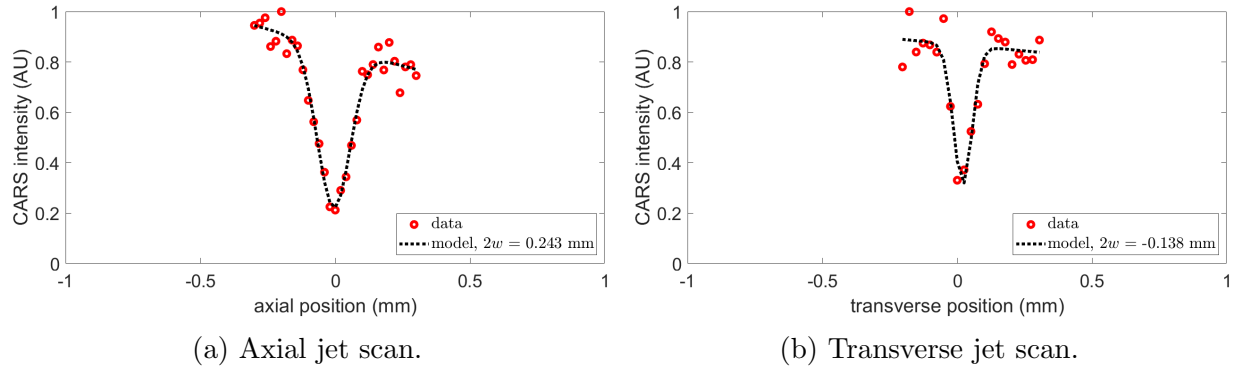
Figure B.13: Case M jet measurements.

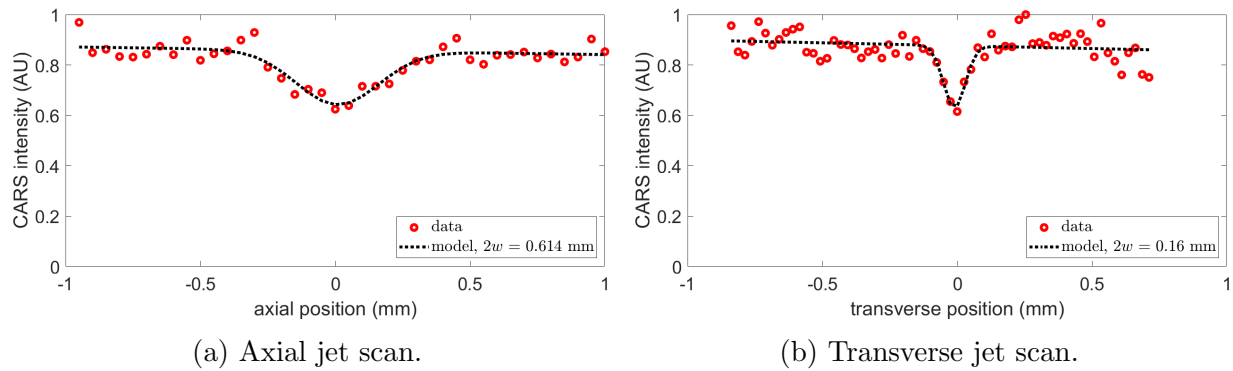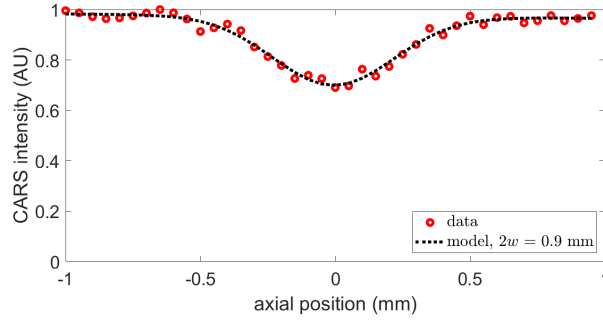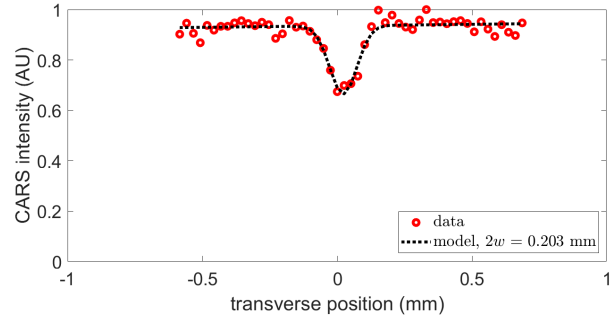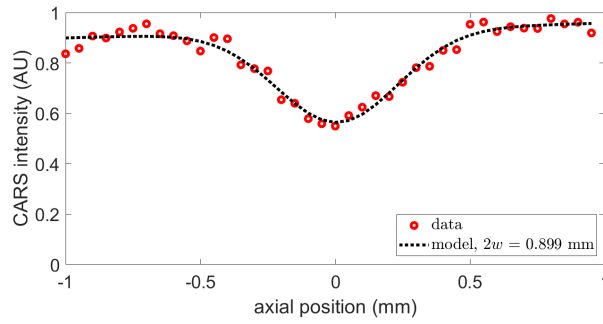(a) Axial jet scan.

(b) Transverse jet scan.
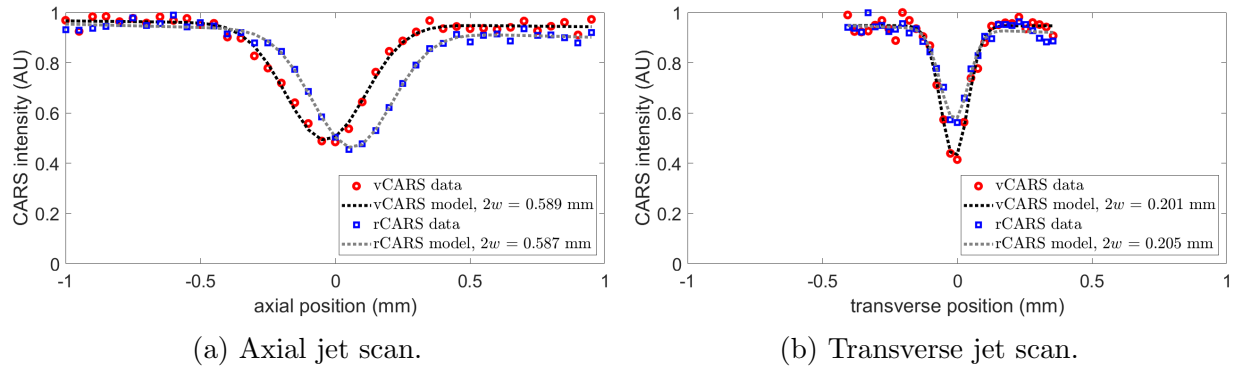
Figure B.14: Case N jet measurements.
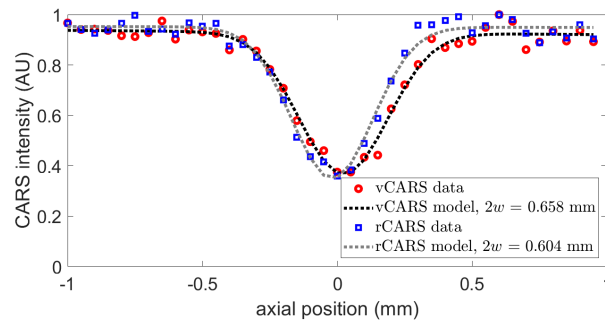
Figure B.15: Case O axial jet scan. No transverse scan was acquired for this case.

(a) Axial jet scan.   (b) Transverse jet scan.
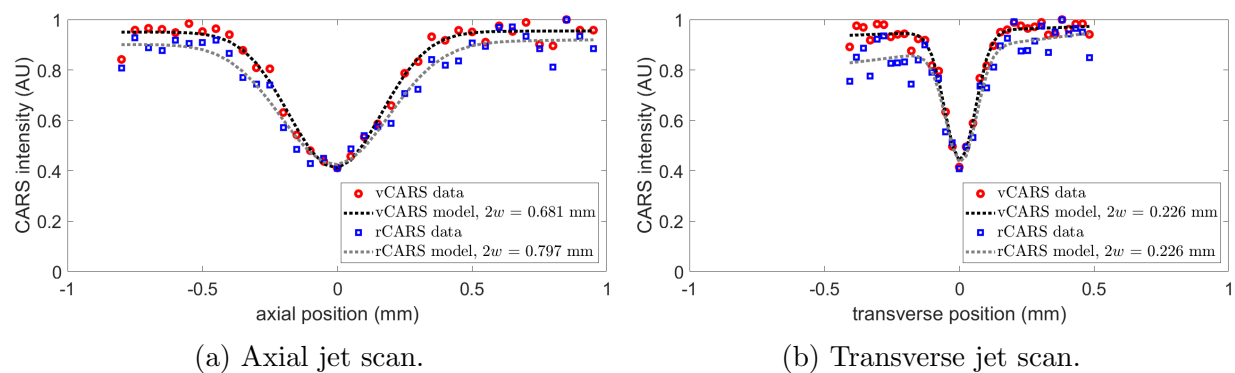
Figure B.16: Case P jet measurements.

B.3   CARS beam profiles

The following figures present beam profile images and 2D Gaussian models for beam profiles
for the different beam crossing configurations presented in Chapter 5.

(a) Beam profile images.   (b) Beam profile model.
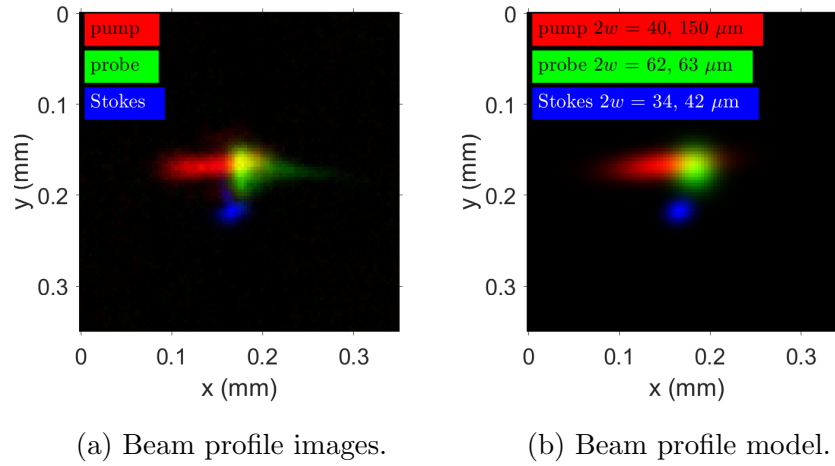
Figure B.17: Case A beam profiles.

(a) Beam profile images.   (b) Beam profile model.
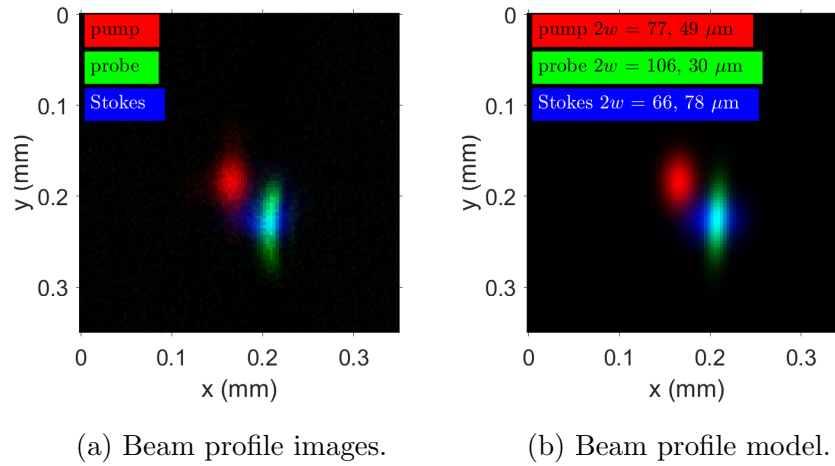
Figure B.18: Case B beam profiles.

(a) Beam profile images.

(b) Beam profile model.
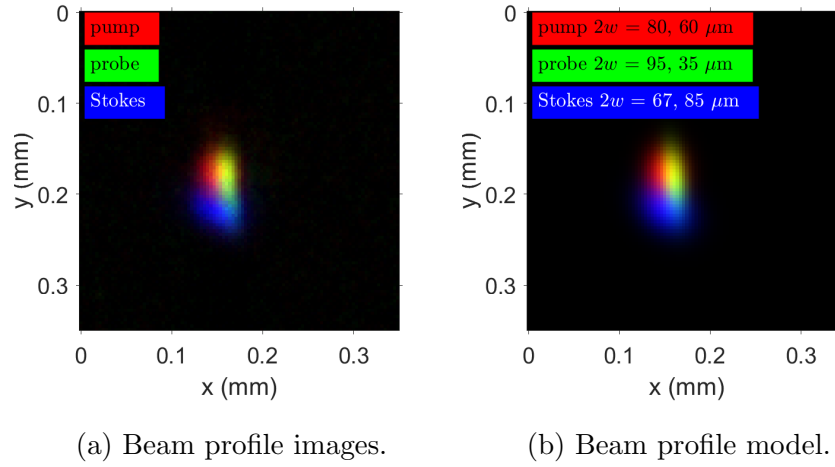
Figure B.19: Case C beam profiles.

(a) Beam profile images.

(b) Beam profile model.
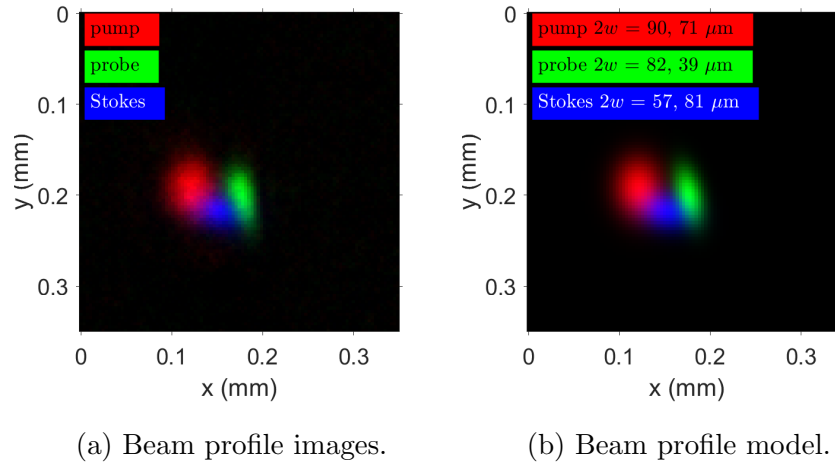
Figure B.20: Case D beam profiles.

(a) Beam profile images.

(b) Beam profile model.
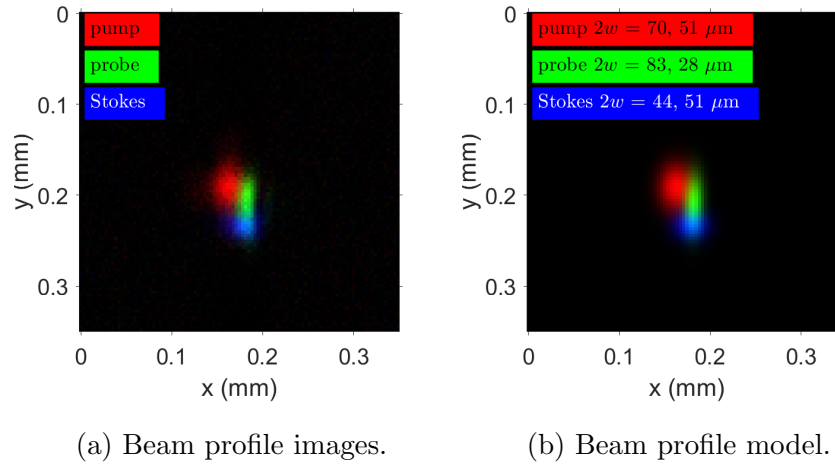
Figure B.21: Case E beam profiles.

(a) Beam profile images.

(b) Beam profile model.
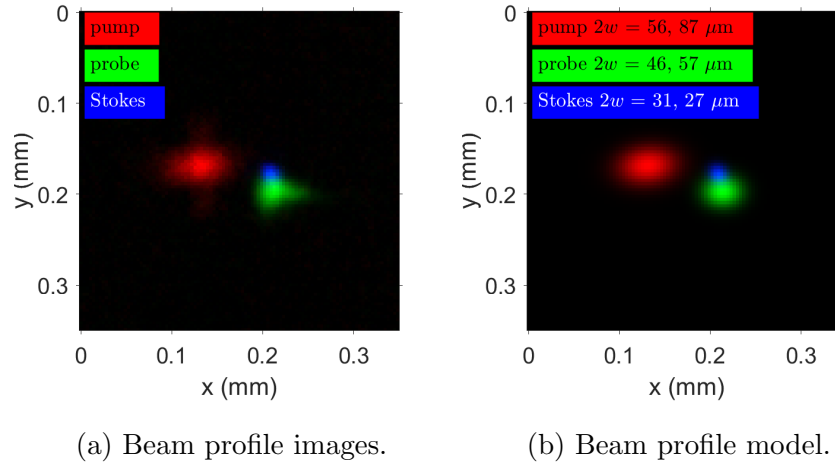
Figure B.22: Case F beam profiles.

(a) Beam profile images.

(b) Beam profile model.
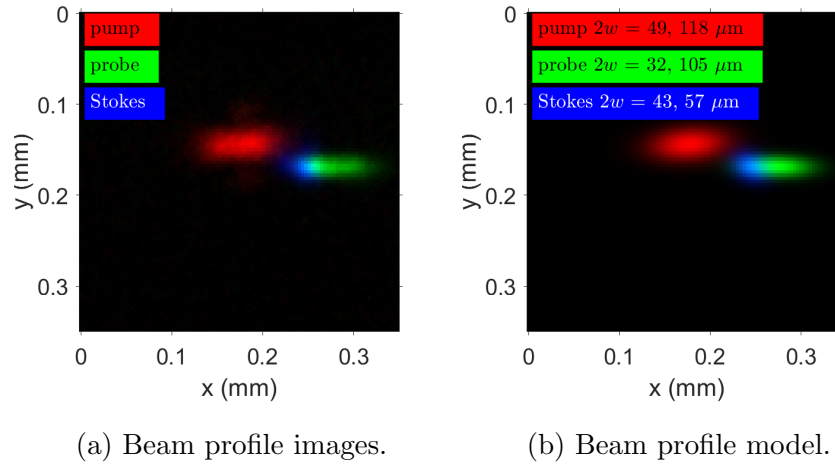
Figure B.23: Case G beam profiles.

(a) Beam profile images.

(b) Beam profile model.
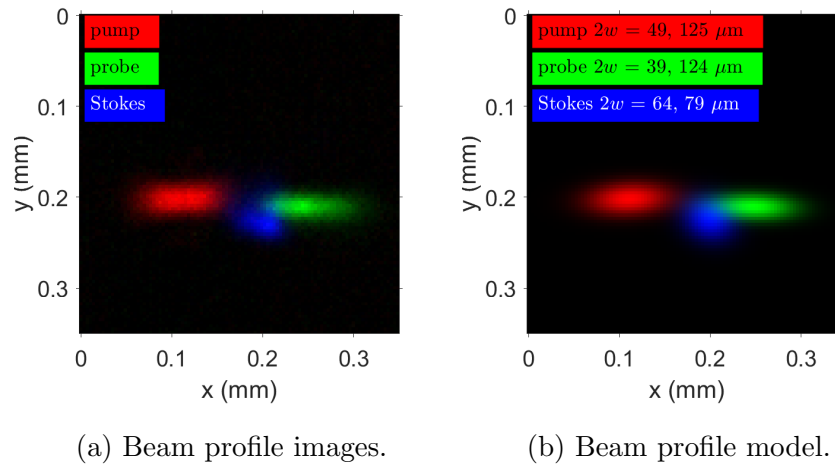
Figure B.24: Case H beam profiles.

(a) Beam profile images.

(b) Beam profile model.
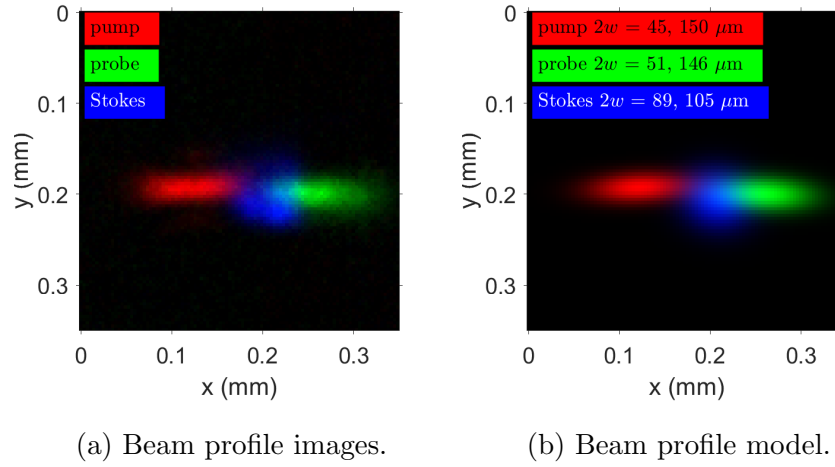
Figure B.25: Case I beam profiles.

(a) Beam profile images.

(b) Beam profile model.
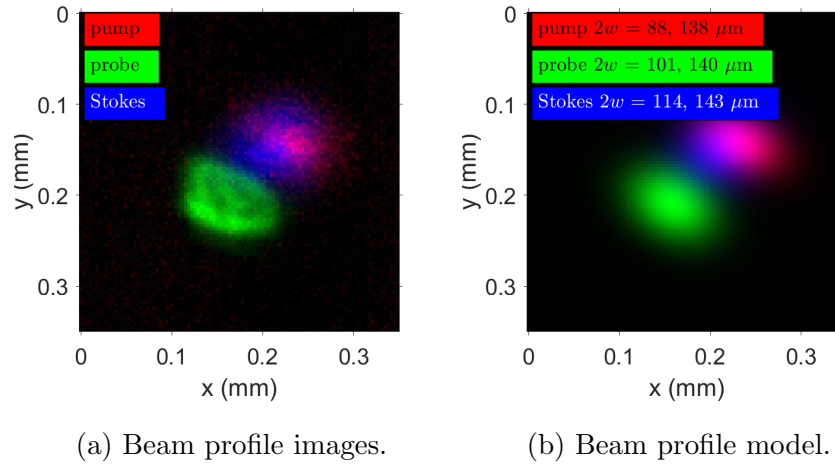
Figure B.26: Case J beam profiles.

(a) Beam profile images.

(b) Beam profile model.
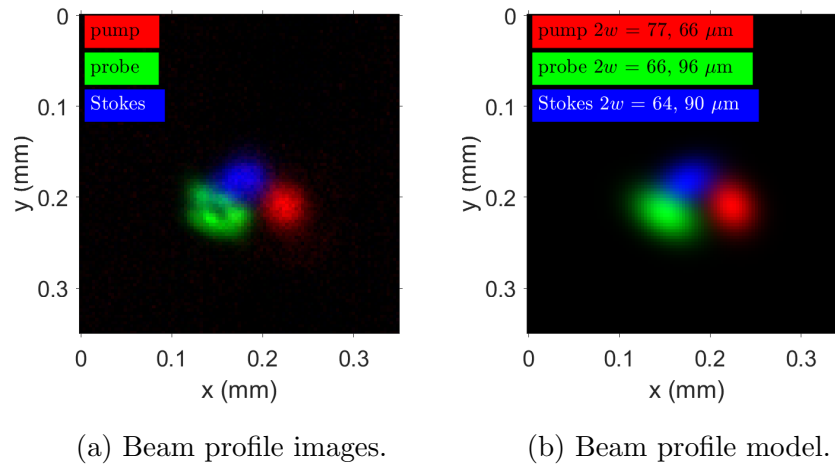
Figure B.27: Case K beam profiles.

(a) Beam profile images.   (b) Beam profile model.
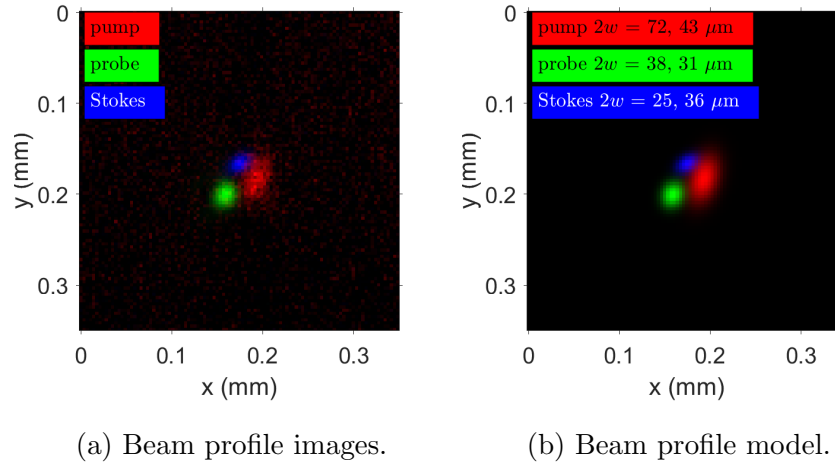
Figure B.28: Case L beam profiles.

(a) Beam profile images.   (b) Beam profile model.
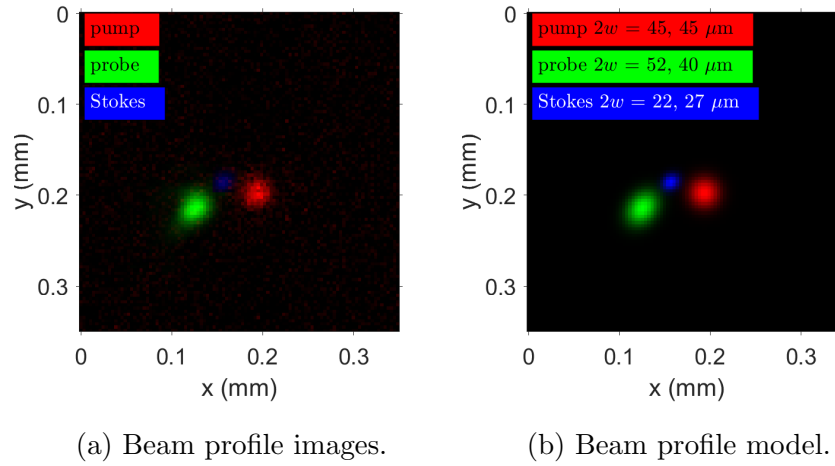
Figure B.29: Case M beam profiles.

(a) Beam profile images.   (b) Beam profile model.
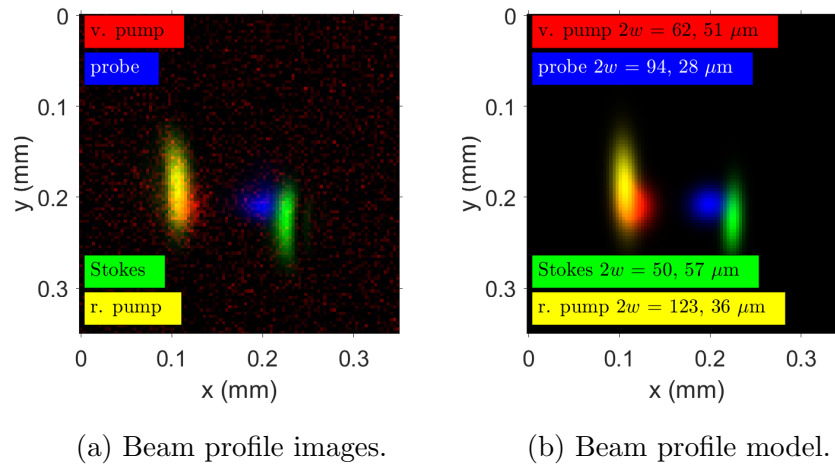
Figure B.30: Case N beam profiles.

(a) Beam profile images.   (b) Beam profile model.
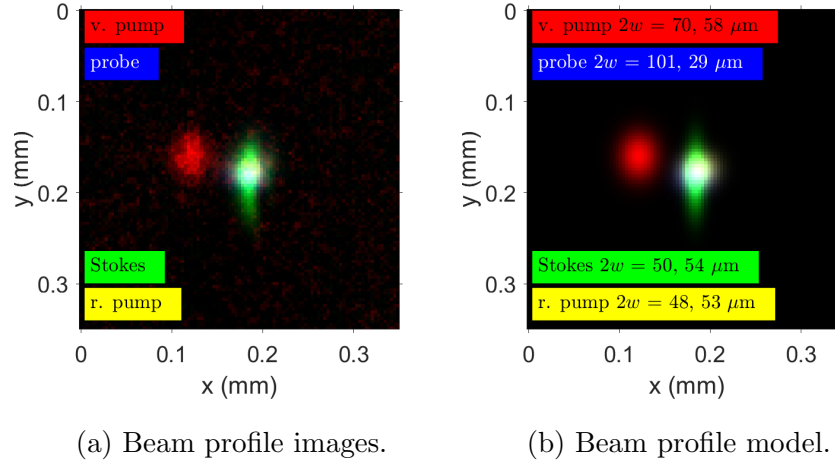
Figure B.31: Case O beam profiles.

(a) Beam profile images.   (b) Beam profile model.
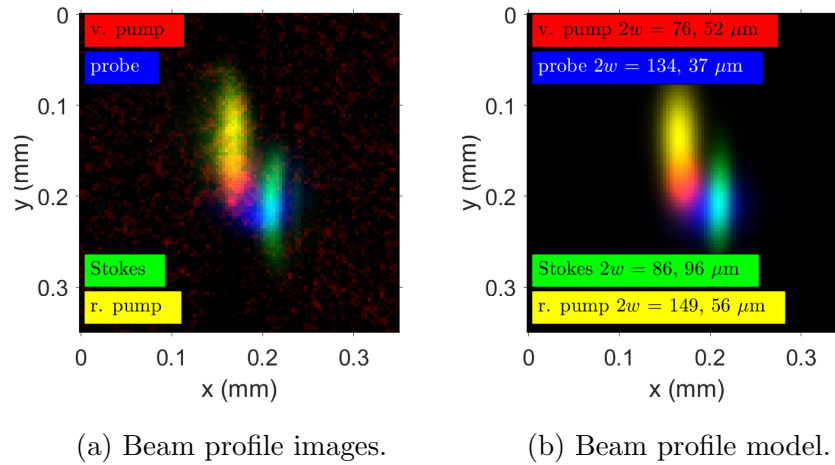
Figure B.32: Case P beam profiles.

B.4 Supplemental CARS setup information

Figure B.33 presents a typical background-corrected rotational CARS spectrum. Figure B.34 shows the magnitude of nonresonant CARS signal generated in glass at many different probe delays; it shows that the probe pulse used throughout Chapter 5 has a shape similar to a sinc-squared function with a full-width at half-maximum of approximately 4 ps.
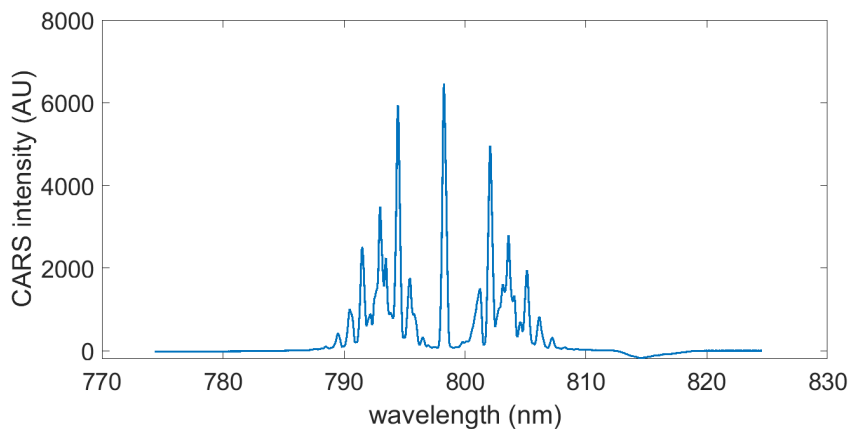
Figure B.33: Example rotational CARS spectrum.
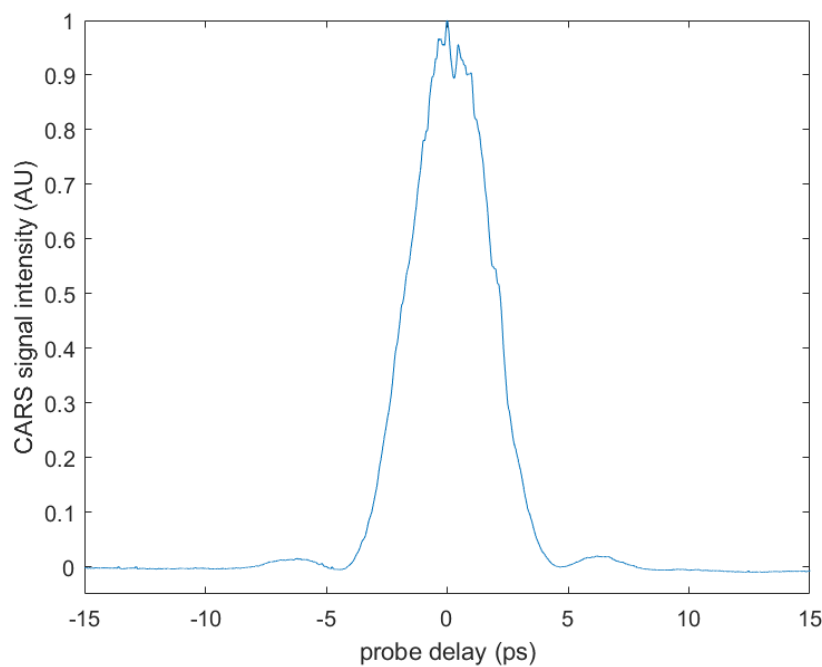
Figure B.34: Nonresonant CARS signal level in glass, as a function of probe delay.

Bibliography

[1] NASA Langley Research Center, "How Scramjets Work," 2006.

[2] R. C. Murray and G. S. Elliott, "Characteristics of the compressible shear layer over a cavity," *AIAA Journal*, vol. 39, pp. 846–856, 1 2001.

[3] A. Ben-Yakar and R. K. Hanson, "Cavity Flame-Holders for Ignition and Flame Stabilization in Scramjets: An Overview," *Journal of Propulsion and Power*, vol. 17, no. 4, pp. 869–877, 2001.

[4] M. R. Gruber, R. A. Baurle, T. Mathur, and K. Y. Hsu, "Fundamental Studies of Cavity-Based Flameholder Concepts for Supersonic Combustors," *Journal of Propulsion and Power*, vol. 17, no. 1, pp. 146–153, 2001.

[5] J. Drummond and M. Carpenter, "Mixing and Mixing Enhancement in Supersonic Reacting Flowfields," in *High-Speed Flight Propulsion Systems* (E. T. Curran and S. N. B. Murthy, eds.), pp. 383–455, Washington DC: AIAA, 1 1991.

[6] E. J. Gutmark, K. C. Schadow, and K. H. Yu, "Mixing Enhancement in Supersonic Free Shear Flows," *Annual Review of Fluid Mechanics*, vol. 27, pp. 375–417, 1 1995.

[7] C. C. Rasmussen, J. F. Driscoll, K. Y. Hsu, J. M. Donbar, M. R. Gruber, and C. D. Carter, "Stability limits of cavity-stabilized flames in supersonic flow," *Proceedings of the Combustion Institute*, vol. 30 II, no. 2, pp. 2825–2833, 2005.

[8] D. J. Micka and J. F. Driscoll, "Combustion characteristics of a dual-mode scramjet combustor with cavity flameholder," *Proceedings of the Combustion Institute*, vol. 32, no. 2, pp. 2397–2404, 2009.

[9] T. Nielsen, J. Edwards, H. Chelliah, D. Lieber, C. Geipel, C. Goyne, R. Rockwell, and A. Cutler, "Hybrid LES/RANS simulation of a premixed ethylene-fueled dual-mode scramjet combustor: Small cavity configuration," in *AIAA Scitech 2019 Forum*, 2019.

[10] R. Rockwell, C. Goyne, H. Chelliah, J. McDaniel, B. Rice, J. Edwards, L. Cantu, E. Gallo, A. Cutler, and P. Danehy, "Development of a Premixed Combustion Capability for Dual-Mode Scramjet Experiments," *Journal of Propulsion and Power*, vol. 34, 2017.

[11] J. F. Driscoll, "Turbulent premixed combustion: Flamelet structure and its effect on turbulent burning velocities," *Progress in Energy and Combustion Science*, vol. 34, no. 1, pp. 91–134, 2008.

[12] S. A. Filatyev, J. F. Driscoll, C. D. Carter, and J. M. Donbar, "Measured properties of turbulent premixed flames for model assessment, including burning velocities, stretch rates, and surface densitites," *Combustion and Flame*, vol. 141, no. 1-2, 2005.

[13] F. A. Williams, *Combustion Theory*. CRC Press, 3 1985.

[14] N. Peters, *Turbulent Combustion*. Cambridge University Press, 8 2000.

[15] V. Zimont, W. Polifke, M. Bettelini, and W. Weisenstein, "An Efficient Computational Model for Premixed Turbulent Combustion at High Reynolds Numbers Based on a Turbulent Flame Speed Closure," *Journal of Engineering for Gas Turbines and Power*, vol. 120, pp. 526–532, 7 1998.

[16] V. Vinogradov, S. Kobyzhskii, and M. Petrov, "Experimental investigation of liquid carbonhydrogen fuel combustion in channel at supersonic velocities," in *28th Joint Propulsion Conference and Exhibit*, (Reston, Virigina), American Institute of Aeronautics and Astronautics, 7 1992.

[17] D. J. Micka and J. F. Driscoll, "Combustion characteristics of a dual-mode scramjet combustor with cavity flameholder," *Proceedings of the Combustion Institute*, vol. 32, no. 2, pp. 2397–2404, 2009.

[18] K.-C. Lin, C.-J. Tam, I. Boxx, C. Carter, K. Jackson, and M. Lindsey, "Flame Characteristics and Fuel Entrainment Inside as Cavity Flame Holder in a Scramjet Combustor," in *43rd AIAA/ASME/SAE/ASEE Joint Propulsion Conference and Exhibit*, (Cincinnati, OH), AIAA, 2007.

[19] T. Mathur, M. Gruber, K. Jackson, J. Donbar, W. Donaldson, T. Jackson, and F. Billig, "Supersonic Combustion Experiments with a Cavity-Based Fuel Injector," *Journal of Propulsion and Power*, vol. 17, no. 6, pp. 1305–1312, 2001.

[20] W. J. Tango, J. K. Link, and R. N. Zare, "Spectroscopy of K 2 Using Laser-Induced Fluorescence," *The Journal of Chemical Physics*, vol. 49, pp. 4264–4268, 11 1968.

[21] J. L. Kinsey, "Laser-Induced Fluorescence," *Annual Review of Physical Chemistry*, vol. 28, pp. 349–372, 10 1977.

[22] R. K. Hanson, "Planar laser-induced fluorescence imaging," *Journal of Quantitative Spectroscopy and Radiative Transfer*, vol. 40, pp. 343–362, 9 1988.

[23] G. Kychakoff, R. D. Howe, R. K. Hanson, and J. C. McDaniel, "Quantitative visualization of combustion species in a plane," *Applied Optics*, vol. 21, no. 18, pp. 3225–3227, 1980.

[24] R. K. Hanson, "Combustion diagnostics: Planar imaging techniques," *Symposium (International) on Combustion*, vol. 21, pp. 1677–1691, 1 1988.

[25] A. C. Eckbreth, *Laser Diagnostics for Combustion Temperature and Species*. Amsterdam: Gordon and Breach, 1996.

[26] K. N. Gabet, R. A. Patton, N. Jiang, W. R. Lempert, and J. A. Sutton, "High-speed CH 2O PLIF imaging in turbulent flames using a pulse-burst laser system," *Applied Physics B: Lasers and Optics*, vol. 106, no. 3, pp. 569–575, 2012.

[27] H. Joel and K. Smyth, "Laser-induced Fluorescense Measurements of Formaldehyde in a methane-air diffucion flame at 603K," *Chemical Physics Letters*, vol. 202, no. 3,4, 1993.

[28] R. Bombach and B. Käppeli, "Simultaneous visualisation of transient species in flames by planar-laser-induced fluorescence using a single laser system," *Applied Physics B: Lasers and Optics*, vol. 68, no. 2, pp. 251–255, 1999.

[29] P. M. Danehy, B. Bathel, C. Ivey, J. A. Inman, and S. B. Jones, "NO PLIF study of hypersonic transition over a discrete hemispherical roughness element," *47th AIAA Aerospace Sciences Meeting including the New Horizons Forum and Aerospace Exposition*, 2009.

[30] J. D. Miller, C. E. Dedic, S. Roy, J. R. Gord, and T. R. Meyer, "Interference-free gas-phase thermometry at elevated pressure using hybrid femtosecond/picosecond rotational coherent anti-Stokes Raman scattering," *Optics Express*, vol. 20, no. 5, p. 5003, 2012.

[31] T. D. Hedman, K. Y. Cho, M. A. Pfeil, A. Satija, H. C. Mongia, L. J. Groven, R. P. Lucht, and S. F. Son, "High speed OH PLIF applied to multiphase combustion (Review)," *Combustion, Explosion and Shock Waves*, vol. 52, no. 1, pp. 1–13, 2016.

[32] R. R. Boyce, N. R. Mudford, and J. R. McGuire, "OH-PLIF visualisation of radical farming supersonic combustion flows," *Shock Waves*, vol. 22, no. 1, pp. 9–21, 2012.

[33] M. Richter, R. Collin, J. Nygren, M. Aldén, L. Hildingsson, and B. Johansson, "Studies of the combustion process with simultaneous formaldehyde and OH PLIF in a direct-injected HCCI engine," *JSME International Journal, Series B: Fluids and Thermal Engineering*, vol. 48, no. 4, pp. 701–707, 2006.

[34] Z. S. Li, B. Li, Z. W. Sun, X. S. Bai, and M. Aldén, "Turbulence and combustion interaction: High resolution local flame front structure visualization using simultaneous single-shot PLIF imaging of CH, OH, and CH2O in a piloted premixed jet flame," *Combustion and Flame*, vol. 157, no. 6, pp. 1087–1096, 2010.

[35] B. K. McMillin, J. M. Seitzman, and R. K. Hanson, "Comparison of NO and OH planar fluorescence temperature measurements in scramjet model flowfields," *AIAA Journal*, vol. 32, no. 10, pp. 1945–1952, 1994.

[36] R. J. Locke, Y. R. Hicks, R. C. Anderson, and K. A. Ockunzzi, "OH imaging in a lean burning high-pressure combustor," *AIAA Journal*, vol. 34, no. 3, pp. 622–624, 1996.

[37] X. Rao, S. Hammack, T. Lee, C. Carter, and I. B. Matveev, "Combustion dynamics of plasma-enhanced premixed and nonpremixed flames," *IEEE Transactions on Plasma Science*, vol. 38, no. 12 PART 1, pp. 3265–3271, 2010.

[38] C. T. Johansen, C. D. McRae, P. M. Danehy, E. C. A. Gallo, L. M. L. Cantu, G. Magnotti, A. D. Cutler, R. D. Rockwell, C. P. Goyne, and J. C. McDaniel, "OH PLIF visualization of the UVa supersonic combustion experiment: configuration A," *Journal of Visualization*, vol. 17, no. 2, pp. 131–141, 2014.

[39] S. O'Byrne, I. Stotz, A. J. Neely, R. R. Boyce, N. R. Mudford, and A. F. P. Houwing, "OH PLIF Imaging of Supersonic Combustion using Cavity Injection," in *AIAA/CIRA 13th International Space Planes and Hypersonics Systems and Technologies Conference*, (Capua, Italy), AIAA/CIRA, 2005.

[40] J. M. Donbar, M. R. Gruber, T. A. Jackson, C. D. Carter, and T. Mathur, "OH planar laser-induced fluorescence imaging in a hydrocarbon-fueled scramjet combustor," *Proceedings of the Combustion Institute*, vol. 28, no. 1, pp. 679–687, 2000.

[41] S. D. Hammack, T. Lee, K. Y. Hsu, and C. D. Carter, "High-repetition-rate OH planar laser-induced fluorescence of a cavity flameholder," *Journal of Propulsion and Power*, vol. 29, no. 5, pp. 1248–1251, 2013.

[42] A. Rauch, *Direct Numerical Simulation of Cavity-Stabilized Premixed Turbulent Flame*. PhD thesis, 2020.

[43] A. H. Rauch, K. Aditya, H. Kolla, J. H. Chen, and H. K. Chelliah, "DNS Investigation of Cavity Stabilized Premixed Turbulent Ethylene-Air Flame," in *58th Aerospace Sciences Meeting, AIAA Science and Technology Forum*, (Kissimmee, Florida), AIAA, 2018.

[44] A. C. Eckbreth, "Recent advances in laser diagnostics for temperature and species concentration in combustion," *Symposium (International) on Combustion*, vol. 18, no. 1, pp. 1471–1488, 1981.

[45] J. R. Gord, T. R. Meyer, and S. Roy, "Applications of ultrafast lasers for optical measurements in combusting flows," *Annual Review of Analytical Chemistry*, vol. 1, no. 1, pp. 663–687, 2008.

[46] G. C. Alessandretti and P. Violino, "Thermometry by CARS in an automobile engine," *Journal of Physics D: Applied Physics*, vol. 16, no. 9, pp. 1583–1594, 1983.

[47] S. P. Kearney and D. R. Guildenbecher, "Temperature measurements in metalized propellant combustion using hybrid fs/ps coherent anti-Stokes Raman scattering," *Applied Optics*, vol. 55, p. 4958, 6 2016.

[48] C. E. Dedic, J. B. Michael, and T. R. Meyer, "Investigation of energy distributions behind a microscale gas-phase detonation tube using hybrid fs/ps coherent anti-Stokes Raman scattering," in *55th AIAA Aerospace Sciences Meeting*, (Reston, Virginia), American Institute of Aeronautics and Astronautics, 1 2017.

[49] W. G. Vincenti and C. H. Kruger, *Introduction to Physical Gas Dynamics*. New York: John Wiley, 1965.

[50] A. C. Eckbreth and T. J. Anderson, "Dual broadband CARS for simultaneous, multiple species measurements," *Applied Optics*, vol. 24, p. 2731, 8 1985.

[51] C. E. Dedic, *Hybrid fs/ps coherent anti-Stokes Raman scattering for multiparameter measurements of combustion and nonequilibrium*. PhD thesis, 2017.

[52] S. P. Kearney, "Hybrid fs/ps rotational CARS temperature and oxygen measurements in the product gases of canonical flat flames," *Combustion and Flame*, vol. 162, no. 5, pp. 1748–1758, 2014.

[53] F. M. Kamga and M. G. Sceats, "Pulse-sequenced coherent anti-Stokes Raman scattering spectroscopy: a method for suppression of the nonresonant background," *Optics Letters*, vol. 5, no. 3, p. 126, 1980.

[54] S. Roy, T. R. Meyer, and J. R. Gord, "Time-resolved dynamics of resonant and nonresonant broadband picosecond coherent anti-Stokes Raman scattering signals," *Applied Physics Letters*, vol. 87, no. 26, pp. 1–3, 2005.

[55] T. R. Meyer, S. Roy, and J. R. Gord, "Improving Signal-to-Interference Ratio in Rich Hydrocarbon–Air Flames Using Picosecond Coherent Anti-Stokes Raman Scattering," *Appl. Spectrosc.*, vol. 61, pp. 1135–1140, 11 2007.

[56] W. D. Kulatilaka, H. U. Stauffer, J. R. Gord, and S. Roy, "One-dimensional single-shot thermometry in flames using femtosecond-CARS line imaging," *Optics Letters*, vol. 36, p. 4182, 11 2011.

[57] A. Bohlin, B. D. Patterson, and C. J. Kliewer, "Communication: Simplified two-beam rotational CARS signal generation demonstrated in 1D," *Journal of Chemical Physics*, vol. 138, no. 8, 2013.

[58] D. R. Richardson, S. Roy, J. R. Gord, and S. P. Kearney, "Two-beam femtosecond rotational CARS for one-dimensional thermometry in a turbulent, sooting jet flame," *Frontiers in Ultrafast Optics: Biomedical, Scientific, and Industrial Applications XVII*, vol. 10094, no. February 2017, 2017.

[59] A. Bohlin, C. Jainski, B. D. Patterson, A. Dreizler, and C. J. Kliewer, "Multiparameter spatio-thermochemical probing of flame-wall interactions advanced with coherent Raman imaging," *Proceedings of the Combustion Institute*, vol. 36, no. 3, pp. 4557–4564, 2017.

[60] A. C. Eckbreth, "BOXCARS: Crossed-beam phase-matched CARS generation in gases," *Applied Physics Letters*, vol. 32, no. 7, pp. 421–423, 1978.

[61] D. Romanov, A. Filin, R. Compton, and R. Levis, "Phase matching in femtosecond BOXCARS," *Optics Letters*, vol. 32, no. 21, p. 3161, 2007.

[62] M. C. Weikl, Y. Cong, T. Seeger, and A. Leipertz, "Development of a simplified dual-pump dual-broadband coherent anti-Stokes Raman scattering system," *Applied Optics*, vol. 48, no. 4, 2009.

[63] A. Bohlin, E. Nordström, H. Carlsson, X. S. Bai, and P. E. Bengtsson, "Pure rotational CARS measurements of temperature and relative O 2-concentration in a low swirl turbulent premixed flame," *Proceedings of the Combustion Institute*, vol. 34, no. 2, pp. 3629–3636, 2013.

[64] A. D. Cutler, E. C. Gallo, L. M. Cantu, R. D. Rockwell, and C. P. Goyne, "Coherent anti-Stokes Raman spectroscopy of a premixed ethylene–air flame in a dual-mode scramjet," *Combustion and Flame*, vol. 189, pp. 92–105, 2018.

[65] T. Seeger and A. Leipertz, "Experimental comparison of single-shot broadband vibrational and dual-broadband pure rotational coherent anti-Stokes Raman scattering in hot air," *Applied Optics*, vol. 35, no. 15, p. 2665, 1996.

[66] J. E. Retter, G. S. Elliott, and S. P. Kearney, "Dielectric-barrier-discharge plasma-assisted hydrogen diffusion flame. Part 1: Temperature, oxygen, and fuel measurements by one-dimensional fs/ps rotational CARS imaging," *Combustion and Flame*, vol. 191, pp. 527–540, 2018.

[67] R. L. Farrow, P. L. Mattern, and L. A. Rahn, "Comparison between CARS and corrected thermocouple temperature measurements in a diffusion flame," *Applied Optics*, vol. 21, no. 17, p. 3119, 1982.

[68] D. R. Richardson, S. P. Kearney, and D. R. Guildenbecher, "Post-detonation fireball thermometry via femtosecond-picosecond coherent anti-Stokes Raman Scattering (CARS)," *Proceedings of the Combustion Institute*, pp. 1–8, 2020.

[69] J. D. Miller, *Hybrid femtosecond/picosecond coherent anti-Stokes Raman scattering for gas-phase temperature measurements*. PhD thesis, Iowa State University, 2012.

[70] J. B. Snow, J.-b. Zheng, and R. K. Chang, "Spatially and spectrally resolved multi-point coherent anti-Stokes Raman scattering from N_2 and O_2 flows," *Optics Letters*, vol. 8, p. 599, 12 1983.

[71] A. Bohlin and C. J. Kliewer, "Two-beam ultrabroadband coherent anti-Stokes Raman spectroscopy for high resolution gas-phase multiplex imaging," *Applied Physics Letters*, vol. 104, no. 3, 2014.

[72] D. A. Greenhalgh, "Comments on the use of BOXCARS for gas-phase CARS spectroscopy," *Journal of Raman Spectroscopy*, vol. 14, pp. 150–153, 6 1983.

[73] S. A. Tedder, M. C. Weikl, T. Seeger, and A. Leipertz, "Determination of probe volume dimensions in coherent measurement techniques," *Applied Optics*, vol. 47, no. 35, pp. 6601–6605, 2008.

[74] K. A. Marko and L. Rimai, "Coherent Anti-Stokes Raman Spectroscopic Probe of Combustion," 2 1980.

[75] D. Klick, K. A. Marko, and L. Rimai, "Broadband single-pulse CARS spectra in a fired internal combustion engine," *Applied Optics*, vol. 20, no. 7, p. 1178, 1981.

[76] L. C. Davis, K. A. Marko, and L. Rimai, "Angular distribution of coherent Raman emission in degenerate four-wave mixing with pumping by a single diffraction coupled laser beam: configurations for high spatial resolution," *Applied Optics*, vol. 20, no. 9, p. 1685, 1981.

[77] D. Lieber, C. Goyne, R. Rockwell, C. Geipel, and H. Chelliah, "Design and testing of an additively manufactured flameholder for scramjets flows," in *2018 Joint Propulsion Conference*, 2018.

[78] R. Krauss and J. C. McDaniel, "A clean air continuous flow propulsion facility," in *28th Joint Propulsion Conference and Exhibit*, (Nashville, TN), AIAA, 1992.

[79] W. Heiser, D. Pratt, D. Daley, and U. Mehta, *Hypersonic Airbreathing Propulsion*. Washington, DC: American Institute of Aeronautics and Astronautics, Inc., 1 1994.

[80] L. M. L. Cantu, E. C. A. Gallo, A. D. Cutler, P. M. Danehy, R. D. Rockwell, C. T. Johansen, C. P. Goyne, and J. C. McDaniel, "OH PLIF Visualization of a Premixed Ethylene-fueled Dual-Mode Scramjet Combustor," in *54th Aerospace Sciences Meeting, AIAA SciTech Forum*, (San Diego, CA), AIAA, 2016.

[81] J. W. Kirik, C. P. Goyne, J. C. McDaniel, R. D. Rockwell, L. M. L. Cantu, E. C. A. Gallo, and A. D. Cutler, "Aerodynamic characterization of a cavity flameholder in a premixed dual-mode scramjet," *Journal of Propulsion and Power*, vol. 34, no. 3, pp. 739–749, 2018.

[82] K. Ramesh, J. R. Edwards, H. Chelliah, C. Goyne, J. McDaniel, R. Rockwell, J. Kirik, A. Cutler, and P. Danehy, "Large eddy simulation of high-speed, premixed ethylene combustion," *53rd AIAA Aerospace Sciences Meeting*, 2015.

[83] D. Lieber, *High-Resolution Velocimetry of a Dual-Mode Scramjet Flameholder*. PhD thesis, University of Virginia, 2018.

[84] H. Kobayashi, T. Kawahata, K. Seyama, T. Fujimari, and J. Kim, "Relationship between the smallest scale of flame wrinkles and turbulence characteristics of high-pressure, high-temperature turbulent premixed flames," *Proceedings of the Combustion Institute*, vol. 29, no. 2, pp. 1793–1800, 2002.

[85] J. Westerweel, G. E. Elsinga, and R. J. Adrian, "Particle Image Velocimetry for Complex and Turbulent Flows," *Annual Review of Fluid Mechanics*, vol. 45, pp. 409–436, 2013.

[86] E. W. Weisstein, "Gaussian Function," 2020.

[87] R. C. Hilborn, "Einstein coefficients, cross sections, f values, dipole moments, and all that," *American Journal of Physics*, vol. 50, pp. 982–986, 11 1982.

[88] C. D. Carter and T. Lee, *Calculation of the Overlap Integral.* unpublished.

[89] E. C. Rea, A. Y. Chang, and R. K. Hanson, "Collisional broadening of the A2Σ+ X2Π(0,0) band of OH by H2O and CO2 in atmospheric-pressure flames," *Journal of Quantitative Spectroscopy and Radiative Transfer*, vol. 41, no. 1, pp. 29–42, 1989.

[90] J. J. Girard, R. Choudhary, and R. K. Hanson, "Collisional-induced broadening and shift parameters of OH with Ar and N2 near 308.6nm, measured at T=1300–2000K and P=20–100atm," *Journal of Quantitative Spectroscopy and Radiative Transfer*, vol. 221, pp. 194–201, 2018.

[91] J. J. Girard, S. Clees, and R. K. Hanson, "Collisional broadening and shift of five OH A2Σ+X2Π (0-0) transitions in the Q1-branch, by H2O, O2, CO2, N2 and Ar, at 1220 K," *Journal of Quantitative Spectroscopy and Radiative Transfer*, vol. 240, 2020.

[92] W. J. Smith, "The Modulation Transfer Function," in *Modern optical engineering: the design of optical systems*, pp. 366–372, 2000.

[93] N. T. Clemens, "Flow Imaging," in *Encyclopedia of Imaging Science and Technology*, pp. 390–419, Wiley, 2002.

[94] A. E. Bayley, Y. Hardalupas, and A. M. K. P. Taylor, "Local curvature measurements of a lean, partially premixed swirl-stabilized flame," *Experimental Fluids*, vol. 52, pp. 963–983, 2012.

[95] P. Perona and J. Malik, "Scale-Space and Edge Detection Using Aniosotropic Diffusion," *IEEE Transactions on Pattern Analysis and Machine Intelligence*, vol. 12, no. 7, pp. 629–639, 1990.

[96] D. Lopes, "Anisotropic Diffusion (Perona & Malik)," 2007.

[97] I. Sobel and G. Feldman, "History and Definition of the so-called "Sobel Operator", more appropriately named the Sobel-Feldman Operator," Tech. Rep. June, 2015.

[98] P. Soille, "Opening and Closing," in *Morphological Image Analysis*, ch. 4, pp. 105–138, Springer, 2013.

[99] J. F. Driscoll, "Turbulent premixed combustion: Flamelet structure and its effect on turbulent burning velocities," *Energy and Combustion Science*, vol. 34, no. 1, pp. 91–134, 2008.

[100] Z. Wang, H. Wang, and M. Sun, "Review of cavity-stabilized combustion for scram-jet applications," *Proceedings of the Institution of Mechanical Engineers, Part G: Journal of Aerospace Engineering*, vol. 228, pp. 2718–2735, 10 2014.

[101] K.-C. Lin, K. Jackson, R. Behdadnia, T. A. Jackson, F. Ma, and V. Yang, "Acoustic Characterization of an Ethylene-Fueled Scramjet Combustor with a Cavity Flame-holder," *Journal of Propulsion and Power*, vol. 26, pp. 1161–1170, 10 2010.

[102] J. Hult, S. Gashi, N. Chakraborty, M. Klein, K. W. Jenkins, S. Cant, and C. F. Kaminski, "Measurement of flame surface density for turbulent premixed flames using PLIF and DNS," *Proceedings of the Combustion Institute*, vol. 31, pp. 1319–1326, 2007.

[103] J. B. Bell, M. S. Day, J. F. Grcar, M. J. Lijewski, J. F. Driscoll, and S. A. Filatyev, "Numerical simulation of a laboratory-scale turbulent slot flame," *Proceedings of the Combustion Institute*, vol. 31, pp. 1299–1307, 1 2007.

[104] C. J. Lawn and R. W. Schefer, "Scaling of premixed turbulent flames in the corrugated regime," *Combustion and Flame*, vol. 146, pp. 180–199, 2006.

[105] D. Veynante, J. Piana, J. M. Duclos, and C. Martel, "Experimental analysis of flame surface density models for premixed turbulent combustion," *Proceedings of the Combustion Institute*, vol. 26, pp. 413–420, 1996.

[106] K. N. C. Bray and R. S. Cant, "Some Applications of Kolmogorov's Turbulence Research in the Field of Combustion," *Proceedings of the Royal Society A: Mathematical, Physical and Engineering Sciences*, vol. 434, no. 1890, pp. 217–240, 1991.

[107] L. Gülder and G. J. Smallwood, "Flame surface densities in premixed combustion at medium to high turbulence intensities," *Combustion Science and Technology*, vol. 179, no. 1-2, pp. 191–206, 2007.

[108] A. Soika, F. Dinkelacker, and A. Leipertz, "Pressure influence on the flame front curvature of turbulent premixed flames," *Combustion and Flame*, vol. 132, no. 3, 2003.

[109] F. Mokhtarian and A. Mackworth, "Scale-based description and recognition of planar curve and two-dimensional shapes," *IEEE Transactions on Pattern Analysis and Machine Intelligence*, vol. 8, no. 1, pp. 34–43, 1986.

[110] R. Ni, S. Huang, and K. Xia, "Lagrangian acceleration measurements in convective thermal turbulence," *Journal of Fluid Mechanics*, vol. 692, pp. 395–419, 2012.

[111] G. Voth, A. La Porta, A. M. Crawford, J. Alexander, and E. Bodenschatz, "Measurement of Particle Accelerations in Fully Developed Turbulence," *Journal of Fluid Mechanics*, vol. 469, pp. 121–160, 2002.

[112] W. T. Ashurst and I. G. Shepherd, "Flame Front Curvature Distributions in a Turbulent Premixed Flame Zone," *Combustion Science and Technology*, vol. 124, pp. 115–144, 3 1997.

[113] J. H. Chen, A. Choudhary, B. De Supinski, M. Devries, E. R. Hawkes, S. Klasky, W. K. Liao, K. L. Ma, J. Mellor-Crummey, N. Podhorszki, R. Sankaran, S. Shende, and C. S. Yoo, "Terascale direct numerical simulations of turbulent combustion using S3D," *Computational Science and Discovery*, vol. 2, no. 1, 2009.

[114] C. A. Kennedy and M. H. Carpenter, "Several new numerical methods for compressible shear-layer simulations," *Applied Numerical Mathematics*, vol. 14, pp. 397–433, 6 1994.

[115] T. M. Wabel, P. Zhang, X. Zhao, H. Wang, E. Hawkes, and A. M. Steinberg, "Assessment of chemical scalars for heat release rate measurement in highly turbulent premixed combustion including experimental factors," *Combustion and Flame*, vol. 194, pp. 485–506, 2018.

[116] C. D. Carter and T. Lee, *Calculation of the Boltzmann Fraction for OH*. unpublished.

[117] P. F. Bernath and R. Colin, "Revised molecular constants and term values for the $X2\Pi$ and $B2\Sigma+$ states of OH," *Journal of Molecular Spectroscopy*, vol. 257, no. 1, pp. 20–23, 2009.

[118] R. F. Johnson, G. B. Goodwin, A. T. Corrigan, A. Kercher, and H. K. Chelliah, "Discontinuous-Galerkin Simulations of Premixed Ethylene-Air Combustion in a Cavity Combustor," in *AIAA Scitech 2019 Forum*, (Reston, Virginia), American Institute of Aeronautics and Astronautics, 1 2019.

[119] G. B. Goodwin, R. F. Johnson, D. Kessler, and H. K. Chelliah, "Premixed Ethylene-Air Combustion in a Dual-Mode Scramjet Cavity Combustor with a Turbulent Inflow," in *AIAA Propulsion and Energy 2019 Forum*, (Reston, Virginia), AIAA, 8 2019.

[120] G. B. Goodwin, R. F. Johnson, D. A. Kessler, A. D. Kercher, and H. K. Chelliah, "Effect of Inflow Turbulence on Premixed Combustion in a Cavity Flameholder," pp. 1–32, 1 2020.

[121] A. H. Rauch and H. K. Chelliah, "On the ambiguity of premixed flame thickness definition of highly pre-heated mixtures and its implication on turbulent combustion regimes," *Combustion Theory and Modelling*, vol. 24, no. 4, pp. 573–588, 2020.

[122] S. P. Kearney, K. Frederickson, and T. W. Grasser, "Dual-pump coherent anti-Stokes Raman scattering thermometry in a sooting turbulent pool fire," *Proceedings of the Combustion Institute*, vol. 32 I, no. 1, pp. 871–878, 2009.

[123] T. Parameswaran and D. R. Snelling, "Estimation of spatial averaging of temperatures from coherent anti-Stokes Raman spectroscopy," *Applied Optics*, vol. 35, no. 27, p. 5461, 1996.

[124] T. Seeger, M. C. Weikl, F. Beyrau, and A. Leipertz, "Identification of spatial averaging effects in vibrational CARS spectra," *Journal of Raman Spectroscopy*, vol. 37, no. 6, pp. 641–646, 2006.

[125] C. E. Dedic, T. R. Meyer, and J. B. Michael, "Single-shot ultrafast coherent anti-Stokes Raman scattering of vibrational/rotational nonequilibrium," *Optica*, vol. 4, no. 5, p. 563, 2017.

[126] A. Monmayrant, S. Weber, and B. Chatel, "A newcomer's guide to ultrashort pulse shaping and characterization," *Journal of Physics B: Atomic, Molecular and Optical Physics*, vol. 43, May 2010.

[127] J. D. Miller, M. N. Slipchenko, T. R. Meyer, H. U. Stauffer, and J. R. Gord, "Hybrid femtosecond/picosecond coherent anti-Stokes Raman scattering for high-speed gas-phase thermometry," *Optics Letters*, vol. 35, no. 14, p. 2430, 2010.

[128] C. M. Geipel, A. H. Rauch, H. K. Chelliah, and C. E. Dedic, "Hybrid fs/ps CARS system for counterflow flame investigation," *Spring Technical Meeting, Eastern States Section of the Combustion Institute*, pp. 1–6, 2020.

[129] B. G. Sarnacki, G. Esposito, R. H. Krauss, and H. K. Chelliah, "Extinction limits and associated uncertainties of nonpremixed counterflow flames of methane, ethylene, propylene and n-butane in air," *Combustion and Flame*, vol. 159, no. 3, pp. 1026–1043, 2012.

[130] H. U. Stauffer, J. D. Miller, M. N. Slipchenko, T. R. Meyer, B. D. Prince, S. Roy, and J. R. Gord, "Time- and frequency-dependent model of time-resolved coherent anti-Stokes Raman scattering (CARS) with a picosecond-duration probe pulse," *Journal of Chemical Physics*, vol. 140, no. 2, 2014.

[131] S. Gordon and B. J. McBride, "Computer Program for Calculation of Complex Chemical Equilibrium Compositions and Applications," tech. rep., NASA Reference Publication 1311, 1994.

[132] G. Magnotti, A. D. Cutler, G. C. Herring, S. A. Tedder, and P. M. Danehy, "Saturation and Stark broadening effects in dual-pump CARS of N2, O2, and H2," *Journal of Raman Spectroscopy*, vol. 43, no. 5, pp. 611–620, 2012.

[133] B. G. Sarnacki and H. K. Chelliah, "Sooting limits of non-premixed counterflow ethylene/oxygen/inert flames using LII: Effects of flow strain rate and pressure (up to 30 atm)," *Combustion and Flame*, vol. 195, pp. 267–281, 2018.

[134] C. Dedic, J. B. Michael, and T. R. Meyer, "Hybrid fs/ps coherent anti-Stokes Raman scattering in a non-equilibrium environment initiated by a ns laser spark," in *46th AIAA Plasmadynamics and Lasers Conference*, (Reston, Virginia), American Institute of Aeronautics and Astronautics, 6 2015.

[135] S. Mukamel, *Principals of Nonlinear Spectroscopy*. New York: Oxford University Press, 1995.

[136] J. D. Miller, M. N. Slipchenko, and T. R. Meyer, "Probe-pulse optimization for non-resonant suppression in hybrid fs/ps coherent anti-Stokes Raman scattering at high temperature," *Optics Express*, vol. 19, no. 14, p. 13326, 2011.

[137] J. B. Michael, M. R. Edwards, A. Dogariu, and R. B. Miles, "Femtosecond laser electronic excitation tagging for quantitative velocity imaging in air," *Applied Optics*, vol. 50, pp. 5158–5162, 9 2011.

[138] N. J. DeLuca, R. B. Miles, N. Jiang, W. D. Kulatilaka, A. K. Patnaik, and J. R. Gord, "FLEET velocimetry for combustion and flow diagnostics," *Applied Optics*, vol. 56, p. 8632, 11 2017.

[139] Y. Zhang, M. N. Shneider, and R. B. Miles, "Femtosecond laser excitation in argon-nitrogen mixtures," *AIAA Journal*, vol. 56, no. 3, pp. 1060–1071, 2018.

[140] C. J. Kliewer, "High-spatial-resolution one-dimensional rotational coherent anti-Stokes Raman spectroscopy imaging using counterpropagating beams," *Optics Letters*, vol. 37, no. 2, p. 229, 2012.

[141] A. Bohlin and P. E. Bengtsson, "Rotational CARS thermometry in diffusion flames: On the influence of nitrogen spectral line-broadening by CH4 and H2," *Proceedings of the Combustion Institute*, vol. 33, no. 1, pp. 823–830, 2011.

[142] C. J. Kliewer, Y. Gao, T. Seeger, B. D. Patterson, R. L. Farrow, and T. B. Settersten, "Quantitative one-dimensional imaging using coherent anti-Stokes Raman spectroscopy," *Applied Optics*, vol. 50, no. 12, pp. 1770–1778, 2011.

[143] A. E. Siegman, *Lasers.* University Science Books, 1986.

[144] O. Svelto, *Principles of Lasers.* Springer, 5th ed., 2010.

[145] M. J. Rahimi and H. K. Chelliah, "Simplified approach to identify thermal choking limits of a dual-mode variable area combustor," *AIAA Journal*, vol. 56, no. 5, pp. 2091–2095, 2018.

[146] A. H. Khalid and K. Kontis, "Thermographic phosphors for high temperature measurements: Principles, current state of the art and recent applications," *Sensors*, vol. 8, no. 9, pp. 5673–5744, 2008.

[147] A. H. Khalid, K. Kontis, and H. Z. Behtash, "Phosphor thermometry in gas turbines: Consideration factors," *Proceedings of the Institution of Mechanical Engineers, Part G: Journal of Aerospace Engineering*, vol. 224, no. 7, pp. 745–755, 2010.

[148] P. Nau, Z. Yin, O. Lammel, and W. Meier, "Wall Temperature Measurements in Gas Turbine Combustors With Thermographic Phosphors," *Journal of Engineering for Gas Turbines and Power*, vol. 141, no. 4, 2019.